IN-02-CR
87656
514686
132P
p-~~146~~

DEVELOPMENT AND APPLICATION OF COMPUTATIONAL AEROTHERMODYNAMICS FLOWFIELD COMPUTER CODES

Technical Progress Report

for
Cooperative Agreement No. NCC2-420

for the period
October 1, 1991 - March 31, 1992

Submitted to

National Aeronautics and Space Administration
Ames Research Center
Moffett Field, California 94035

Aerothermodynamics Branch
Dr. George S. Deiwert, Chief and Technical Monitor

Thermosciences Division
Dr. Jim Arnold, Chief

Prepared by

ELORET INSTITUTE
1178 Maraschino Drive
Sunnyvale, CA 94087
Phone: 408 730-8422 and 415 493-4710
Telefax: 408 730-1441
K. Heinemann, President and Grant Administrator
Ethiraj Venkatapathy, Principal Investigator

7 May, 1992

(NASA-CR-190294) DEVELOPMENT AND
APPLICATION OF COMPUTATIONAL
AEROTHERMODYNAMICS FLOWFIELD COMPUTER CODES
Progress Report, 1 Oct. 1991 - 31 Mar. 1992
(Eloret Corp.) 146 p
N92-24229
Unclas
CSCL 01A G3/02 0087656

Summary

Research activity carried out by each research associate on the Grant NCC2-420 are listed below. The activity covers the period October 1991 through March 1992. Dr. Greg Wilson is a new associate in this grant.

Dr. Dikran Babikian

Predicting and characterizing the flowfield of the 20 MW Arc-Jet is in progress. Various available computer codes are used for the different sections of the flow for initial predictions.The predictions of the free stream spectra has been obtained and compared with the experimental data. The prediction of the shock layer spectra and it's comparison with the available experimental data is in progress.

Dr. Tahir Gokcen

The work in progress is in two areas. First, the coupling of the radiative transfer to flow motion for a non-gray emitting and absorbing gas has been formulated for two-dimensional nonequilibrium flows. The preliminary results will be presented in AIAA 23rd Plasma Dynamics and Lasers Conference, July 6-8, 1992, Nashville, Tennessee. Please see the attached copies of the AIAA paper abstract. Second, in collaboration with Dr. Iain Boyd of Eloret Institute, thermochemical models for continuum and particle simulations of hypersonic flow is being investigated. The results will be presented in AIAA 27th Thermophysics Conference, July 6-8, 1992, Nashville, Tennesse. Please see the attached copies of the AIAA paper abstract under Appendix A.

Dr. Seung-Ho Lee

In previous period, I performed the grid generation for the flow field calculations for the NASA-Ames NASP nozzle/afterbody model, which had been tested in the Ames 3.5 ft. hypersonic wind tunnel. The result of the flow field calculation along with the experimental result presented as AIAA Paper 92-0387 in the AIAA 30th Aerospace Meeting & Exhibit, Reno, Nevada, January 6-9, 1992, entitled "Single Expansion Ramp Nozzle Simulations."

Pulse facilities , such as the reflected shock tunnel, expansion tubes, and gun tunnels, can produce a pulse of high energy airflow over a short time, typically on the order of a millisecond. It is this ability to produce high energy levels in a test gas that has led to the application of these type facilities to the experimental study of hypersonic mixing and combustion in a scramjet propulsion system for a

NASP-type evhicle. Those facilities had been evaluated for the test conditions using the various flow codes (mostly one-dimensional codes) with their own chemistry models. It is important to evaluate those chemistry models and their reactions and choose the best suitable model. Application of this model would enable to simulate the conditions at the test sections of the pulse hypersonic facilities. The result of this study will be presented in the AIAA 17th Aerospace Ground Testing Conference, Nashville, Tennessee, July 6-8, 1992, entitled "Thermochemical Relaxation in High Enthalpy Nozzle Flows" (AIAA Paper 92-4015). Please see the attached copies of the AIAA paper abstract under Appendix B.

Dr. Dinesh Prabhu

The following tasks were initiated and completed for the reporting period Oct.'91-Mar.'92 - (1) As a preliminary test of the capability of the computer codes, the flow past a two-dimensional wedge was simulated using nonequilibrium upwind codes developed by Dr.J.-L. Cambier. The computed results were compared with those obtained at Langley Research Center. The good agreement between the codes gave the confidence to compute the flow in the inlet of the NASP combustor. (2) The performance of the NASP combustor inlet (modelled as a two-dimensional geometry) was studied for the 16" Shock Tunnel flow conditions corresponding to driver pressures of 6000 psi and 8000 psi. The effect on the performance due to varying cowl lengths and flow Mach numbers was also investigated. The location of the impingement point of the cowl shock was determined for various cowl lengths and special attention was paid to the case of shock cancellation at the body surface. This work was done in collaboration with Dr. J.-L. Cambier whose two-dimensional/axisymmetric nonequilibrium codes were used and during the course of this study a detailed grid sensitivity analysis of the computer codes was done. The adaptive gird code SAGE developed by Dr.Venkatapathy and Dr. Davies was also used in order to more accurately obtain the impingement points. (3) In support of the absorption experiment to be located at station N3 of the 16" shock tunnel nozzle, the NO(γ) system [(0,0) and (0,1) bands] was studied in absorption with both quasi-one dimensional and two-dimensional axisymmetric reacting flow analyses. The required depth of the optical access, to minimize the effects of the hot boundary layer on the measurements, was estimated. The NO(γ) band system was studied in very high-resolution with and without splitting of the $^2\Sigma$-$^2\Pi$ transitions. The entire analysis was done with the assumption of chemical nonequilibrium and thermal equilibrium using a spectral code NEQAIR developed by Dr. Ellis Whiting. (4) A similar analysis was done at the exit of the nozzle in order to characterize the chemical state of the gas. (5) The spectra code was modified in order to do the spectroscopic study of the contaminants in the shock tunnel. The spectroscopic data for the species Fe, Cr, Ni and Cu are now incorporated into the code and the code has been handed over to the experimentalists who plan on using it to study the contamination levels in the shock tunnel. (6) The calibration of the Pinckney static pressure probes was initiated using a nonequilibrium parabolized Navier-Stokes code. Please see the Appendix C for further details.

Ms. Susan Tokarcik

1. I participated in the Ames Technical Paper Contest for Women. I presented work on hypersonic drag devices. I was one of the winners of this contest and will be attending the Society of Women Engineers Conference in June to present my winning paper. Also, a paper on this material has been submitted to the Journal of Spacecraft and Rockets for publication.

2. I have also been working on computing the flowfield around a lunar return aerobrake concept proposed by Mike Tauber. I am working with E. Venketapathy on this project. Thus far an axisymmetric study of the aerobrake design has been completed for an aerobrake with flares at angles of 50^{∞}, 55^{∞}, and 60^{∞}. Three-dimensional calculations have also been completed at the same flare angles. It has been found that because of the large separated region created by the flares, the flow about the aerobrake is very complicated. Further investigation of this flow is

anticipated and will include calculation of the base flow region. Comparisons between the axisymmetric solutions and the 3-D solutions have been made for surface pressure, size of the separated region, and total drag produced. Validation of the drag calculations and general flowfield character are to be completed by calculating a similar flowfield that has been studied experimentally. A representative picture of this work is shown in Figure 1.

3. I am continuing as point of contact for the University of Maryland. Maryland is involved in the CFD support effort for the Ames 16" shock tunnel. Thus far J.L. Cambier's axisymmetric TVD code (Emozart_2dA.f) has been transfered to the University of Maryland as well as the configuration of the ARC 16" shock tunnel nozzle and a generic combustor design. Cambier's 3-D code will eventually be transfered to the University of Maryland so that they can perform a full 3-D calculation of the test section flow with the combustor model in the test section. This study is being performed in order to determine the likelihood of choking the tunnel with the combustor model.

4. My involvement with the CFD support of the 16" shock tunnel has increased in the last six months and will increase further when D. Prabhu leaves the project. I am also working with J.L. Cambier on this project A fully turbulent, nonequilibrium chemistry calculation of the nozzle flow has been completed. Information from this solution was used

to characterize the flow in the test section and also to determine the optical character of the flow in the nozzle. A study of grid effects on the start-up solution has also been performed. This study was done assuming an inviscid, non-reacting flow. This start-up process begins at the breaking of the the diaphragm between the driven tube and the nozzle throat. A representative figure demonstrating grid effects is shown in Figure 2. A study of the entire start up procedure for a "best case" grid was also completed. This was also for inviscid, non-reacting flow. Figure 3. shows a time history of the start-up procedure.

A study of the applicability of calculating quasi-one-dimensional (Q-1D) flow of a reacting gas in order to simulate the full axisymmetric, turbulent solution was performed. It is shown that by decreasing the nozzle radius by 13% (an 87% nozzle), the flow in the turbulent, reacting case could be simulated successfully at a fraction of the CPU time required for the axisymmetric calculation. The results of this study are shown in Figure 4. Note that the Q-1D solution gives no information about boundary layer thickness or core flow profiles. This study will be continued further in order to determine if some "rules of thumb" exist for simulating axisymmetric, turbulent flows with finite rate chemistry with a Q-1D code with finite rate chemistry. The Q-1D code is also being used to study the effects of varying the chemical reaction rates for the reactions taking place in the nozzle.

Another study being done at this time is the simulation of the full driver tube, driven tube and nozzle flows in a time accurate manner. This simulation is axisymmetric, turbulent, and has finite rate chemistry. A representative figure of this flow is shown in Figure 5. In this figure, the diaphragm between the driver tube and the driven tube has partially ruptured and a shock has formed in the driven tube.

The results completed thus far for the Ames 16" shock tunnel will be presented at the AIAA Thermophysics Conference in July.

Please see the Appendix D for further details.

Dr. Ethiraj Venkatapathy

The axis singularity problem for three dimensional blunt body flows were addressed and two possible methods were found to work equally well. These methods and the results were reported at the 30th AIAA Aerospace Sciences Meeting in January 1992. The work was performed in collaboration with Mr. Grant Palmer of NASA Ames research Center. A copy of the publication entitled, "Effective Treatment of the Singular Line Boundary Problem for Three Dimensional Grids," is attached at the end.

Related to the National Aero-Space Plane (NASP) Program, simulations of the single expansion ramp nozzle experiment were completed and the results along with preliminary experimental comparisons were reported in a AIAA publication entitled " Single Expansion Ramp Nozzle Simulations," at the 30th Aerospace Sciences Meeting in Reno in January 1992. This work was done inn collaboration with Mr. S.M. Ruffin of NASA Ames, Dr. E. Keener of Eloret Institute, Dr. F. Spade of McDonnel Douglas Research Laborataries of St. Louis and Dr. Seung-Ho Lee of Eloret Institute. A copy of the publication is attached at the end.

To understand the flow around a Lunar Return Aero-Brake Vehicle and to predict total drag for a number of configurations, flow simulations were performed with an axisymmetric and full 3-D geometries. Preliminary predictions indicate an effective way of predicting drag for a number of 3-D configurations with just axisymmetric computations. Though flow details for the full 3-D configurations are very complex and completely three dimensional, integrated quantities such as drag coefficient can be evaluated with simpler computations. These findings are very useful in the design process. This work was performed in collaboration with Ms. Susan Tokarcik of Eloret Institute and Dr. Mike

Taubar of NASA Ames Research Center. Complete computations and results on this topic will be presented in an upcoming AIAA conference.

Please see the Appendix E for further details.

Dr. Greg Wilson

Work for this reporting period has involved a transition from my Ph.D. research at Stanford University to research involving the NASA Ames 16 inch, combustion driven shock tunnel. My dissertation was published in December and an additional work co-authored by Myles A. Sussman, a Stanford University graduate student, and myself was submitted to the AIAA Journal. Both works present numerical simulations used to investigate periodic combustion instabilities observed in ballistic-range experiments of blunt bodies flying at supersonic speeds through hydrogen-air mixtures. The computations are validated by comparing experimental shadowgraphs to shadowgraphs created from the computed flowfields and by comparing the frequency of the experimental and computed instabilities. The simulations add insight into the physical processes observed in the experiments and help establish the usefulness of the ballistic-range experiments for the validation of numerical methods and chemical kinetic models.

Initial research involving the Ames 16 inch Shock tunnel has involved time-dependent quasi-one-dimensional simulations using finite rate chemistry to simulate the driver and driven sections of the facility. Studies to date have helped quantify viscous and heat conduction losses during shock tunnel runs and to demonstrate the effect of driver tube pressure gradients on tunnel performance. Numerical simulations which include these phenomena compare well with experimental data obtained from the facility.

To compliment the numerical simulations of the shock tunnel, expansion tube flow is also being examined using the same numerical tools. This is in support of work being done by Dr. Seung-Ho Lee.

Wilson, G. J., ``Computation of Steady and Unsteady Shock-Induced Combustion Over Hypervelocity Blunt Bodies,'' *Ph.D Thesis*, Stanford University, December, 1991.

Wilson, G. J. and Sussman, M. A., ``Computation of Unsteady Shock-Induced Combustion Using a Logarithmic Form of the Species Conservation Equations,'' Submitted to the *AIAA Journal*, December, 1991.

Please see the Appendix F for further details.

Appendix A

Abstract submitted for 23rd AIAA Plasma Dynamics and Lasers Conference
July 6-8, 1992, Nashville, Tennessee.

THE COUPLING OF RADIATION TO BLUNT BODY FLOWS IN THERMOCHEMICAL NONEQUILIBRIUM

by
Tahir Gökçen †
Eloret Institute, 3788 Fabian Way, Palo Alto, CA 94303

In hypersonic flight, the radiative energy transfer to the surface of a blunt reentry body becomes an important mode of heat transfer as very high temperatures are attained behind the bow shock. The radiative transfer occurs along with the other modes of heat transfer, conduction and convection. For most of the aerothermodynamic flow problems, the radiation and flowfield are not coupled, i.e., the effects of radiation emission and absorption on flowfield are neglected. The radiative energy flux to the wall is then calculated from this uncoupled flowfield solution. On the other hand, for flow problems such as predicting aerobrake flow environment of planetary entry vehicles, radiative transfer becomes significant enough that its presence alters the flowfield, which in turn affects the radiative heat transfer at the wall. In such situations the radiation and flowfield are said to be strongly coupled, therefore, a simultaneous treatment is necessary. This coupling leads to a set of integro-differential equations, which are much more complicated than the governing differential equations of non-radiating flows.

Main objective of the proposed paper is to present the numerical tools to simulate two dimensional or axisymmetric thermochemical nonequilibrium flows with strong radiation coupling. In particular, a thermochemical nonequilibrium radiating shock layer about a blunt body is considered, and a schematic of such flowfield is shown in Figure 1.

The present nonequilibrium gas model for air consists of eleven chemical species, (N_2, O_2, NO, N, O, N_2^+, O_2^+, NO^+, N^+, O^+, e^-), and the thermal state of the gas is described by three temperatures: translational, rotational and vibrational (vibrational-electronic). The radiative energy transport is assumed to be one-dimensional, the dimension being normal to the wall. This is the so-called tangent-slab approximation which is applicable to the stagnation region of a blunt body or to blunt bodies of large radius of curvature. The thermal radiation is assumed to be governed by the vibrational temperature.[1] The gases are assumed to be non-gray, and the spectral absorption coefficients of the species are prescribed by 615 absorption bands.[2]

---

† Research Scientist, Member AIAA
Mailing Address: NASA Ames Research Center, MS 230-2, Moffett Field, CA 94035

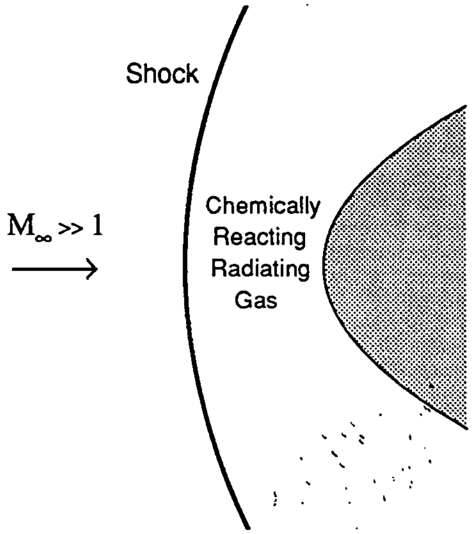

Fig. 1. Schematic of a nonequilibrium radiating shock layer about a blunt body.

The governing Navier-Stokes equations are augmented with the equations accounting for thermochemical nonequilibrium processes. The equation set consists of sixteen partial differential equations: eleven mass conservation equations for species, two momentum equations for two dimensional flows, and three energy equations. The numerical approach to solve the governing equations follows the previous work on non-reacting and reacting flows, and incorporates several features developed earlier.[3-5] The method is fully implicit for fluid dynamics, chemistry, and radiative transfer. It uses flux vector splitting for convective fluxes, and shock capturing along with adaptive grid strategy is also implemented. The radiative flux is treated fully implicitly, which results in the full block matrix difference equations. The full block matrix is inverted iteratively using block iteration methods such as Gauss-Seidel Line Relaxation.[6]

The development of the code for two dimensional blunt body flows with fully coupled radiation is currently in progress. Therefore, preliminary results are presented. As a test case, hypersonic ionizing flow over a 45° blunt cone is considered. Freestream conditions of $u_\infty = 12.\,\text{km/s}$, $T_\infty = 300.\,^\circ K$, and $\rho_\infty = 1. \times 10^{-4}\,\text{kg/m}^3$ are prescribed. The selected velocity is high enough that both the ionization and the radiation phenomena play important role in the flowfield behind the shock wave. Figure 2 depicts the blunt cone geometry and computational adaptive grid. For these computations flow is assumed to be inviscid, and the grid is only adapted to the shock wave. As an example of the flowfield chemistry, the electron mole fraction contours near the nose region are plotted in Figure 3, showing the extent of ionization. The electron mole fraction and temperature profiles along the stagnation streamline are presented in Figure 4 and 5, respectively. In Figure 4, there are two distinct peaks in the electron mole fraction plot. The first peak is attributed to the associative ionization processes and the second to the electron-impact ionization.[7]

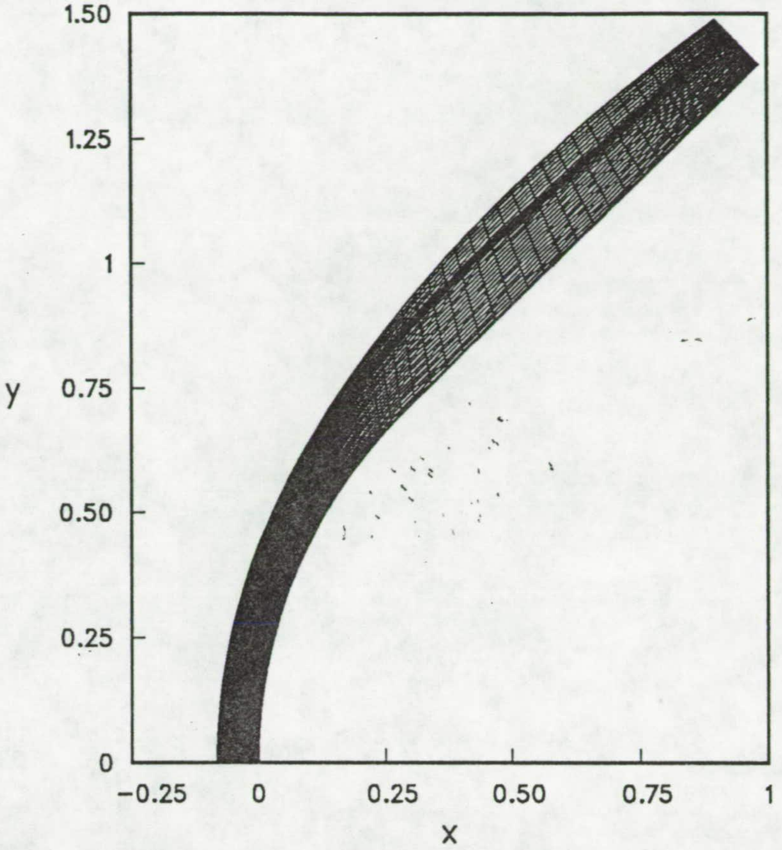

Fig. 2. Computational grid (50 × 30) over a 45° blunt cone.

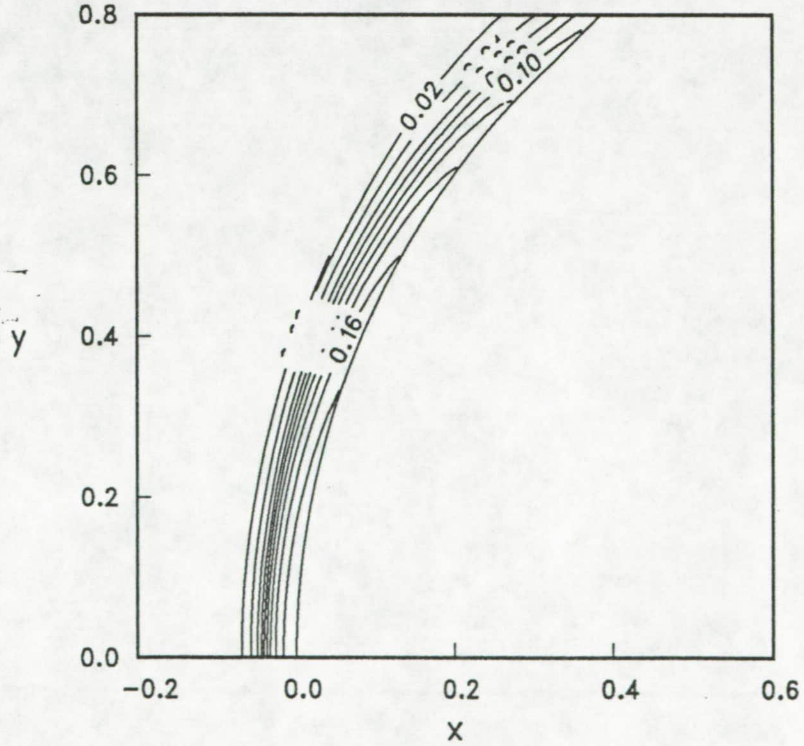

Fig. 3. Electron mole fraction contours near the nose region of the 45° cone. Freestream conditions: $u_\infty = 12.\,\mathrm{km/s}$, $T_\infty = 300.\,^\circ K$, $\rho_\infty = 1. \times 10^{-4}\,\mathrm{kg/m^3}$.

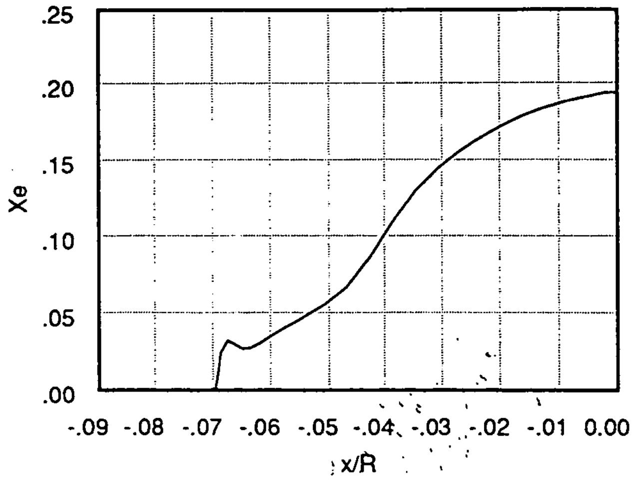

Fig. 4. Electron mole fraction profile along the stagnation streamline of the 45° cone.

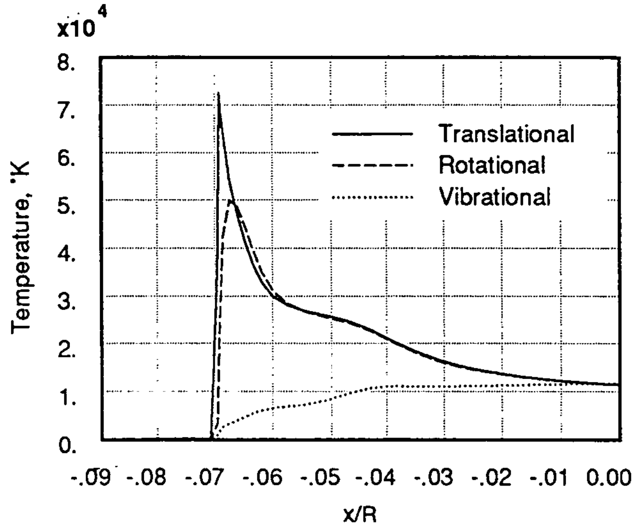

Fig. 5. Temperature profiles along the stagnation streamline of the 45° cone.

This shift in the dominant ionization process along the streamline in turn affects the temperature profiles. As seen from Figure 5, the temperature profiles show an inflection point in the relaxation zone rather than monotonically approaching to the equilibrium value. Similar behavior is observed by Park's one dimensional computations.[7] For radiative transfer computations of the test case, the spectral absorption coefficient κ_λ is assumed to be constant ($\kappa_\lambda = 1.0 \text{ m}^{-1}$, gray gas). The variation of total radiative flux along the stagnation streamline is plotted in Figure 6. The radiative flux is constant upstream of the shock since the upstream gas is specified to be transparent.

As mentioned earlier, these results are preliminary, the proposed paper will give results for both gray and non-gray gases in much greater detail. The emphasis will be on the numerical solutions for nonequilibrium blunt body flows where the flowfield and radiation field are strongly coupled. The paper will also present details of the numerical procedures associated with the radiation coupling.

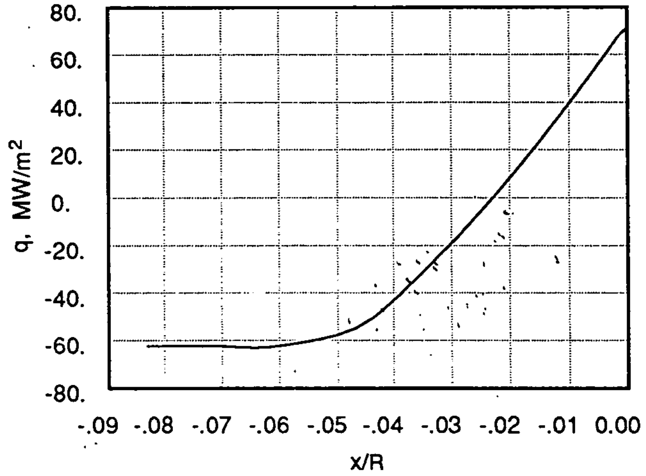

Fig. 6. Variation of the total radiative flux along the stagnation streamline of the 45° cone.

References

[1] Park, C., *Nonequilibrium Hypersonic Aerothermodynamics*, John Wiley and Sons, Inc., New York, 1989.

[2] Park, C., and Milos, F. S., "Computational Equations for Radiating and Ablating Shock Layers," *AIAA paper 90-0356*, 1990.

[3] MacCormack, R. W., "Current Status of the Numerical Solutions of the Navier-Stokes Equations," *AIAA paper 85-0032*, 1985.

[4] Candler, G.V., "The Computation of Weakly Ionized Hypersonic Flows in Thermo-Chemical Nonequilibrium," *Ph. D. Thesis*, Stanford University, 1988.

[5] Gökçen, T., "Computation of Hypersonic Low Density Flows with Thermochemical Nonequilibrium," *Ph. D Thesis*, Stanford University, 1989.

[6] Gökçen, T., and Park, C., "The Coupling of Radiative Transfer to Quasi 1-D Flows with Thermochemical Nonequilibrium," *AIAA paper 91-0570*, 1991.

[7] Park, C., Howe, T. H., Jaffe, L. R., and Candler, G. V., "Chemical-Kinetic Problems of Future NASA Missions," *AIAA paper 91-0464*, 1991.

Abstract submitted for consideration to

AIAA 27th Thermophysics Conference, July 6-8 1992

Nashville, Tennessee

ASSESSMENT OF THERMOCHEMICAL MODELS FOR CONTINUUM AND PARTICLE SIMULATIONS OF HYPERSONIC FLOW

Iain D. Boyd and Tahir Gökçen

Eloret Institute

3788 Fabian Way

Palo Alto, California.

Computations are presented for strong shock waves that are typical of those that form in front of reentering spacecraft. The fluid mechanics and thermochemistry are modeled using two different approaches. The first employs traditional continuum techniques in solving the Navier-Stokes equations. The important chemical effect of vibration-dissociation coupling is simulated using a multi-temperature model. The second approach employs a particle simulation technique (the direct simulation Monte Carlo method, DSMC). This method employs a vibrationally-favored dissociation probability model. These techniques are assessed through comparison of solutions generated under hypersonic flow conditions. Separate cases are considered that are dominated by thermal relaxation processes (translational-rotational-vibrational energy exchange), and chemical relaxation processes (dissociation-ionization). These phenomena are each considered for pure nitrogen and comparison made with limited experimental data. The studies performed provide an improved understanding of the relationship between the thermochemical models employed in continuum and particle simulations of hypersonic flow.

A space-vehicle passing through the earth's atmosphere will traverse a number of different flow regimes. At lower altitudes, the fluid density is sufficiently large for the flow to be considered as lying in thermochemical equilibrium. However, as the vehicle ascends higher into the atmosphere, the molecular collision rate will fall, and low-density effects will become increasingly important.

Continuum methods are applied to flows in which the collision rate of the gas is sufficient to maintain Boltzmann energy distributions for the various thermal modes of the gas. It is not necessary that the temperatures associated with each of the different modes be equal, or that chemical equilibrium prevails. As a general, and somewhat arbitrary guideline, it is usually assumed that this condition is met when the Knudsen number of the flow lies below about 0.01. For computation in the transition flow regime, which lies beyond this continuum limit, the most generally successful approach has been the particle simulation technique such as DSMC.

The computation of flow properties for the flight trajectories of many space vehicles will require the use of both solution techniques mentioned above. The interface between the different flow regimes is therefore of great importance. Clearly, it is desirable to obtain consistent results with these numerical methods in an overlapping near-continuum flow regime. Although the thermochemical models employed in continuum and particle methods are quite different, under conditions of thermochemical equilibrium they should provide identical solutions. The relationship between a continuum solution and a particle simulation under conditions of thermochemical nonequilibrium, however, has not been investigated previously. It is therefore the purpose of the present paper to study these effects by computing typical hypersonic flows with both continuum and particle simulation methods. The continuum and particle approaches employed in this work are briefly described below.

The continuum nonequilibrium gas model for air consists of eleven chemical species, (N_2, O_2, NO, N, O, N_2^+, O_2^+, NO^+, N^+, O^+, e^-), and the thermal state of the gas is described by three temperatures: translational, rotational and vibrational (vibrational-electronic). The governing Navier-Stokes equations are supplemented by the equations accounting for thermochemical nonequilibrium processes. The equation set consists of sixteen partial differential equations: eleven mass conservation equations for species, two momentum equations for two-dimensional flows, and three energy equations. The numerical approach to solve the governing equations is described in Refs. 1-3 in detail. The method is fully implicit for fluid dynamics and chemistry. It uses flux vector splitting for convective fluxes, and shock capturing. An adaptive grid strategy is also implemented. For the computations in this paper, a two-dimensional axisymmetric blunt-body code is used and a freestream of pure nitrogen is prescribed.

The particle simulation code employed in this investigation provides modeling of the translational, rotational, vibrational, and electron energy distributions. These are complemented through simulation of dissociative, recombinative, ionizing, and exchange reactions. The code is vectorized for efficient execution on a Cray-YMP. Description of the vectorized implementation may be found in Refs. 4 and 5. The inclusion of electrons in the simulation is discussed in detail in Ref. 6. The code employs energy-dependent probabilities of rotational and vibrational energy exchange, and a vibrationally-favored dissociation model which are all described in Ref. 5. The thermal relaxation rates employed in the particle simulation have been equated with the continuum values through the definition provided in Ref. 7. The chemical rate data was chosen to correspond to the continuum values wherever possible.

Computations have been performed for three different sets of flow conditions for pure nitrogen and these are listed in Table 1. The flow conditions for case 1 correspond to those investigated experimentally by Sharma[8]. The density and temperature for cases 2 and 3 have been chosen to correspond to the ambient conditions of the earth's atmosphere at an altitude of 78 km. The freestream conditions provide increasing enthalpy corresponding to flow which is dominated in case 2 by thermal relaxation processes, and in case 3 by chemical relaxation processes.

One of the flow quantities which is most sensitive to changes in the modeling of thermochemistry is the vibrational temperature. This quantity is also of great physical significance due to its importance in the determination of radiative emission. Several computed profiles of vibrational temperature for case 1 are compared in Fig. 1. The continuum profile was obtained with Park's two-temperature dissociation model in which the controling temperature is given by the square root of the product of the translational and vibrational values. Three different solutions have been obtained with the particle method. The vibrationally-favored dissociation model (VFD) employed in the particle simulations computes a dissociation probability based on the total collision energy (the sum of the translational, rotational, and vibrational components) and may be biased in addition to the vibrational energy (see Ref. 5). The particle solution labeled (#1) employed the total collision energy to evaluate the dissociation probability, and set the degree of additional vibration-dissociation coupling to zero. This is the configuration which has been in general usage and leads to a dissociation rate which is higher than that computed with the continuum model. Hence the particle computed vibrational temperatures lie well below the continuum values. The particle solution labeled (#2) employed the total collision energy together with the degree of vibration-dissociation coupling determined in Ref. 5 for nitrogen. In this case, the particle simulated dissociation rate is slightly slower than the continuum rate. Finally, the particle solution labeled (#3) employed a total energy given by the sum of the translational collision energy, and the rotational and vibrational energies of only the dissociating molecule, and the vibration-dissociation coupling is retained. This model has the effect of speeding up the dissociation rate, and gives a profile for vibrational temperature which is in good agreement with the continuum computations. This configuration also represents the most physically realistic methodology for simulating dissociation within the framework of a phenomenological model.

The temperature profiles of the three energy modes computed with the continuum technique and particle method, for configuration (#3), are shown in Fig. 2. The experimental data of Sharma[8] is also included. Good agreement between the particle and continuum solutions for all three temperature profiles is obtained. The results obtained for the rotational and vibrational energy modes offer good correspondence to the experimental values both in the shock-front and in the equilibrium region far behind the shock. The close accord between the numerical methods is further demonstrated in Fig. 3 where the profiles for the mass fraction of atomic nitrogen are observed to compare well.

The density profiles computed with the two numerical methods for case 2 are compared in Fig. 4. The continuum solution is shown as a solid line, and the particle solution is shown as a dotted line. The thermochemical model employed in the particle simulation was configuration (#3). The distance through the shock-wave has been normalized by the nose radius (RN=2.3 m). The density rise predicted in the particle simulation preceeds that computed by the continuum method, producing a thicker shock-wave. In the relaxation zone behind the shock, there is generally good agreement between the two solutions. The computed temperature profiles are compared in Fig. 5. The rise in each of the temperatures computed with the particle method also preceeds that in the continuum solution. These types of differences between particle and continuum solutions have been found previously by Lumpkin and Chapman[6] who noted that the continuum equations predict shock-wave thicknesses which are smaller than those measured experimentally and which are predicted successfully with DSMC. The differences occur because the continuum formulation breaks down in regions of the flow where high gradients give rise to relatively large values for the local Knudsen number. In the present study, this occurs in the shock-front, where the temperatures first begin to rise.

Comparison is made of the species mole fractions computed with the two numerical methods in Fig. 6 for the 10 km/s conditions of case 3. Only the 3 major species are represented. Once again, the particle simulation was performed with the thermochemical model labeled (#3). Generally, quite good agreement is found for the two solutions. However, as in case 2, it is found that the thermochemical relaxation processes computed with the particle method preceed the continuum simulation results due to the presence of a thicker shock.

The good agreement found between the continuum and particle computations for case 1 is partly due to the relatively high-density freestream conditions which place the flow in the near-continuum regime. For cases 2 and 3, in understanding the differences between the continuum and particle solutions, it is difficult to separate the effects of chemical nonequilibrium from those of thermal nonequilibrium. Further studies are being undertaken to investigate these coupled phenomena in greater detail, and will be reported in the final paper.

Table 1. Flow conditions.

Case	U_∞ (km/s)	ρ_∞ (kg/m^3)	T_∞ (K)
1	6.2	1.50×10^{-3}	300
2	5	2.75×10^{-5}	188
3	10	2.75×10^{-5}	188

References

[1] MacCormack, R. W., "Current Status of the Numerical Solutions of the Navier-Stokes Equations," *AIAA paper 85-0032*, 1985.

[2] Candler, G.V., "The Computation of Weakly Ionized Hypersonic Flows in Thermo-Chemical Nonequilibrium," *Ph. D.Thesis*, Stanford University, 1988.

[3] Gökçen, T., "Computation of Hypersonic Low Density Flows with Thermochemical Nonequilibrium," *Ph. D Thesis*, Stanford University, 1989.

[4] Boyd, I.D., "Vectorization of a Monte Carlo Method For Nonequilibrium Gas Dynamics," Journal of Computational Physics, Vol. 96, 1991, pp. 411-427.

[5] Boyd, I.D., "Analysis of Vibration-Dissociation-Recombination Processes Behind Strong Shock Waves of Nitrogen," Physics of Fluids A (in press).

[6] Boyd, I.D. and Whiting, E.E., "Comparison of Radiative Heating Estimates Using Particle Simulation and Continuum Methods," abstract submitted to AIAA 27th Thermophysics Conference, Nashville, Tennessee, July 1992.

[7] Lumpkin, F.E., Haas, B.L., and Boyd, I.D., "Resolution of Differences Between Collision Number Definitions in Particle and Continuum Simulations," Physics of Fluids A, Vol. 3 (9), 1991, pp. 2282-2284.

[8] Sharma, S.P., "Vibrational and Rotational Temperature Measurements in a Shock Tube," *Proceedings of 18th International Shock Tube Symposium*, (Tohoku, Japan, 1991, in press).

[9] Lumpkin, F.E. and Chapman, D.R., "Accuracy of the Burnett Equations for Hypersonic Real Gas Flows," Journal of Thermophysics and Heat Transfer, (in press, see also AIAA-91-0771).

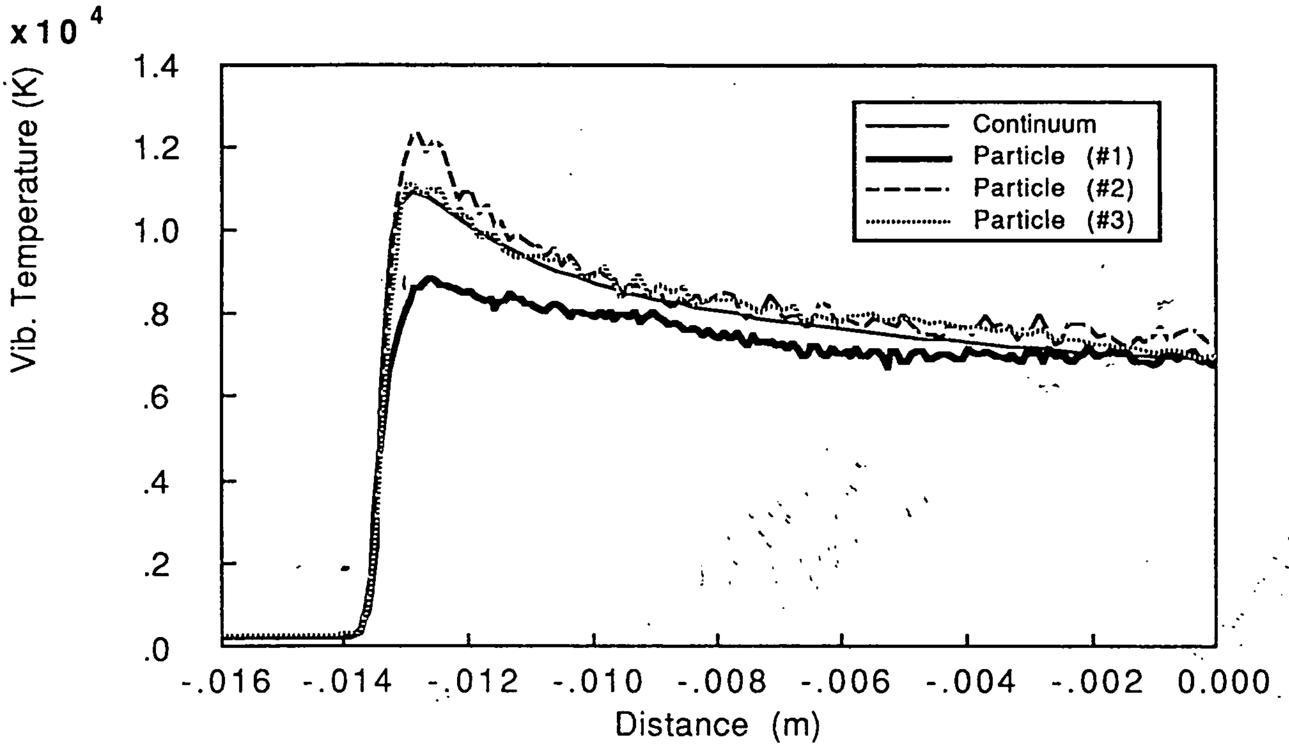
x 10 4
Vib. Temperature (K)
1.4
1.2
1.0
.8
.6
.4
.2
.0
-.016
-.014
-.012
-.010
-.008
-.006
-.004
-.002
0.000
Distance (m)
Continuum
Particle (#1)
Particle (#2)
Particle (#3)

Fig. 1

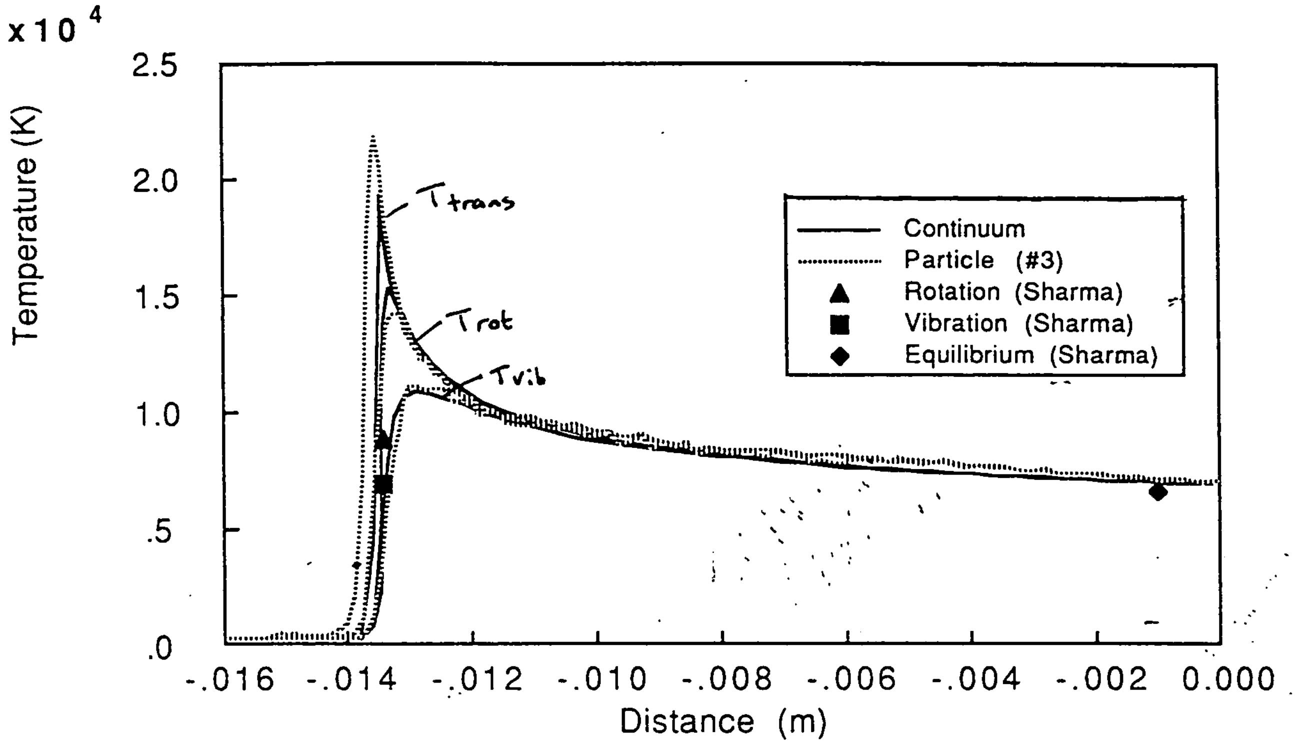
x 10 4
2.5
2.0
1.5
1.0
.5
.0
Temperature (K)
T trans
T rot
T vib
Continuum
Particle (#3)
Rotation (Sharma)
Vibration (Sharma)
Equilibrium (Sharma)
-.016
-.014
-.012
-.010
-.008
-.006
-.004
-.002
0.000
Distance (m)

Fig. 2

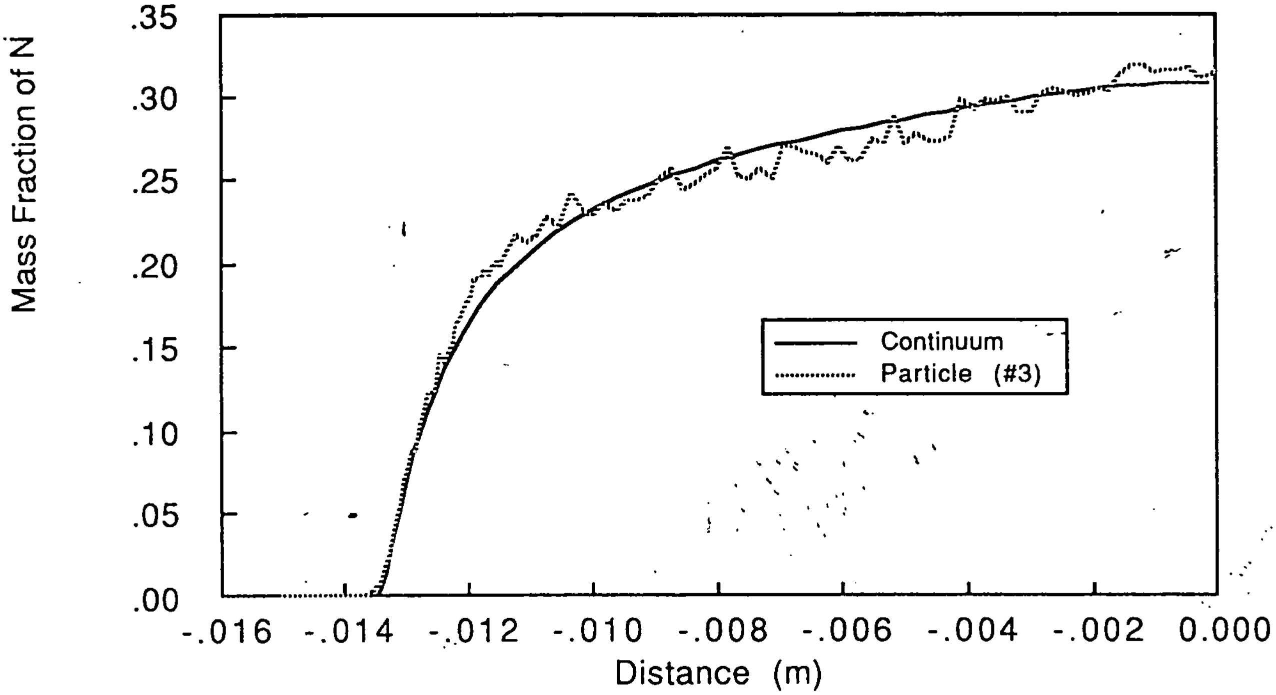
Mass Fraction of Ni
.35
.30
.25
.20
.15
.10
.05
.00
-.016
-.014
-.012
-.010
-.008
-.006
-.004
-.002
0.000
Distance (m)
Continuum
Particle (#3)

Fig. 3

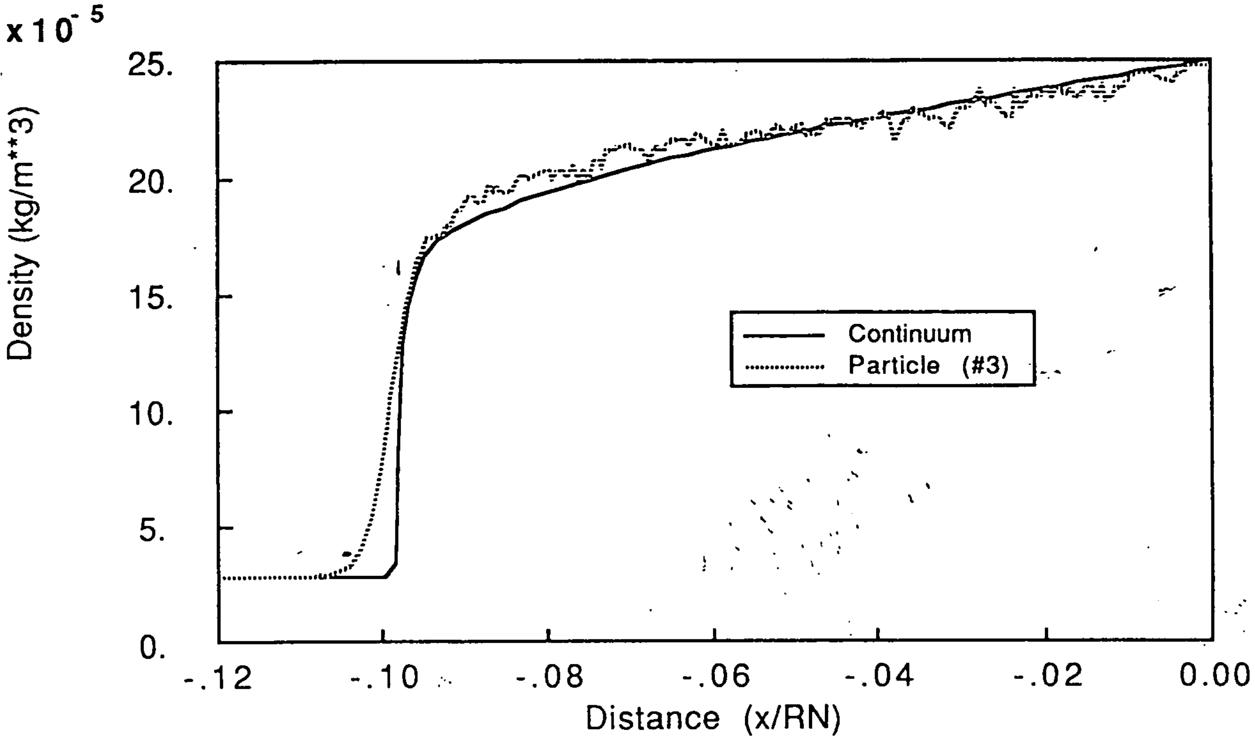
x 10^-5
Density (kg/m**3)
25.
20.
15.
10.
5.
0.
-.12
-.10
-.08
-.06
-.04
-.02
0.00
Distance (x/RN)
Continuum
Particle (#3)

Fig. 4

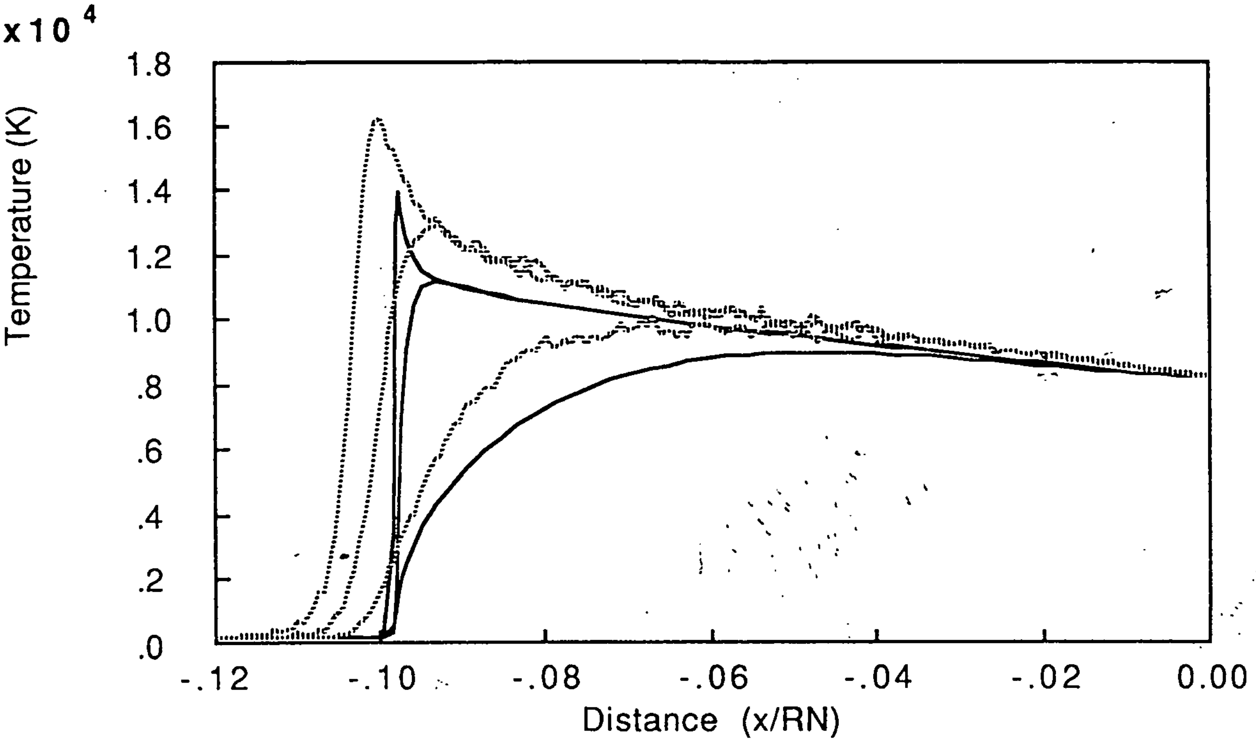
x 10 4
Temperature (K)
1.8
1.6
1.4
1.2
1.0
.8
.6
.4
.2
.0
-.12
-.10
-.08
-.06
-.04
-.02
0.00
Distance (x/RN)

Fig. 25

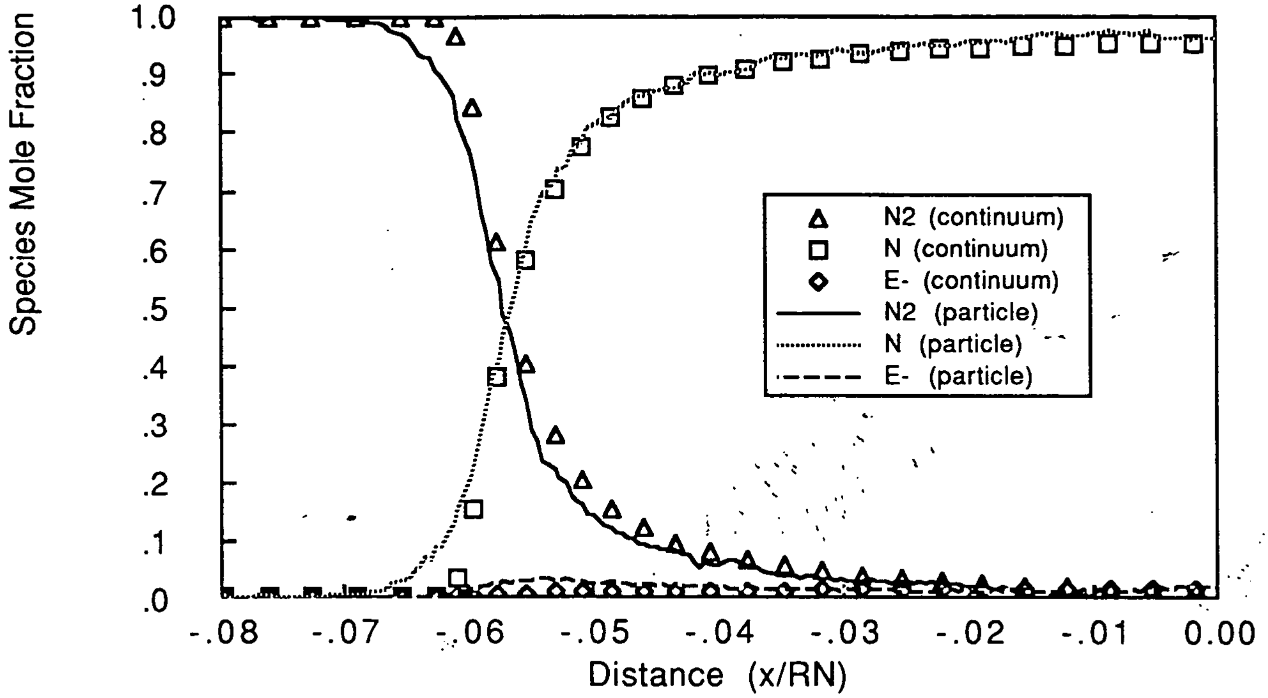
Species Mole Fraction
1.0
.9
.8
.7
.6
.5
.4
.3
.2
.1
.0
-.08
-.07
-.06
-.05
-.04
-.03
-.02
-.01
0.00
Distance (x/RN)
N2 (continuum)
N (continuum)
E- (continuum)
N2 (particle)
N (particle)
E- (particle)

Fig. 6

Appendix B

Proposed abstract for the AIAA 17th Ground Testing Conference
Nashville, Tennessee, July 6-8, 1992

THERMOCHEMICAL RELAXATION IN HIGH ENTHALPY NOZZLE FLOWS

Seung-Ho Lee, Eloret Institute, Palo Alto, CA
Mark Loomis, MCAT Institute, Moffett Field, CA
Chul Park, NASA Ames Research Center, Moffett Field, CA

Summary

The problem of thermochemical relaxation in a high enthalpy wind tunnel nozzles is reviewed. The operating conditions of the shock tunnels and arc-jet wind tunnels existing in the United States and elsewhere are first surveyed. Next the existing one-dimensional computer codes that calculate the thermochemical nonequilibrium state in the nozzle are reviewed and compared. The codes are run for the experimental conditions of CALSPAN and elsewhere in which vibrational and electron temperature and electron density have been measured. The discrepancy between the calculation and the experimental data is discussed. Comparison is made also between the interferometric fringe pattern obtained in a flow over a wedge placed in the 16 inch Combustion-Driven Shock Tunnel at Ames Research Center and that predicted by a code. A set of reaction rates is selected to reproduce the experimental data. Using this validated code, the degree of simulation is calcualted for the existing shock tunnels and arc-jet wind tunnels.

Introduction

With the advent of the aerospace vehicles such as Space Shuttle, an effort has been expended in recent years to produce a high enthalpy flow in a ground-based facility for testing of the models for such vehicles. High enthalpy flows are produced either by means of an arc-jet wind tunnel, hot-shot wind tunnel, expansion tube, or shock tunnel. To determine the thermochemical state of the flow produced in such facilities, several computer codes have been written. These codes require several thermochemical rate parameters as inputs. Validity of these codes and the rate parameters used have not yet been made, mostly because required measurements of the flow characteristics are difficult. Each laboratory uses different computer codes to determine the facility in the laboratory. Thus, there are several questions regarding the performance of such facilities. They are:

(1) What actually happens in the nozzle?

(2) Which computer code most closely reproduces the flow conditions in the nozzle?

(3) How do various facilities compare in their performance?

The purpose of the present work is to answer these questions.

What Actually Happens in the Nozzle?

The actual thermochemical phenomena in a high enthalpy nozzle flow can be understood by analyzing the experimental data obtained in various shock tunnels. The first of these sets of experimental data are those obtained at Cornell Aeronautical Laboratory in the late 1950s and early 1960s[1] in which vibrational temperature has been measured. The second set of such data are those taken also in Cornell Laboratory in which electron temperature and electron density have been measured.[2-4] The third set of data is obtained at Ames Research Center in which the electron density, electron temperature, and electronic excitation temperature have been measured.[5,6] Lastly, very recently, interferometric density measurement has been made at Ames Research Center in a shock tunnel for a flowfield produced by a two-dimensional wedge for both air and nitrogen. The interferogram, reproduced in Fig. 1, contains a peculiar bending of fringes, which indicates that density is decreasing toward the wall. This phenomenon is interpreted to be due to atomic recombination. The extent of the bending of the fringes will depend on the amount of dissociated atoms in the test section. By analyzing this data, it should be possible to deduce the degree of dissociation in the test section flow.

In the present work, a comprehensive one-dimensional computer code, named NOZ3T, has been developed recently to numerically reproduce the above-mentioned experimental data. The code allows three temperatures, namely, the translational-rotational, vibrational, and electron-electronic, to be different. This was necessitated by the fact that some of the experimental data are in the form of vibrational temperature or electron temperature. An example of the use of this code is shown in Fig. 2, in which the experimental data of Dunn and Lordi[2] is reproduced. Such comparison is being made presently for all other existing experimental data.

A two-dimensional, thermochemical nonequilibrium flow calculation is currently being undertaken to reproduce the interferogram of Fig. 1 by using the CENS2H code developed by Park and Yoon.[7] The degree of dissociation of the test section flow is being varied to find the value which best reproduces the interferogram. The results are not yet available, but will be presented in the final paper. The reaction rate set that produces the observed degree of dissociation will be determined by running the NOZ3T code. This completes validation of the code NOZ3T and the reaction rate set.

Which Code and What Rate Set Best Reproduce The Flow?

The validity of the existing computer codes that calculate the relaxation phenomena in a high enthalpy nozzle flow and the associate rate parameters is tested by comparing against the NOZ3T code so validated. The code so compared are: (1) CALSPAN code,[8] (2) Lewis GCKP code,[9] and (3) CHEMKIN code.[10] The comparison has not yet begun because the validation of NOZ3T is not yet been finished. The result of the comparison will be presented in the final paper.

How Do Each Facilities Perform?

Using the above-mentioned computer codes, comparison is being made between various different facilities in the world. The facilities chosen for this comparison are, for the present: (1) Ames 16 inch combustion-driven shock tunnel, (2) the piston-compression-heated shock tunnel T4 in Australia, (3) the piston-compression-heated shock tunnel T5 in California Institute of Technology, (4) the expansion tube at GASL. More facilities will be included in this list before the final paper. In Table 1, first of such comparisons is shown between the Ames 16 inch shock tunnel and T4.

Conclusions

It is the intention of this study to draw conclusion on (1) what computer code should be recommended for determining the thermochemical state in a nozzle in the high enthalpy regime, and (2) how each facility compare in their performance.

References

[1] Hurle, I. R., "Nonequilibrium Flows with Special Reference to the Nozzle-Flow Problem," Proceedings of the 8th International Shock Tube Symposium, 1971, pp. 3.1 - 3.37.

[2] Dunn, M. G., and Lordi, J. A., "Meausrement of N_2^+ + e Dissociative Recombination in Expanding Nitrogen Flows," AIAA Journal, Vol. 8, 1970, pp. 339-345.

[3] Dunn, M. G., and Lordi, J. A., "Measurement of O_2^+ + e Dissociative Recombination in Expanding Oxygen Flows," AIAA Journal, Vol. 8, 1970, pp. 614-618.

[4] Dunn, M. G., and Lordi, J. A., " Measurement of Electron Temperature and Number Density in Shock Tunnel Flows, Part 2. NO^+ + e Dissociative Recombination Rate in Air," AIAA Journal, Vol. 7, 1969, pp. 2099-2104.

[5] Park, C.,"Comparison of Electron and Electronic Temperatures in Recombining Nozzle Flow of Ionized Nitrogen-Hydrogen Mixture. Part 1. Theory," Journal of Plasma Physics, Vol. 9, 1973, pp. 187-215.

[6] Park, C.,"Comparison of Electron and Electronic Temperatures in Recombining Nozzle Flow of Ionized Nitrogen-Hydrogen Mixture. Part 2. Experiment," Journal of Plasma Physics, Vol. 9, 1973, pp. 217-234.

[7] Park, C., and Yoon, S., "Fully-Coupled Implicit Method for Thermochemical Nonequilibrium Air at Suborbital Flight Speeds," Journal of Spacecraft and Rockets, Vol. 28, 1991, pp. 31-39.

[8] Lordi, J. A., Mates, R. E., and Moselle, J. R., "Computer Program for the Numerical Solution of Nonequilibrium Expansion of Reacting Gas Mixtures," NASA CR-472, 1966.

[9] Bittker, D. A., and Scullin, V. J., "GCKP84 - General Chemical Kinetics code for Gas-Phase Flow and Batch Processes Including Heat Transfer Effects," NASA TP 2320, 1984.

[10] Kee, R. J., Miller, J. A., and Jefferson, T. H., "CHEMKIN: A General Purpose Problem-Independent, Transportable, Fortran, Chemical Kinetics Program Package," Sandia National Laboratories Report SAND80-8003, 1980.

Table 1. Comparison of the flow conditions for Ames 16 inch shock tunnel and T4.

	Ames 16" Shock Tunnel	T4 (Mach 4)	T4 (Mach 10)
Stagnation Chamber Condition			
Temperature (K)	5750	8000	8000
Pressure (mpa)	24.13	30.4	30.4
Enthalpy (mj/kg)	9.630	16.228	16.228
Nozzle Exit Condition			
Location from throat (m)	5.728	0.512	1.777
A/A*	270.8	28.0	624.5
Temperature (K)	678.8	2992.0	632.5
Pressure (kpa)	1.814	11.348	0.477
Density (kg/m^3)	0.00925	0.01235	0.00227
Velocity (m/sec)	4136.3	4586.5	4988.5
Mach number	8.13	4.24	5.43
Species Concentrations			
E^-	1.73×10^{-13}	4.96×10^{-12}	8.44×10^{-12}
N^2	7.27×10^{-1}	7.31×10^{-1}	7.37×10^{-1}
O^2	1.93×10^{-1}	1.27×10^{-1}	3.56×10^{-2}
Ar	1.29×10^{-2}	1.29×10^{-2}	1.29×10^{-2}
N	8.75×10^{-12}	2.52×10^{-5}	4.94×10^{-8}
O	5.98×10^{-3}	7.73×10^{-2}	1.75×10^{-1}
NO	6.19×10^{-2}	5.13×10^{-2}	3.95×10^{-2}
NO^+	9.80×10^{-9}	2.72×10^{-7}	4.62×10^{-7}

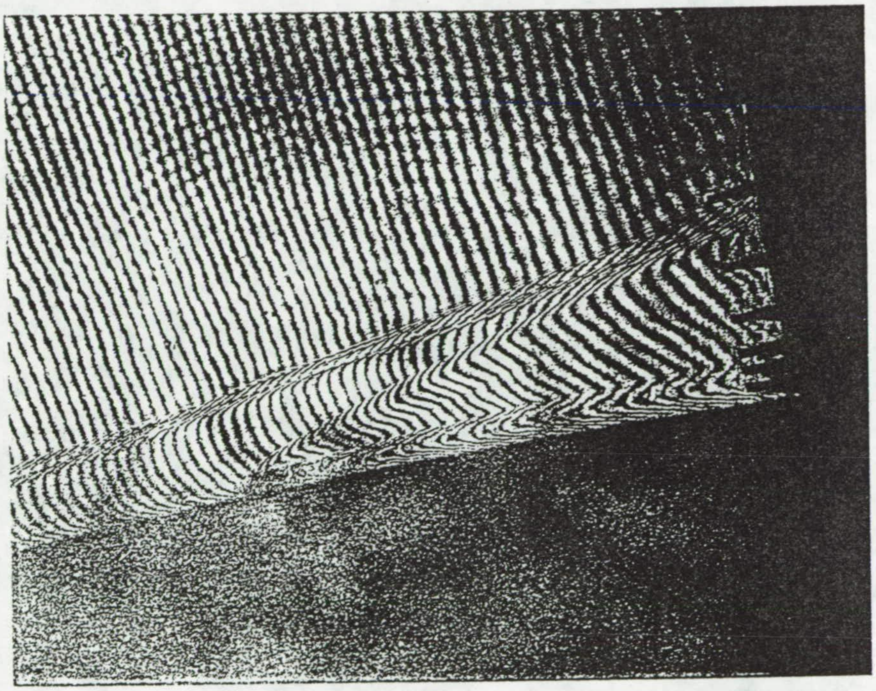

Figure 1. Holographic interferogram over a wedge at 11° inclination in the Ames 16 inch shock tunnel flow at H = 10 MJ/kg; test gas = air, reflected-shock pressure = 400 psia, with hydrogen injection.

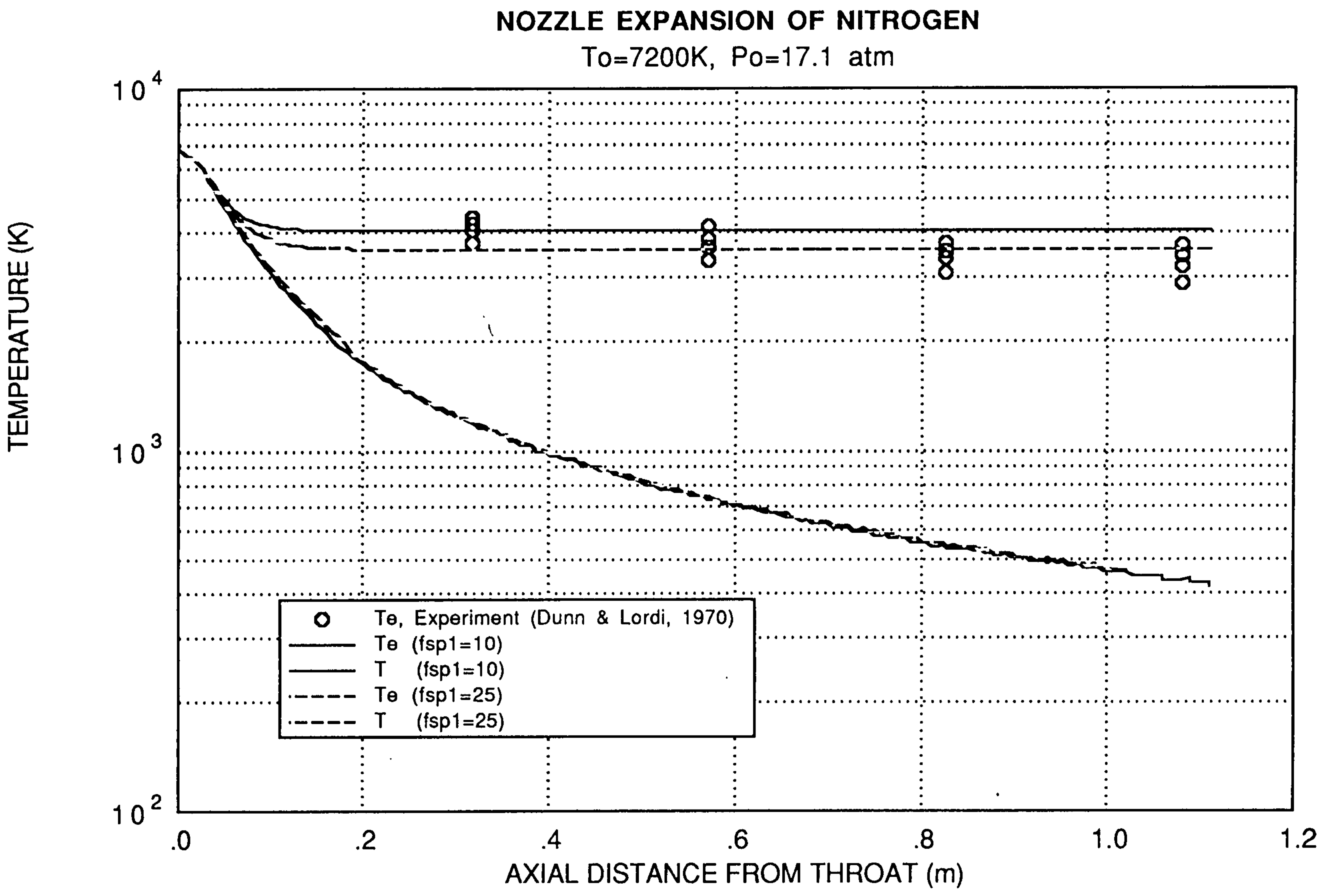

Figure 2. Comparison between the measured electron temperature and that calculated using the NOZ3T code for nitrogen for the experimental condition of Dunn and Lordi.[2]

Appendix C

Dr. Dinesh Prabhu

The following tasks were initiated and completed for the reporting period Oct.'91-Mar.'92 - (1) As a preliminary test of the capability of the computer codes, the flow past a two-dimensional wedge was simulated using nonequilibrium upwind codes developed by Dr.J.-L. Cambier. The computed results were compared with those obtained at Langley Research Center. The good agreement between the codes gave the confidence to compute the flow in the inlet of the NASP combustor. (2) The performance of the NASP combustor inlet (modelled as a two-dimensional geometry) was studied for the 16" Shock Tunnel flow conditions corresponding to driver pressures of 6000 psi and 8000 psi. The effect on the performance due to varying cowl lengths and flow Mach numbers was also investigated. The location of the impingement point of the cowl shock was determined for various cowl lengths and special attention was paid to the case of shock cancellation at the body surface. This work was done in collaboration with Dr. J.-L. Cambier whose two-dimensional/axisymmetric nonequilibrium codes were used and during the course of this study a detailed grid sensitivity analysis of the computer codes was done. The adaptive gird code SAGE developed by Dr.Venkatapathy and Dr. Davies was also used in order to more accurately obtain the impingement points. (3) In support of the absorption experiment to be located at station N3 of the 16" shock tunnel nozzle, the NO(γ) system [(0,0) and (0,1) bands] was studied in absorption with both quasi-one dimensional and two-dimensional axisymmetric reacting flow analyses. The required depth of the optical access, to minimize the effects of the hot boundary layer on the measurements, was estimated. The NO(γ) band system was studied in very high-resolution with and without splitting of the $^2\Sigma$-$^2\Pi$ transitions. The entire analysis was done with the assumption of chemical nonequilibrium and thermal equilibrium using a spectral code NEQAIR developed by Dr. Ellis Whiting. (4) A similar analysis was done at the exit of the nozzle in order to characterize the chemical state of the gas. (5) The spectra code was modified in order to do the spectroscopic study of the contaminants in the shock tunnel. The spectroscopic data for the species Fe, Cr, Ni and Cu are now incorporated into the code and the code has been handed over to the experimentalists who plan on using it to study the contamination levels in the shock tunnel. (6) The calibration of the Pinckney static pressure probes was initiated using a nonequilibrium parabolized Navier-Stokes code.

TWO-DIMENSIONAL WEDGE MODEL

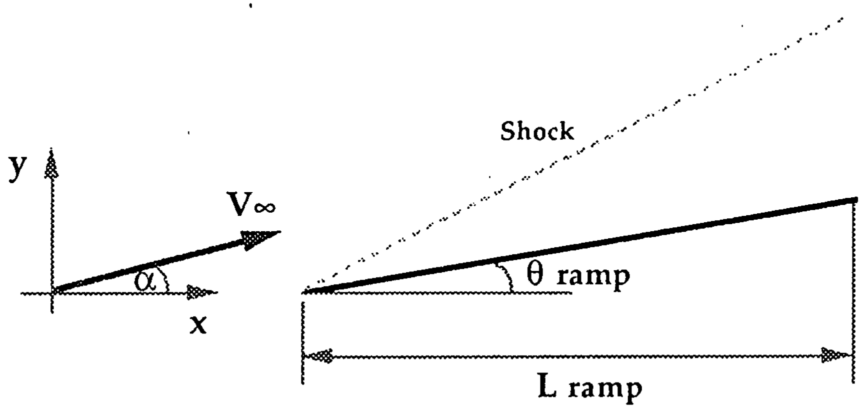

FOR THE PRESENT CALCULATIONS

L ramp = 14.724"
θ ramp = 11°
α = 0°

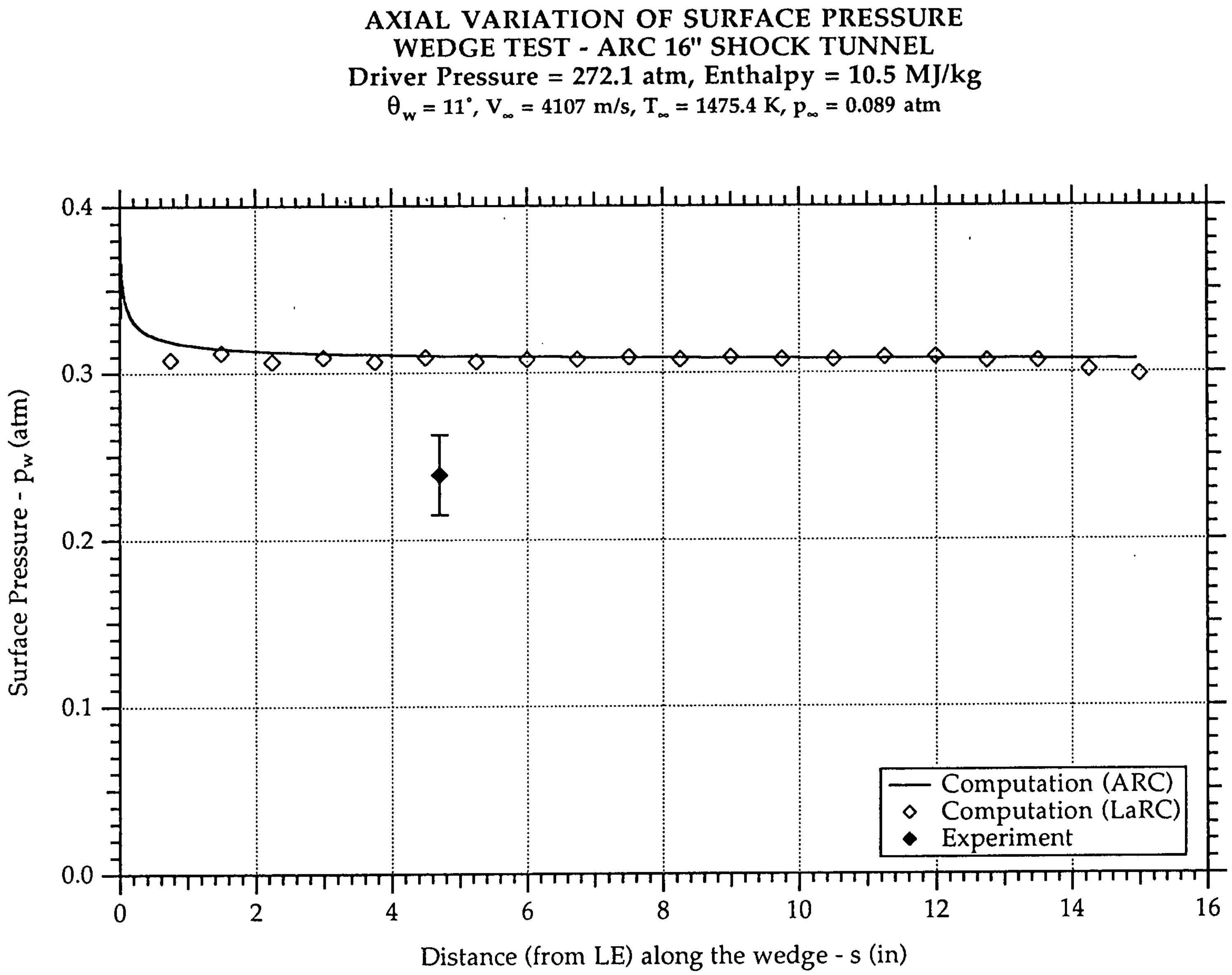

AXIAL VARIATION OF SURFACE PRESSURE
WEDGE TEST - ARC 16" SHOCK TUNNEL
Driver Pressure = 272.1 atm, Enthalpy = 10.5 MJ/kg
$\theta_w = 11^\circ$, $V_\infty = 4107$ m/s, $T_\infty = 1475.4$ K, $p_\infty = 0.089$ atm

AXIAL VARIATION OF SURFACE HEAT FLUX
WEDGE TEST - ARC 16" SHOCK TUNNEL
Driver Pressure = 272.1 atm, Enthalpy = 10.5 MJ/kg
$\theta_w = 11^\circ$, $V_\infty = 4107$ m/s, $T_\infty = 1475.4$ K, $p_\infty = 0.089$ atm

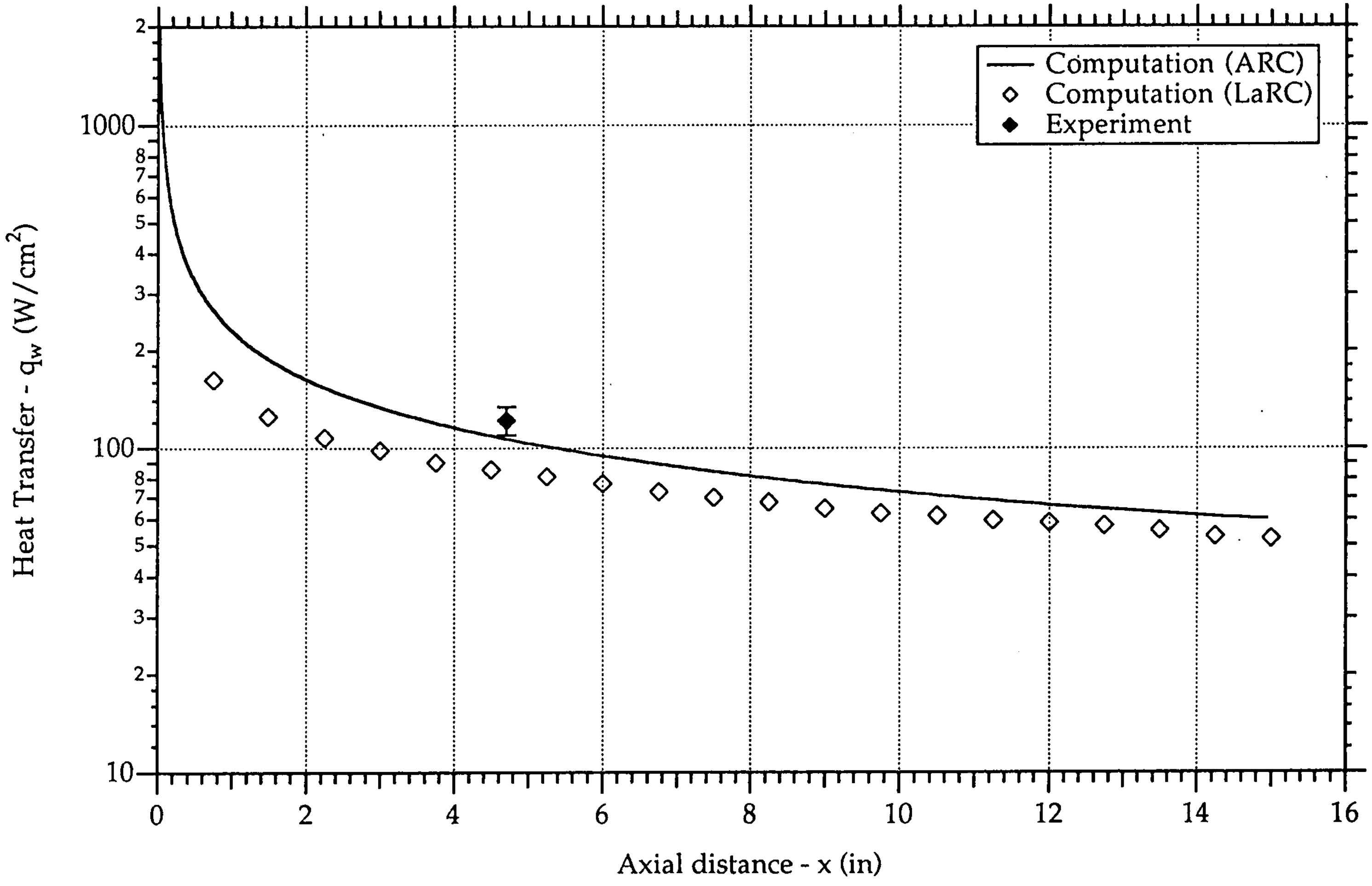

TWO-DIMENSIONAL COMBUSTOR MODEL FOR IMPINGEMENT CALCULATIONS

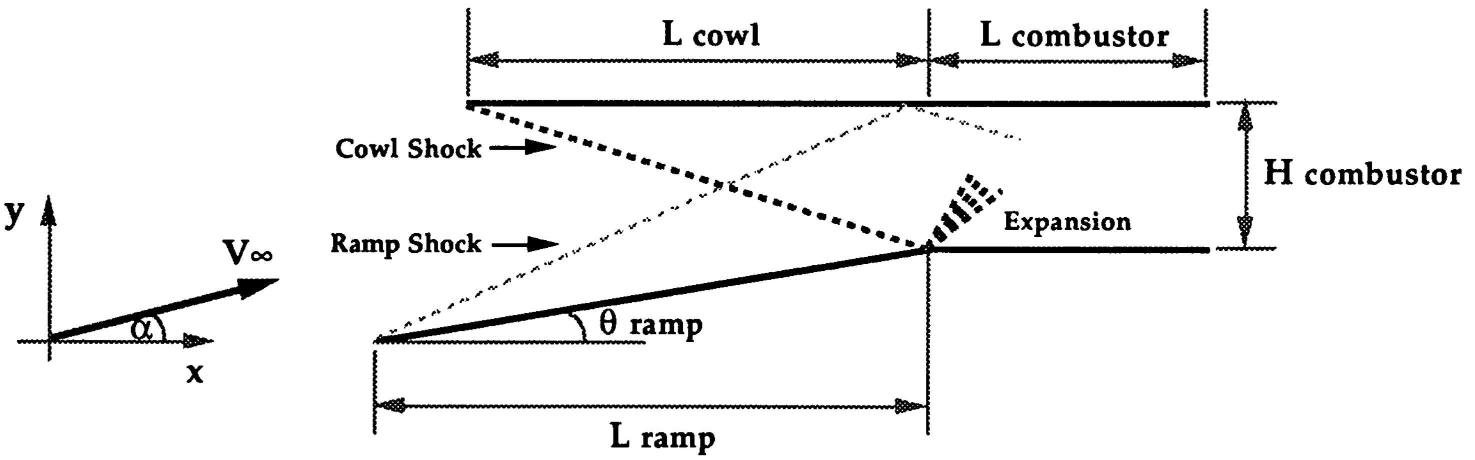

2D COMBUSTOR MODEL - IMPINGEMENT STUDY

MACH CONTOURS AT THE LOWER CORNER

P = 408.2 atm, H = 6.8 MJ/kg, M = 12

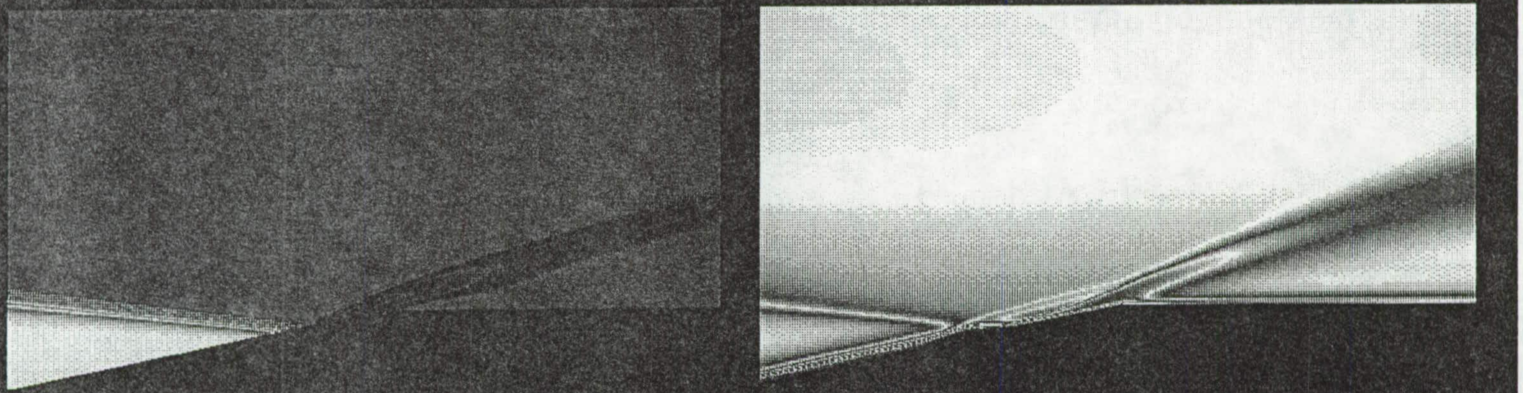

INVISCID FLOW

LAMINAR FLOW

2D COMBUSTOR MODEL -·IMPINGEMENT STUDY

MACH CONTOURS AT THE LOWER CORNER

P = 408.2 atm, H = 9 MJ/kg, M = 14

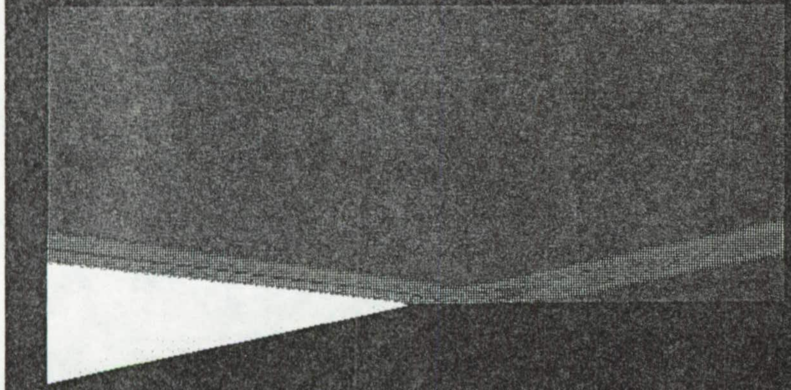

INVISCID FLOW

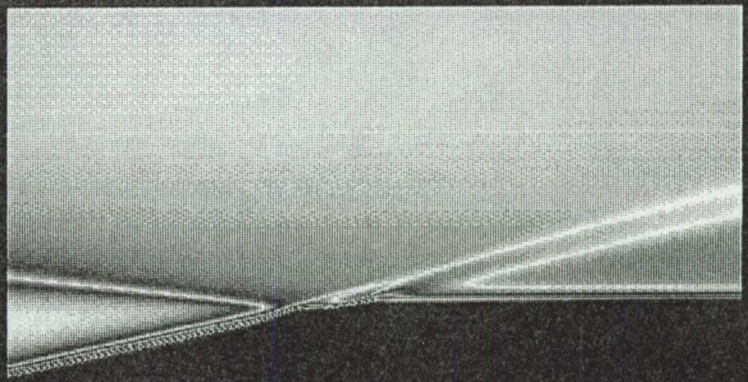

LAMINAR FLOW

2D COMBUSTOR MODEL - IMPINGEMENT STUDY

MACH CONTOURS AT THE LOWER CORNER

$P = 408.2$, $H = 10.5$ MJ/kg, $M = 15.5$

INVISCID FLOW

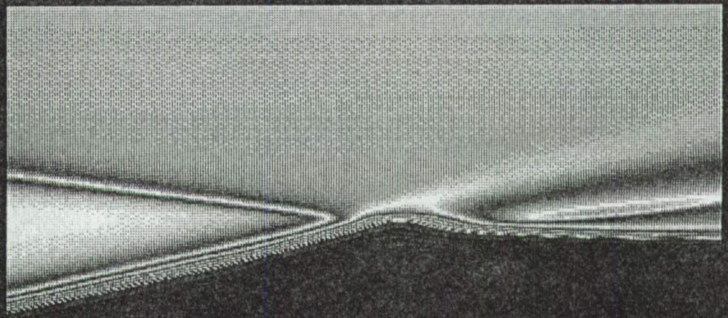

LAMINAR FLOW

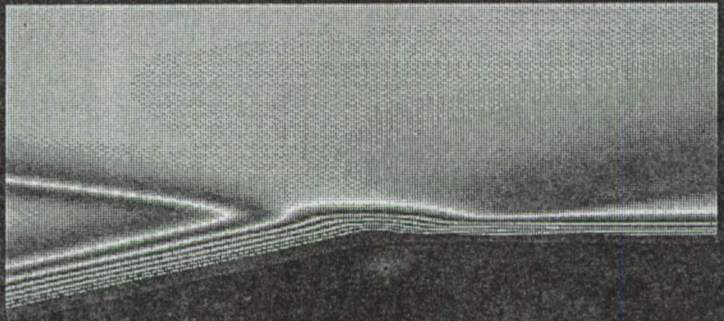

TURBULENT FLOW

LOWER WALL - SURFACE PRESSURE (INVISCID FLOW)
IMPINGEMENT STUDY - 2D COMBUSTOR MODEL
Driver Pressure = 408.2 atm

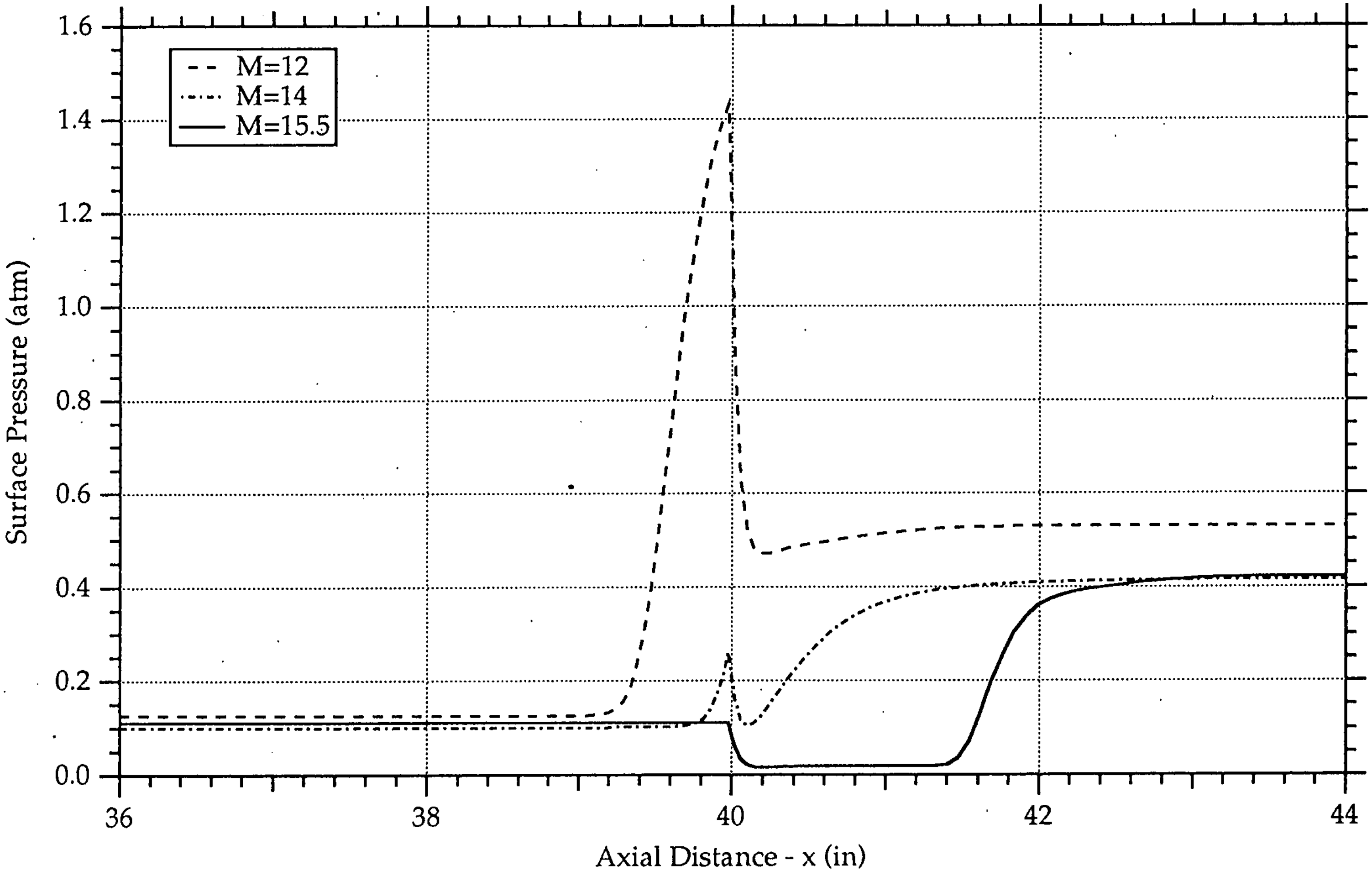

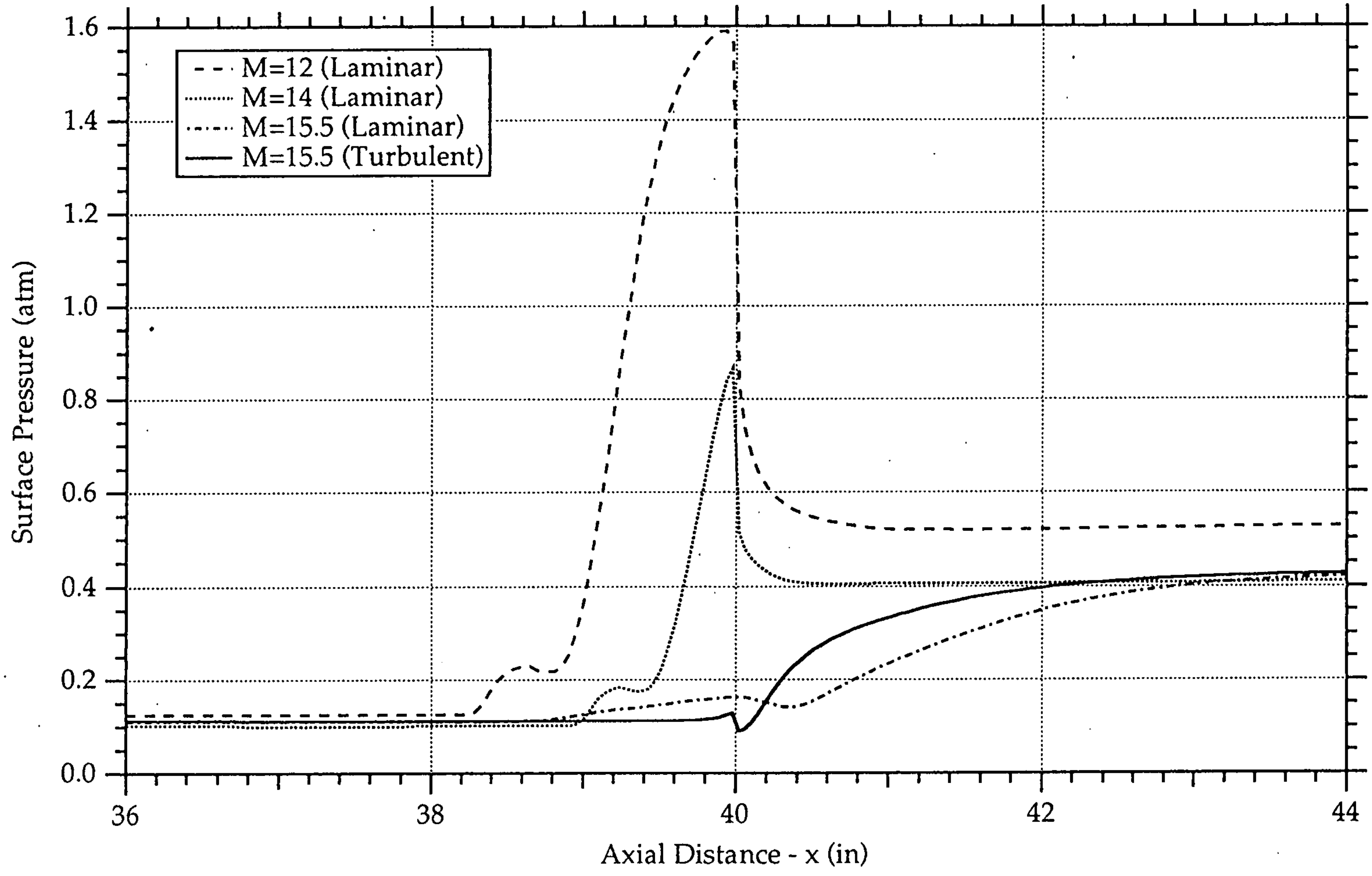

LOWER WALL - SURFACE PRESSURE (VISCOUS FLOW)
IMPINGEMENT STUDY - 2D COMBUSTOR MODEL
Driver Pressure = 408.2 atm

LOWER WALL - HEAT TRANSFER
IMPINGEMENT STUDY - 2D COMBUSTOR MODEL
Driver Pressure = 408.2 atm

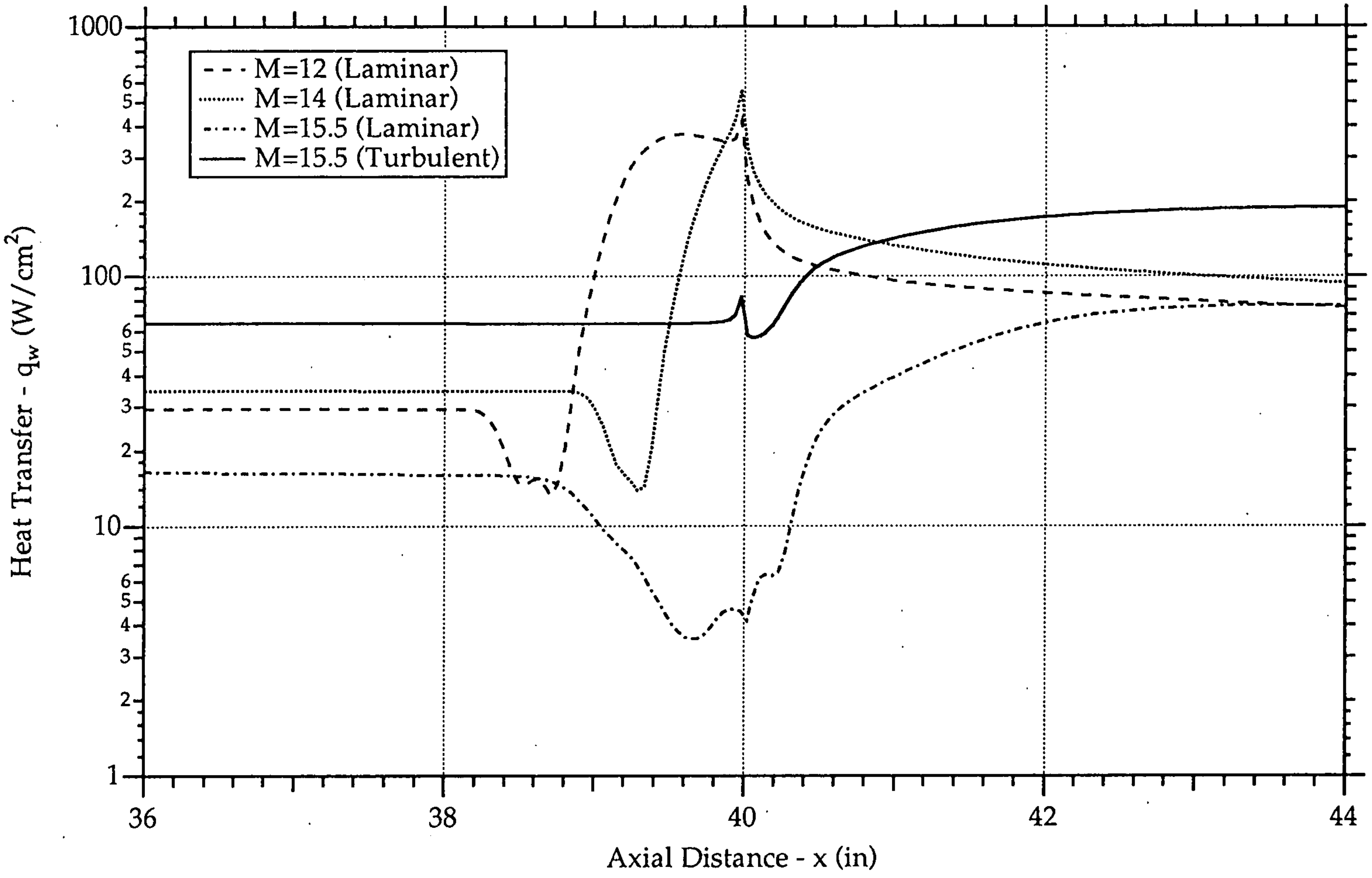

MACH PROFILES AT x = 40" - VISCOUS FLOW
IMPINGEMENT STUDY - 2D COMBUSTOR MODEL
Driver Pressure = 408.2 atm

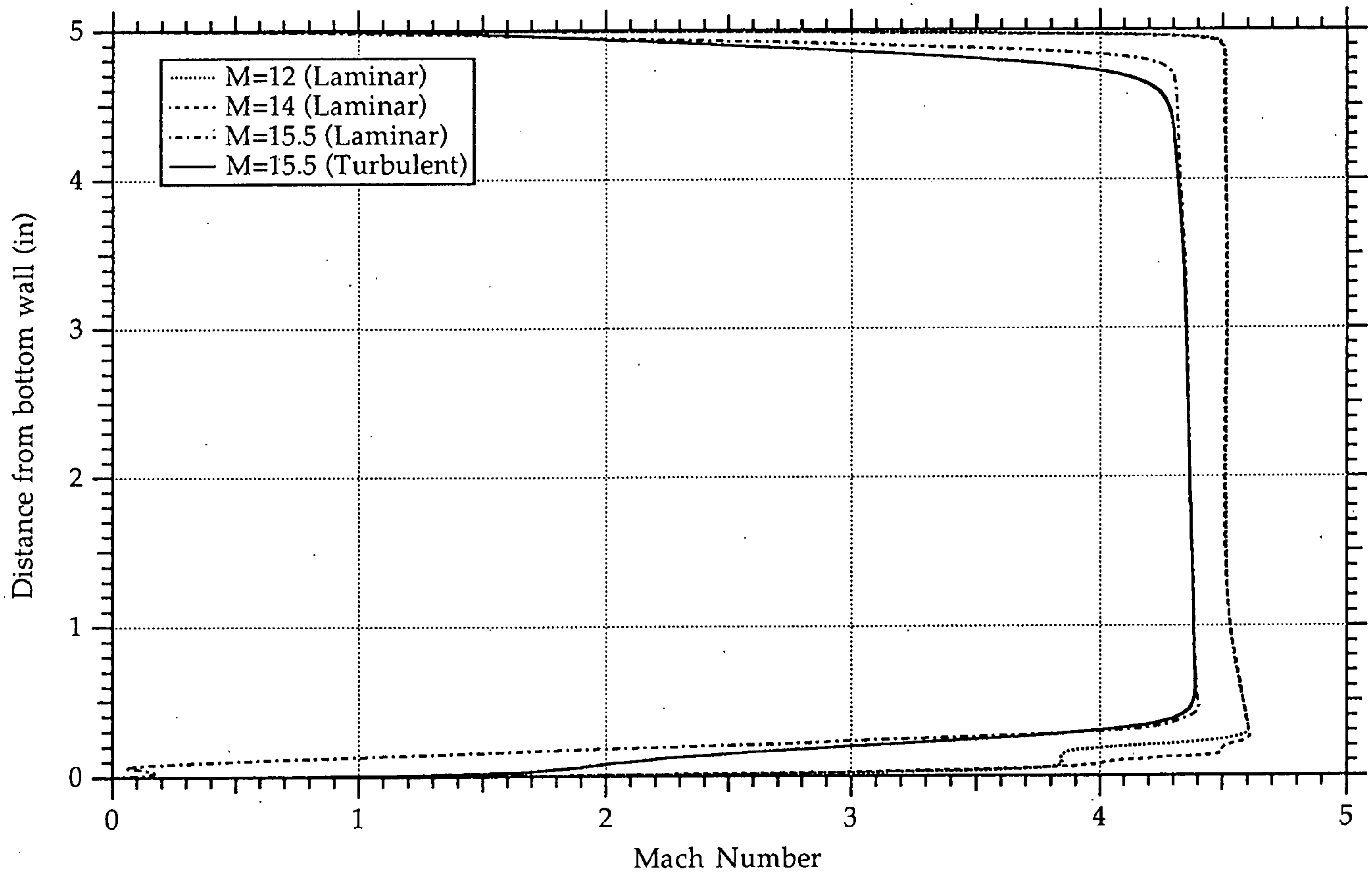

PRESSURE PROFILES AT x = 40" - VISCOUS FLOW
IMPINGEMENT STUDY - 2D COMBUSTOR MODEL
Driver Pressure = 408.2 atm

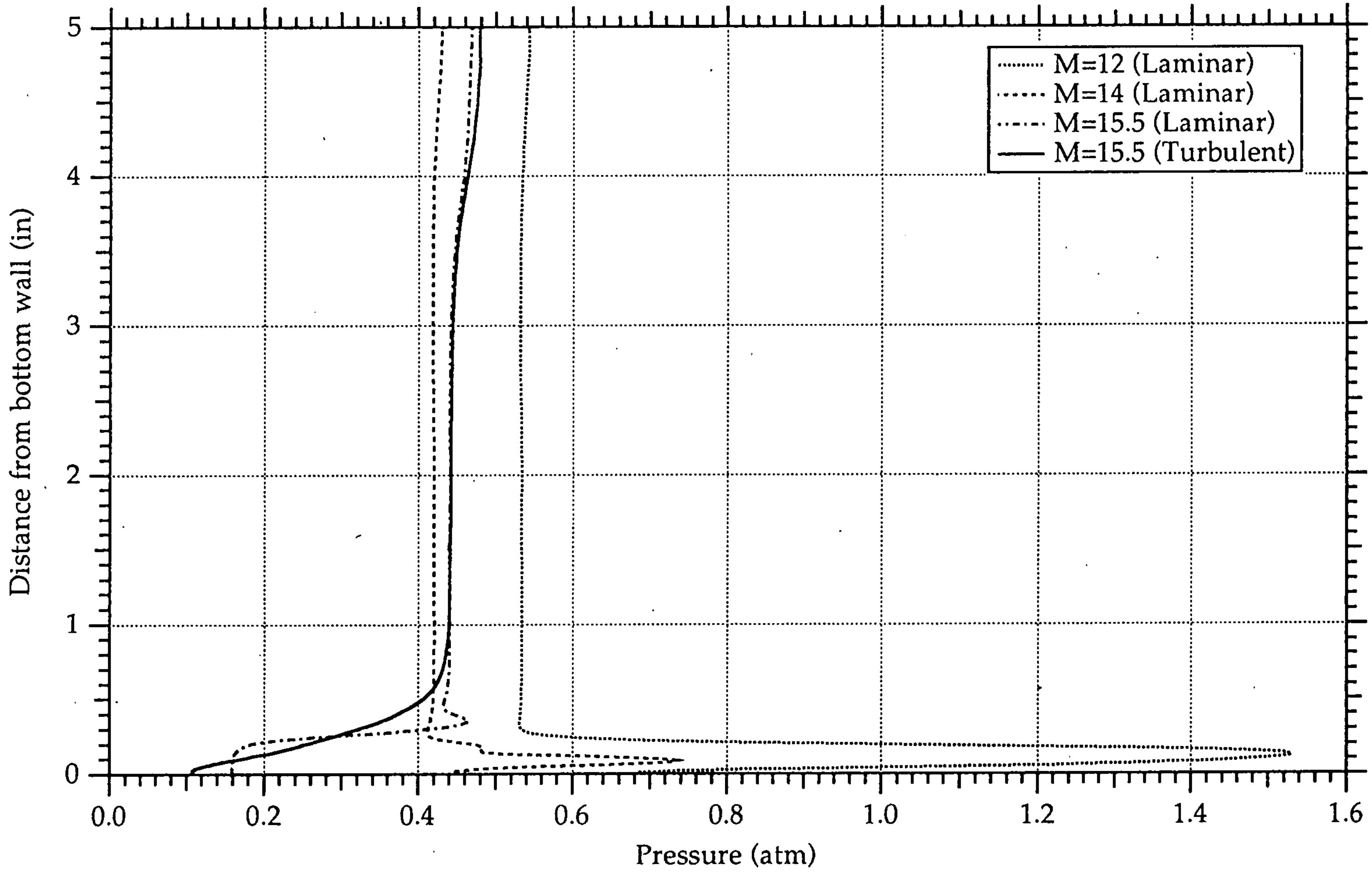

TEMPERATURE PROFILES AT x = 40" - VISCOUS FLOW
IMPINGEMENT STUDY - 2D COMBUSTOR MODEL
Driver Pressure = 408.2 atm

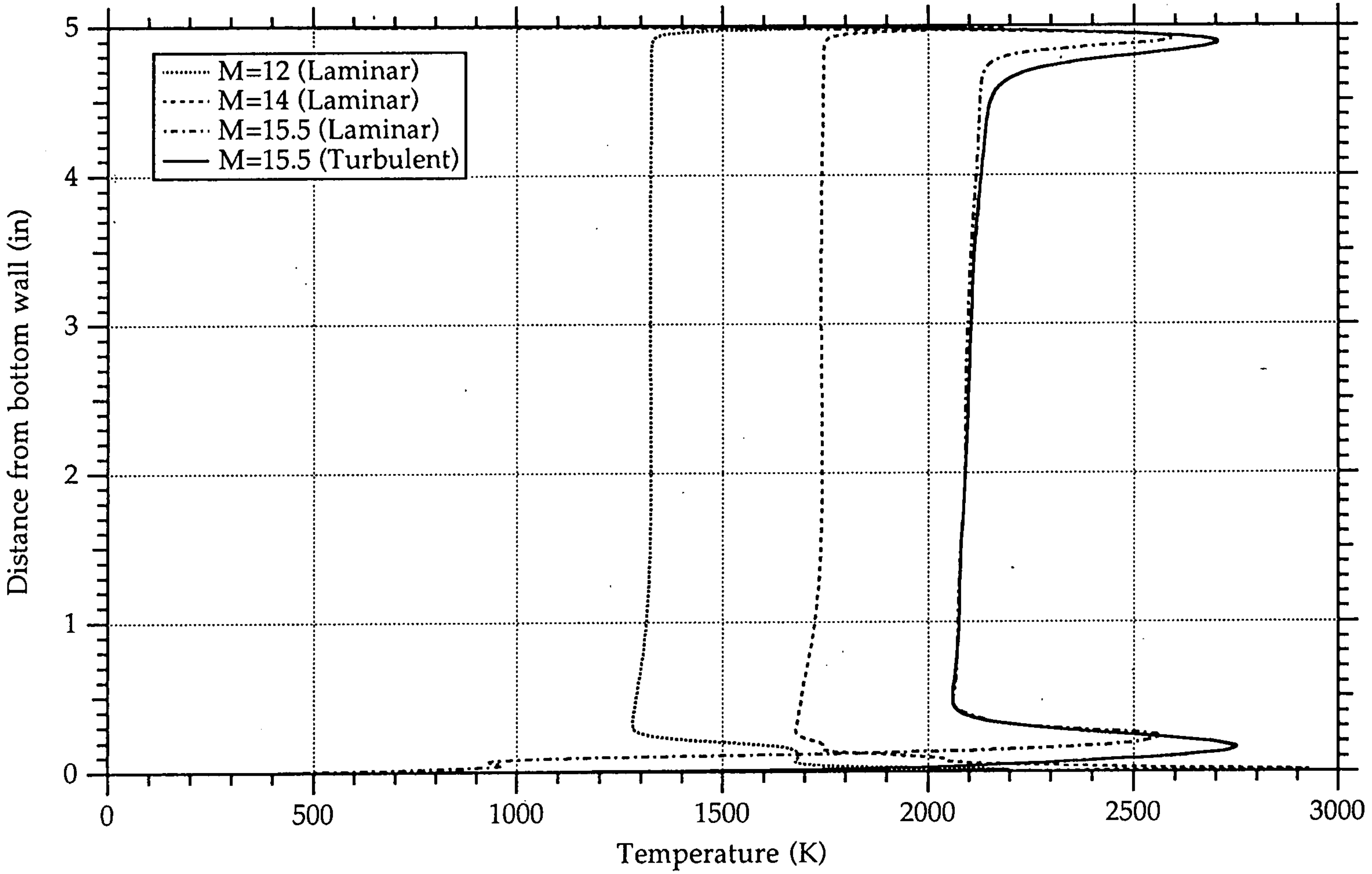

GRID SENSITIVITY ANALYSIS - LOWER WALL PRESSURE
IMPINGEMENT STUDY - 2D COMBUSTOR MODEL
Mach 15.5 Case, Turbulent Flow, Driver Pressure = 408.2 atm
p_∞ = 11.2 kPa, V_∞ = 4097.6 m/s, T_∞ = 1412 K

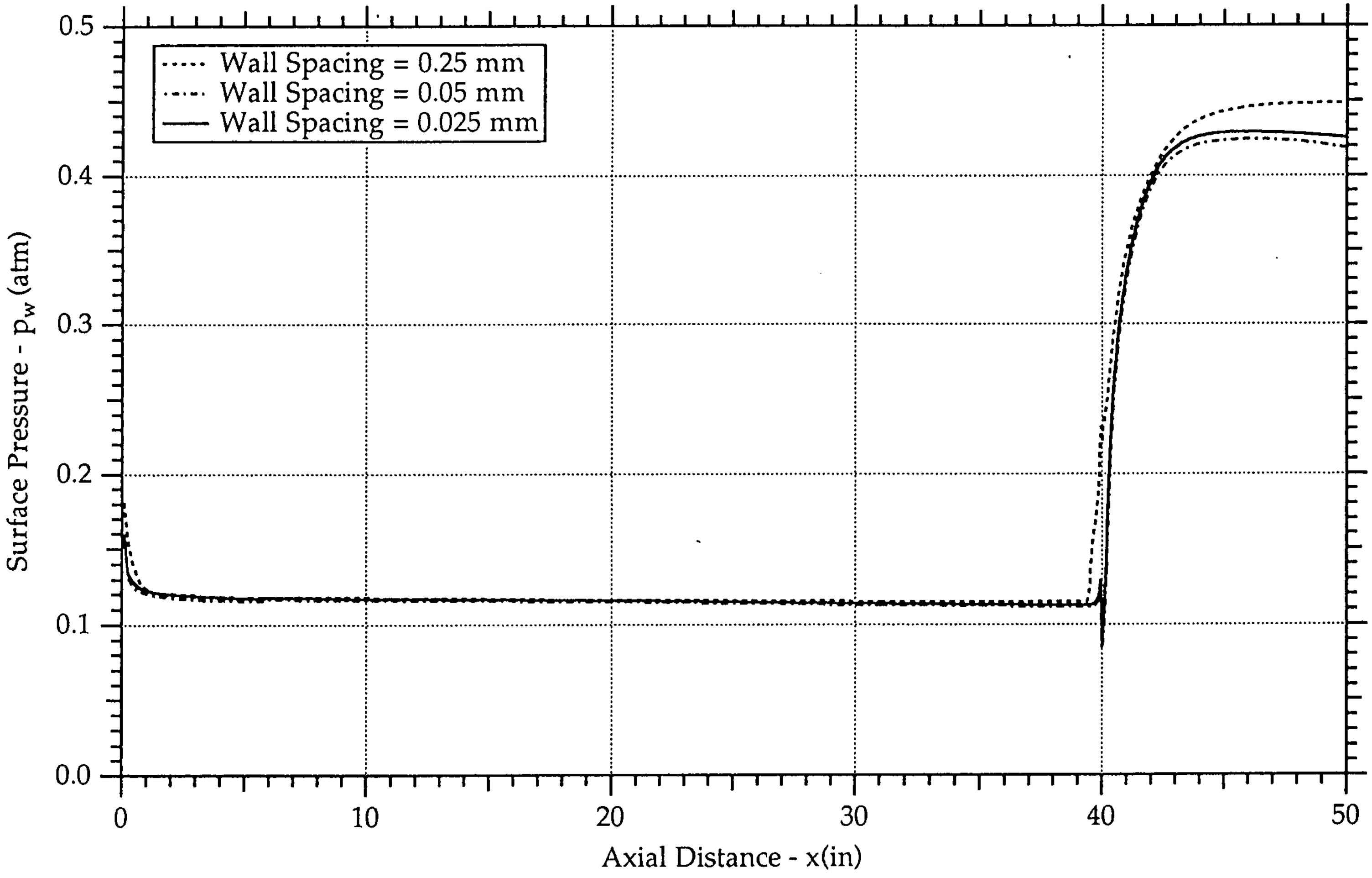

GRID SENSITIVITY ANALYSIS - LOWER WALL HEAT TRANSFER
IMPINGEMENT STUDY - 2D COMBUSTOR MODEL
Mach 15.5 Case, Turbulent Flow, Driver Pressure = 408.2 atm
$p_\infty = 11.2$ kPa, $V_\infty = 4097.6$ m/s, $T_\infty = 1412$ K

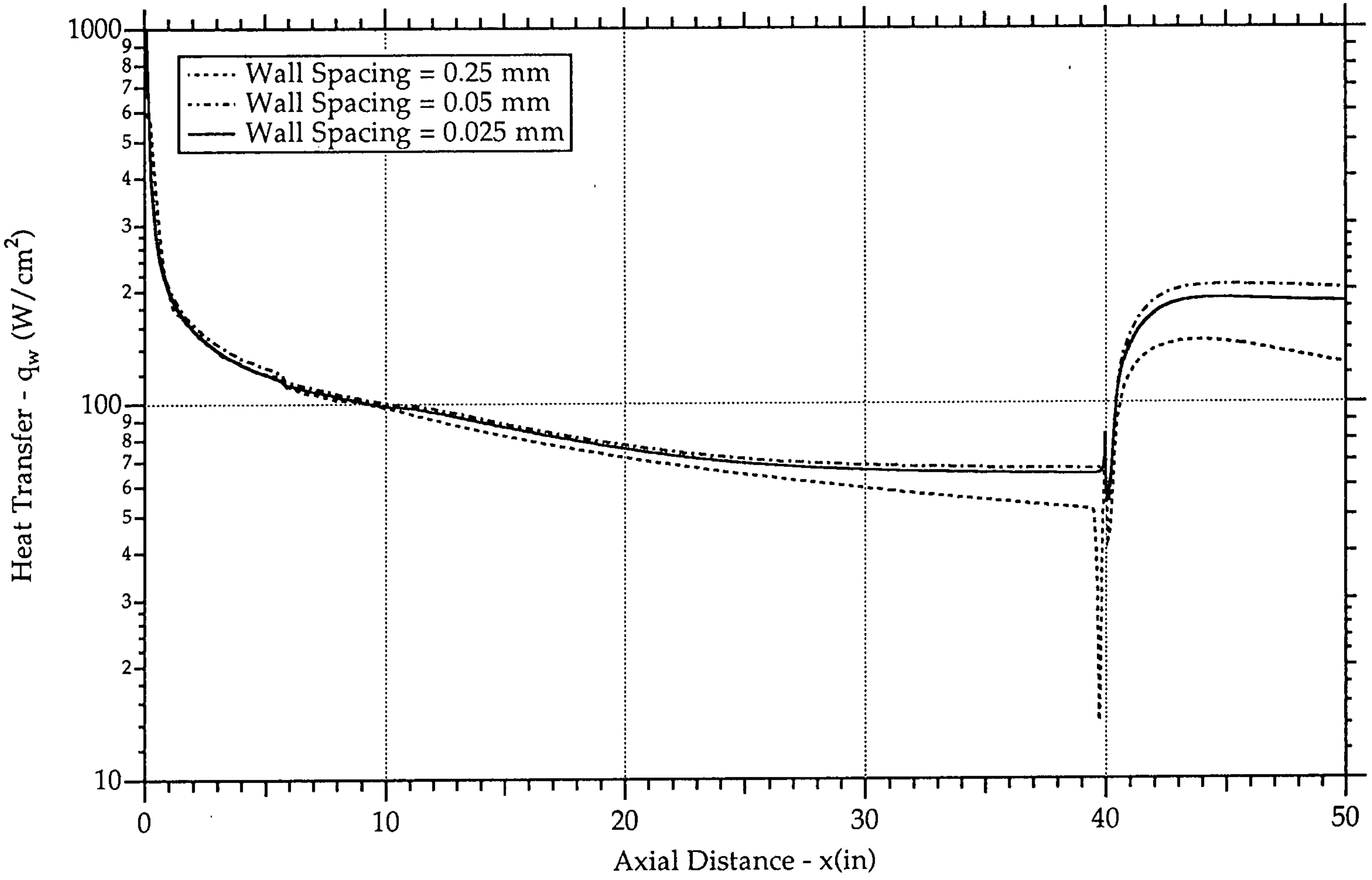

GRID SENSITIVITY ANALYSIS - LOWER WALL PRESSURE (CORNER DETAIL)
IMPINGEMENT STUDY - 2D COMBUSTOR MODEL
Mach 15.5 Case, Turbulent Flow, Driver Pressure = 408.2 atm
p_∞ = 11.2 kPa, V_∞ = 4097.6 m/s, T_∞ = 1412 K

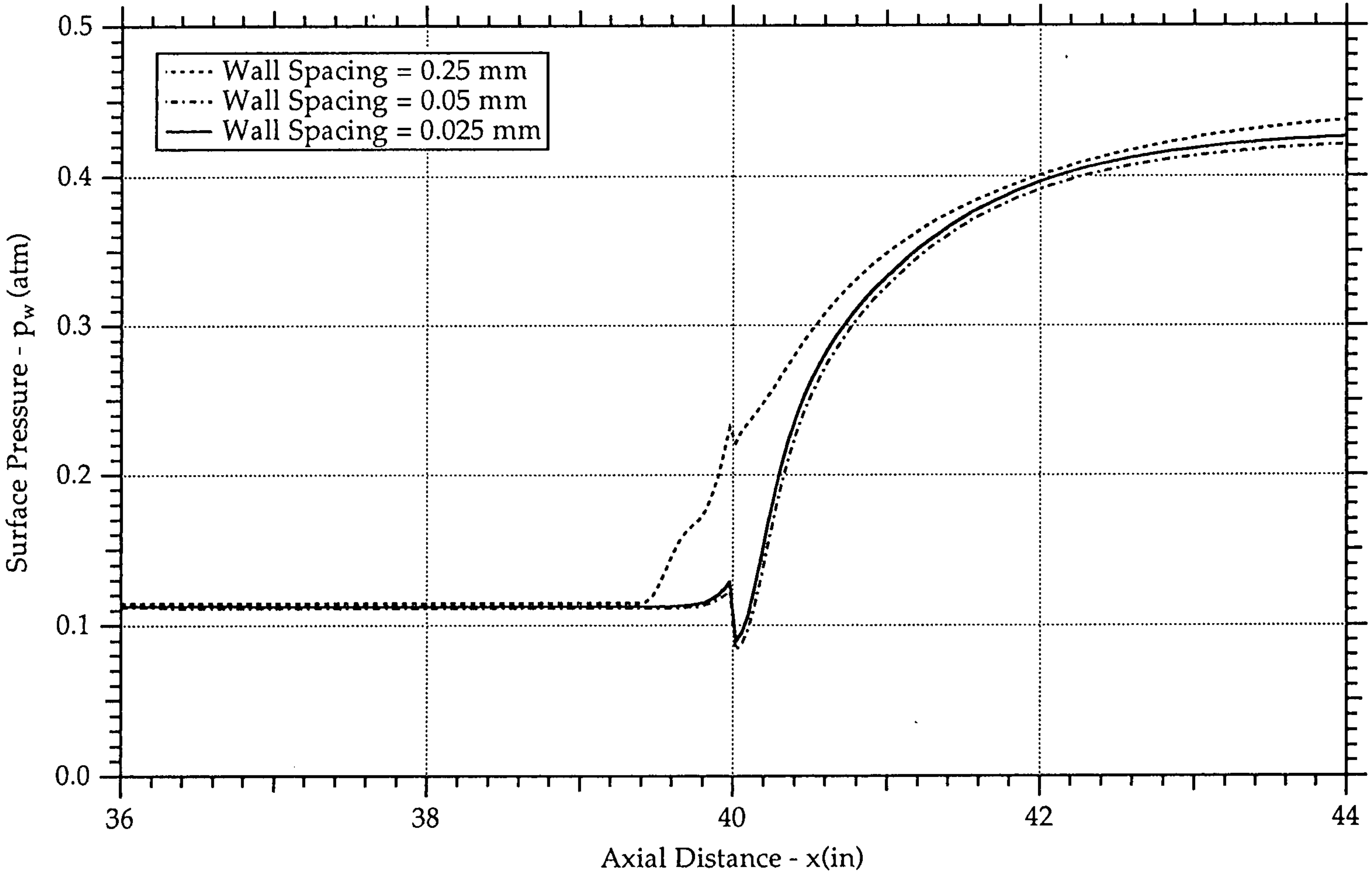

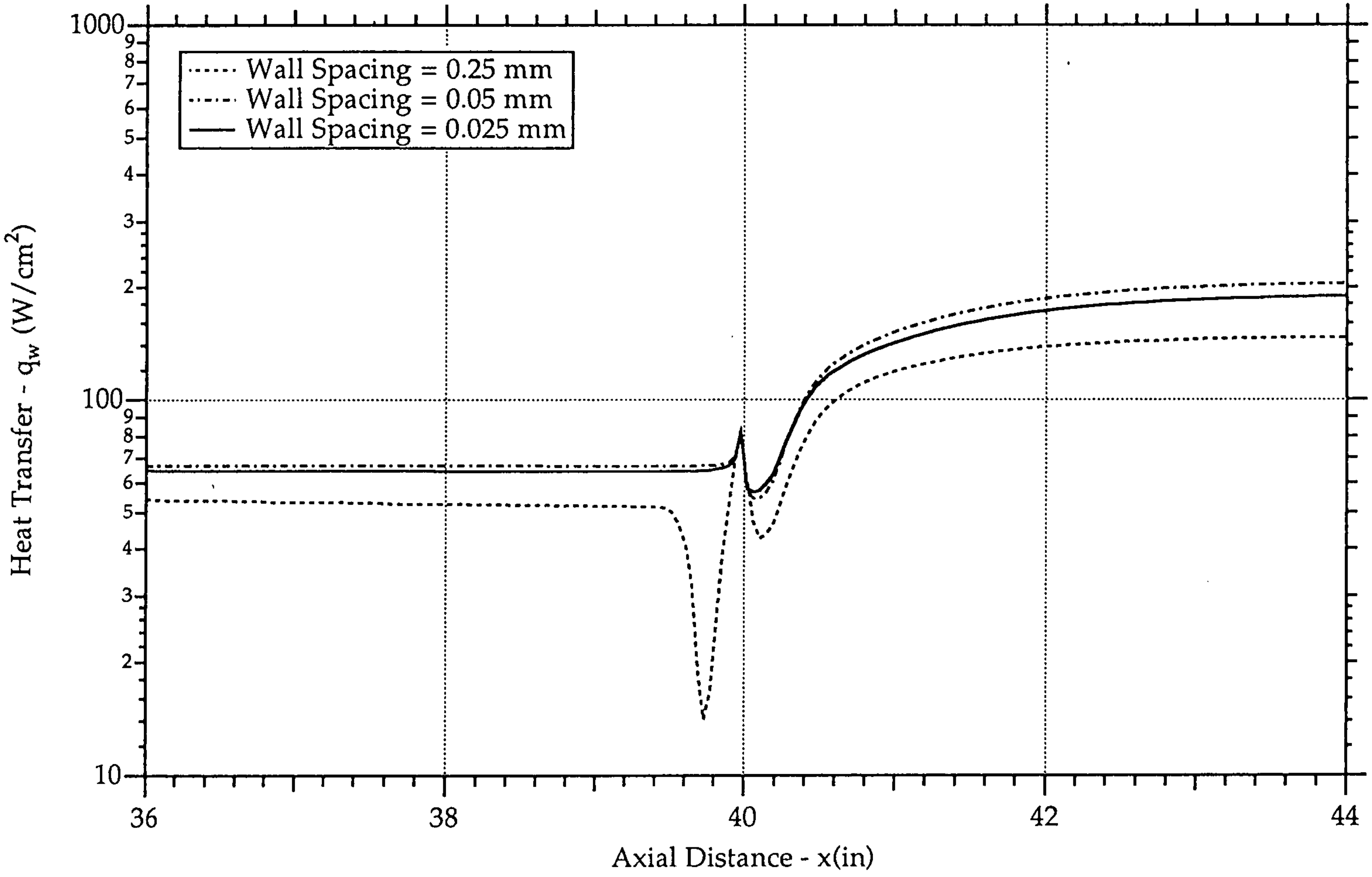

GRID SENSITIVITY ANALYSIS - LOWER WALL HEAT TRANSFER (CORNER DETAIL)
IMPINGEMENT STUDY - 2D COMBUSTOR MODEL
Mach 15.5 Case, Turbulent Flow, Driver Pressure = 408.2 atm
p_∞ = 11.2 kPa, V_∞ = 4097.6 m/s, T_∞ = 1412 K

GRID SENSITIVITY ANALYSIS - PRESSURE PROFILE AT x = 40"
IMPINGEMENT STUDY - 2D COMBUSTOR MODEL
Mach 15.5 Case, Turbulent Flow, Driver Pressure = 408.2 atm
p_∞ = 11.2 kPa, V_∞ = 4097.6 m/s, T_∞ = 1412 K

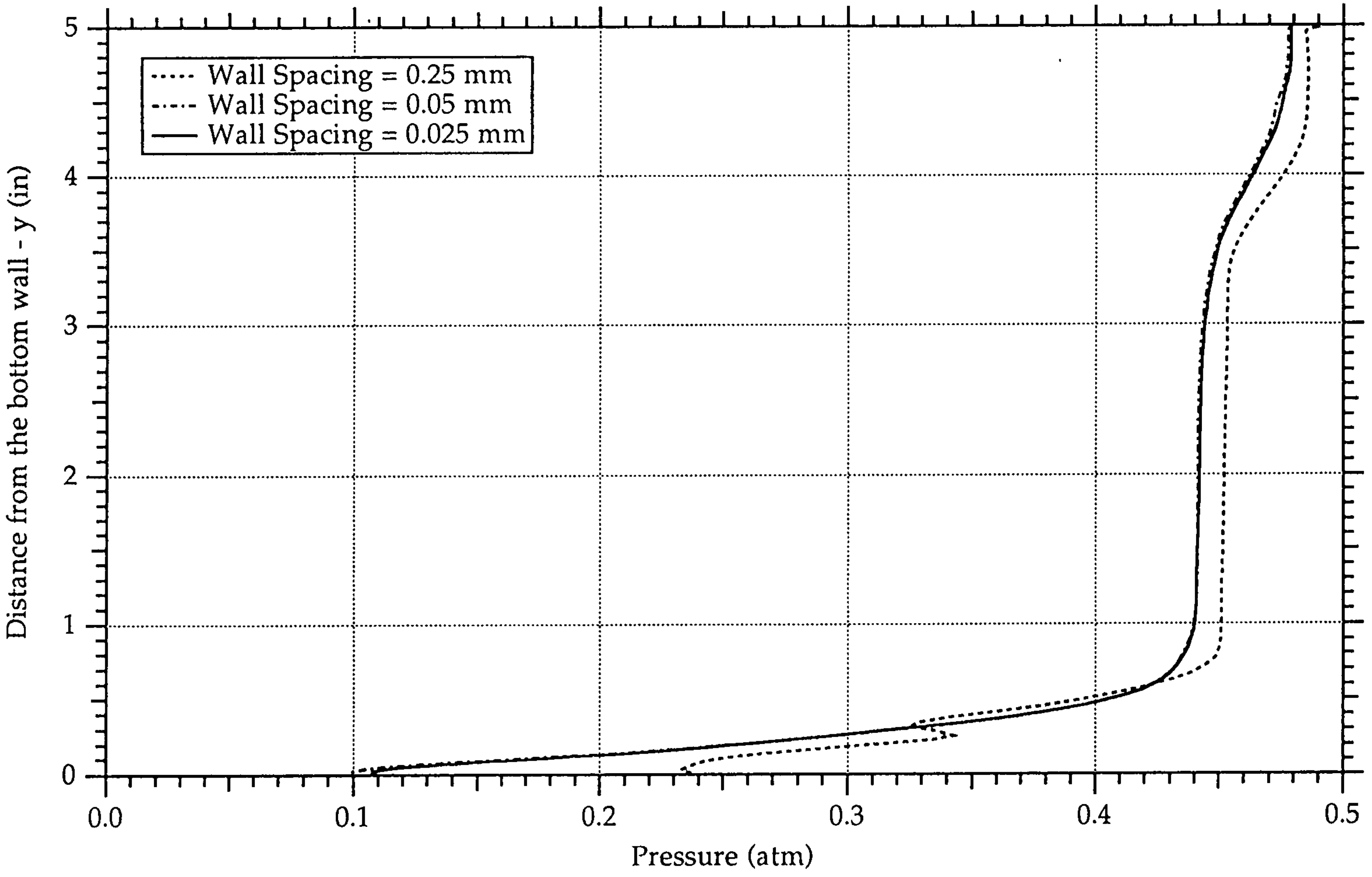

GRID SENSITIVITY ANALYSIS - MACH PROFILE AT x = 40"
IMPINGEMENT STUDY - 2D COMBUSTOR MODEL
Mach 15.5 Case, Turbulent Flow, Driver Pressure = 408.2 atm
p_∞ = 11.2 kPa, V_∞ = 4097.6 m/s, T_∞ = 1412 K

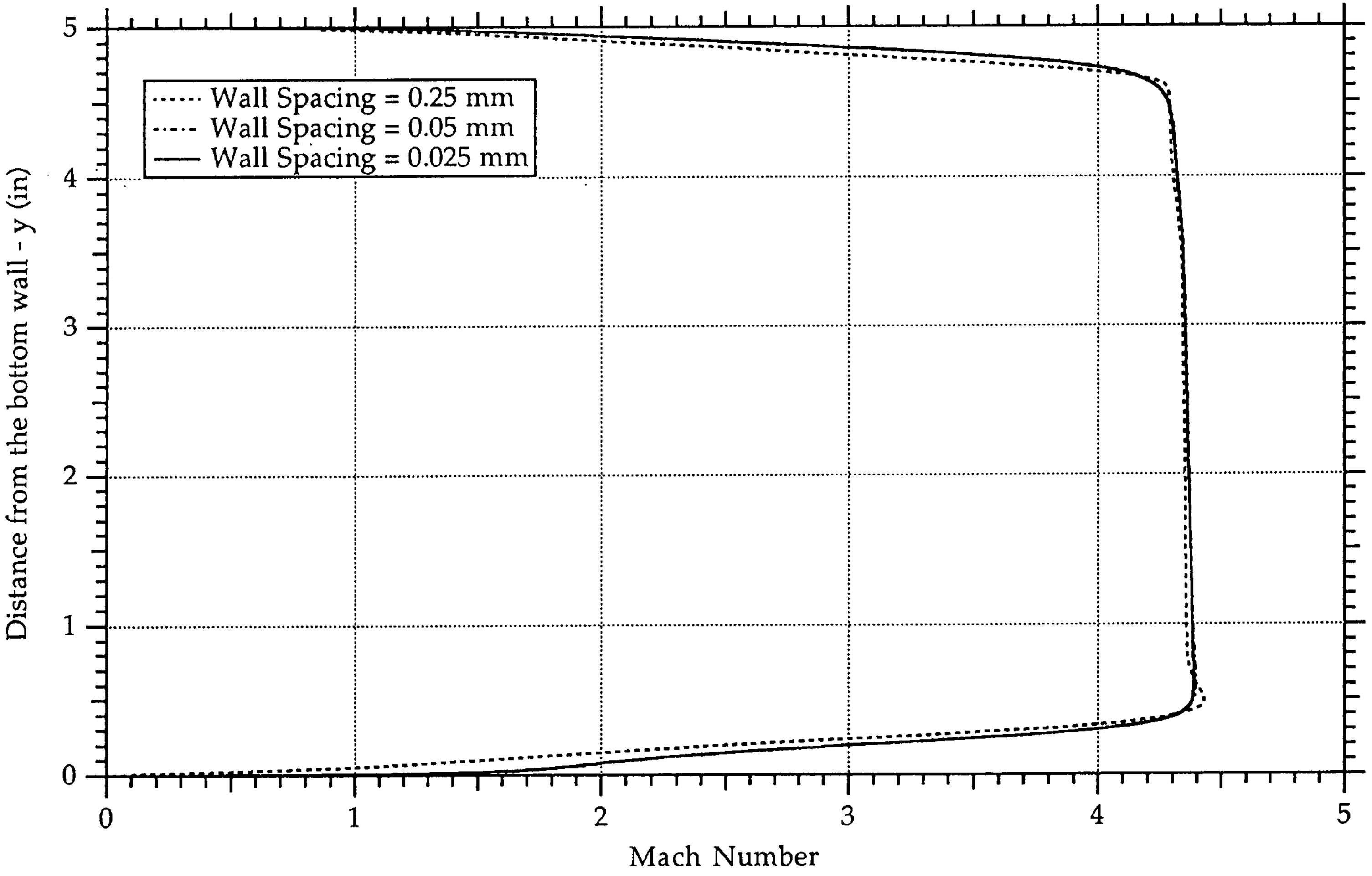

GRID SENSITIVITY ANALYSIS - TEMPERATURE PROFILE AT x = 40"
IMPINGEMENT STUDY - 2D COMBUSTOR MODEL
Mach 15.5 Case, Turbulent Flow, Driver Pressure = 408.2 atm
p_∞ = 11.2 kPa, V_∞ = 4097.6 m/s, T_∞ = 1412 K

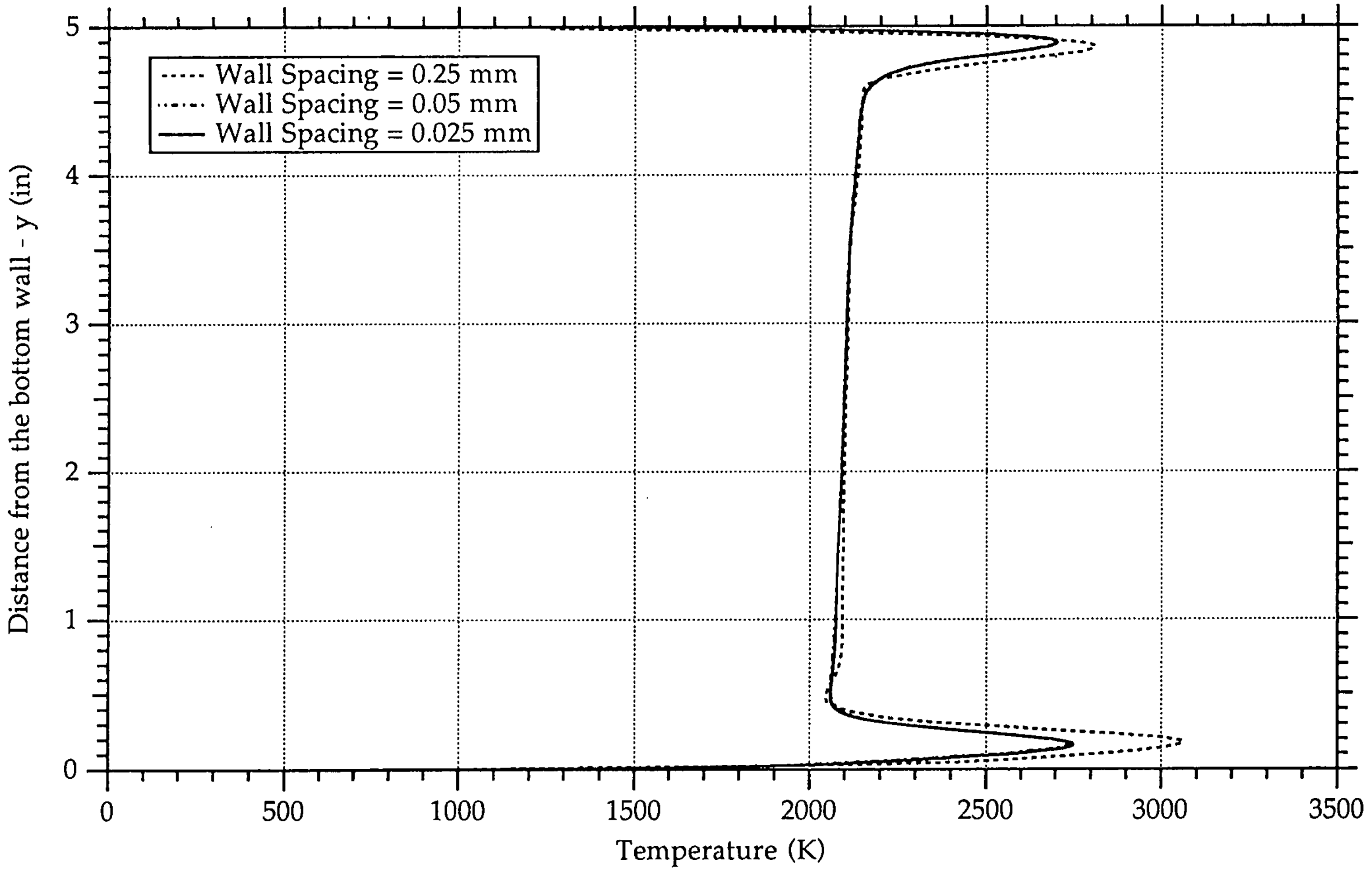

IMPINGEMENT STUDY - 2D COMBUSTOR MODEL
MACH CONTOURS FOR TURBULENT FLOW
M = 12, P = 544 atm, H = 6.6 MJ/kg

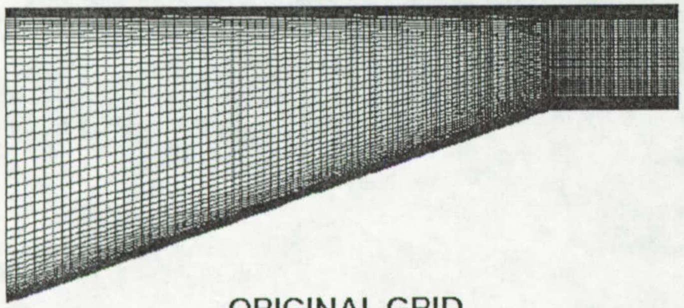

ORIGINAL GRID

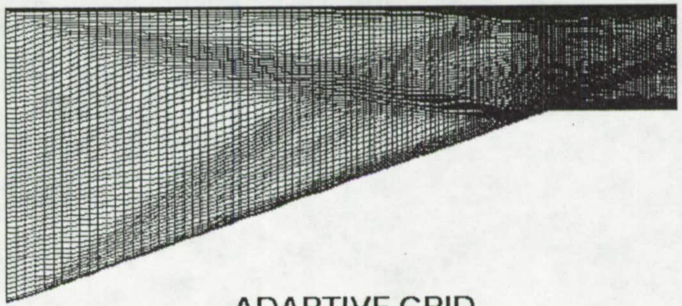

ADAPTIVE GRID

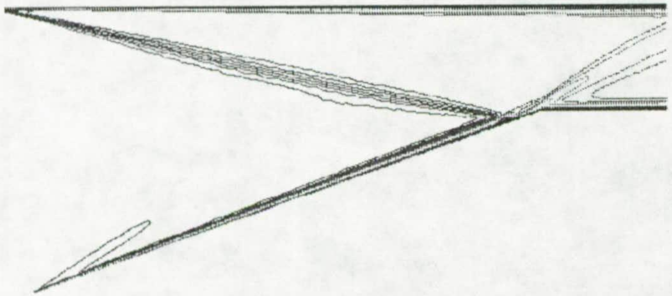

ORIGINAL SOLUTION

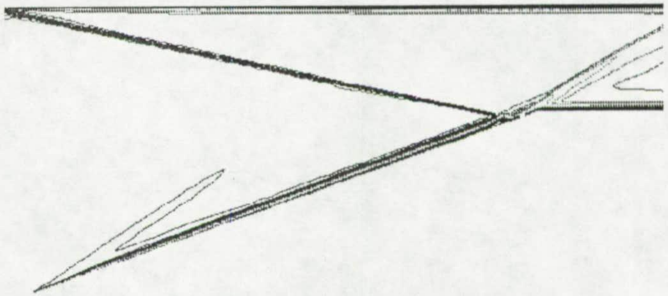

ADAPTIVE SOLUTION

ARC 16" SHOCK TUNNEL - NOZZLE DIAGNOSTICS
COMPUTED HIGH RESOLUTION SPECTRUM OF NO(γ) BAND SYSTEM AT STATION N3

QUASI-ONE DIMENSIONAL FLOW SOLUTION

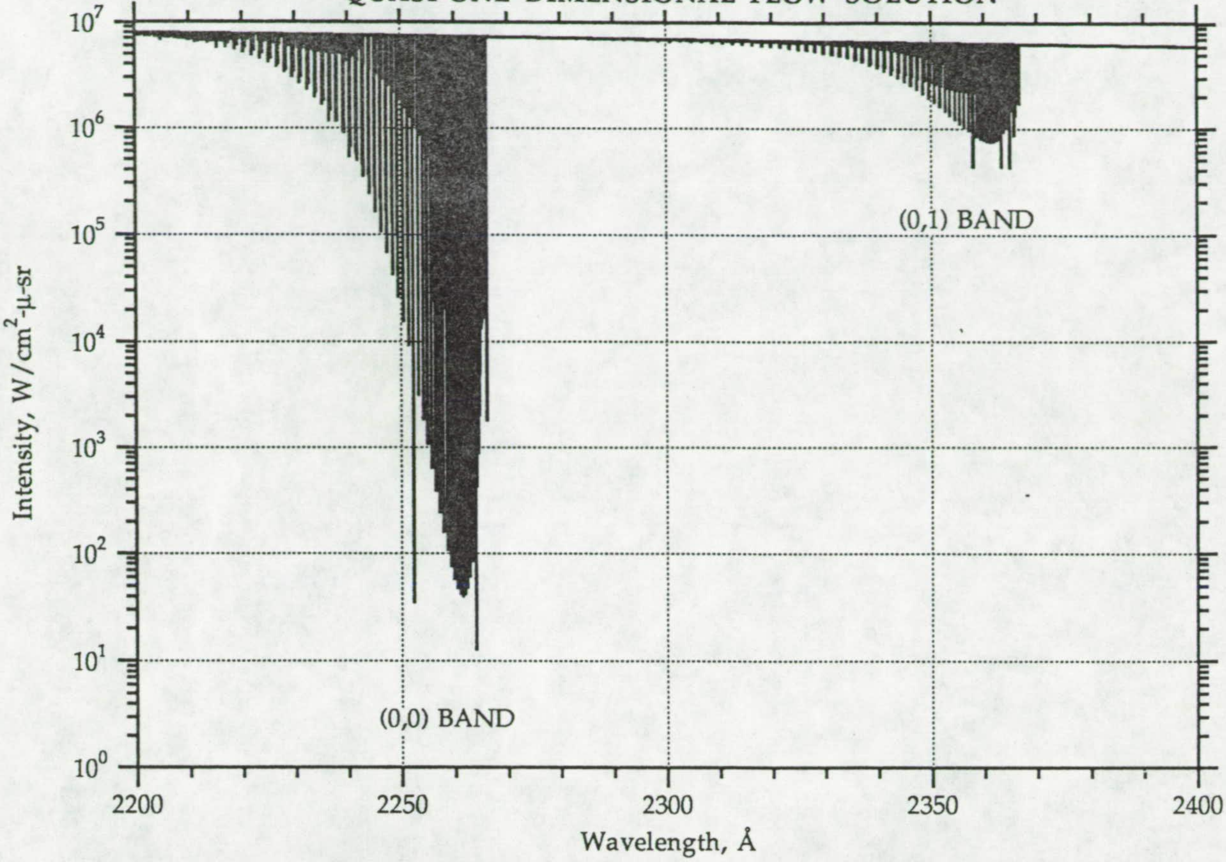

AXISYMMETRIC FLOW SOLUTION (WITHOUT BOUNDARY LAYER)

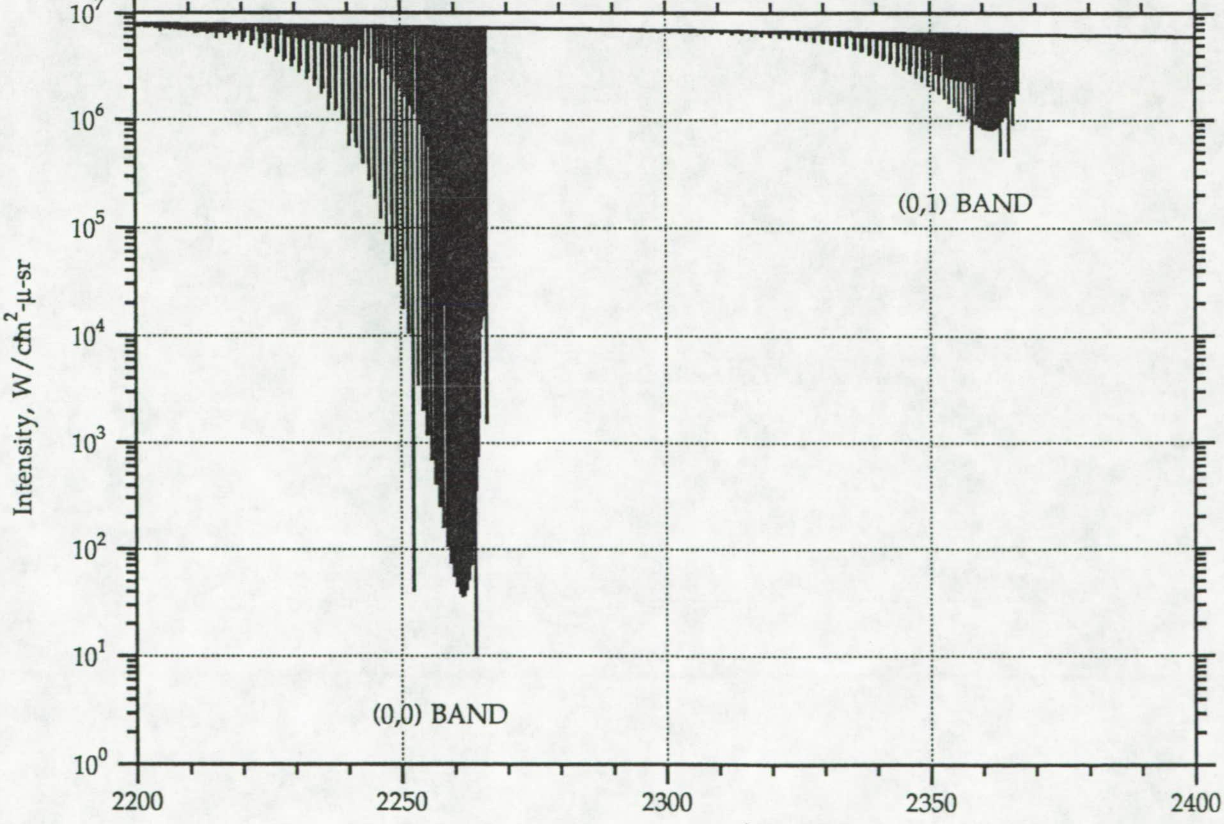

ARC 16" SHOCK TUNNEL
COMPUTED HIGH RESOLUTION SPECTRUM OF NO(γ) BAND SYSTEM AT STATION N3

QUASI-ONE DIMENSIONAL FLOW SOLUTION

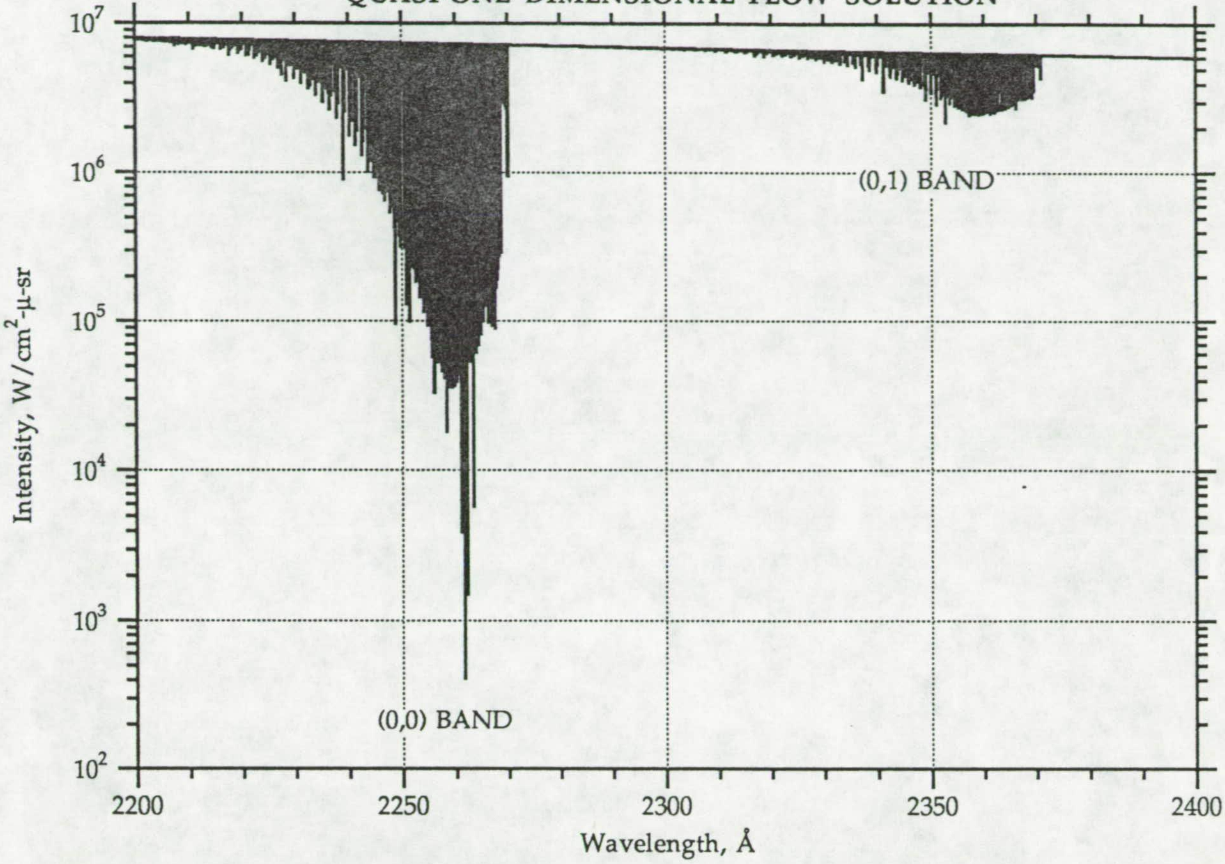

AXISYMMETRIC FLOW SOLUTION (WITHOUT BOUNDARY LAYER)

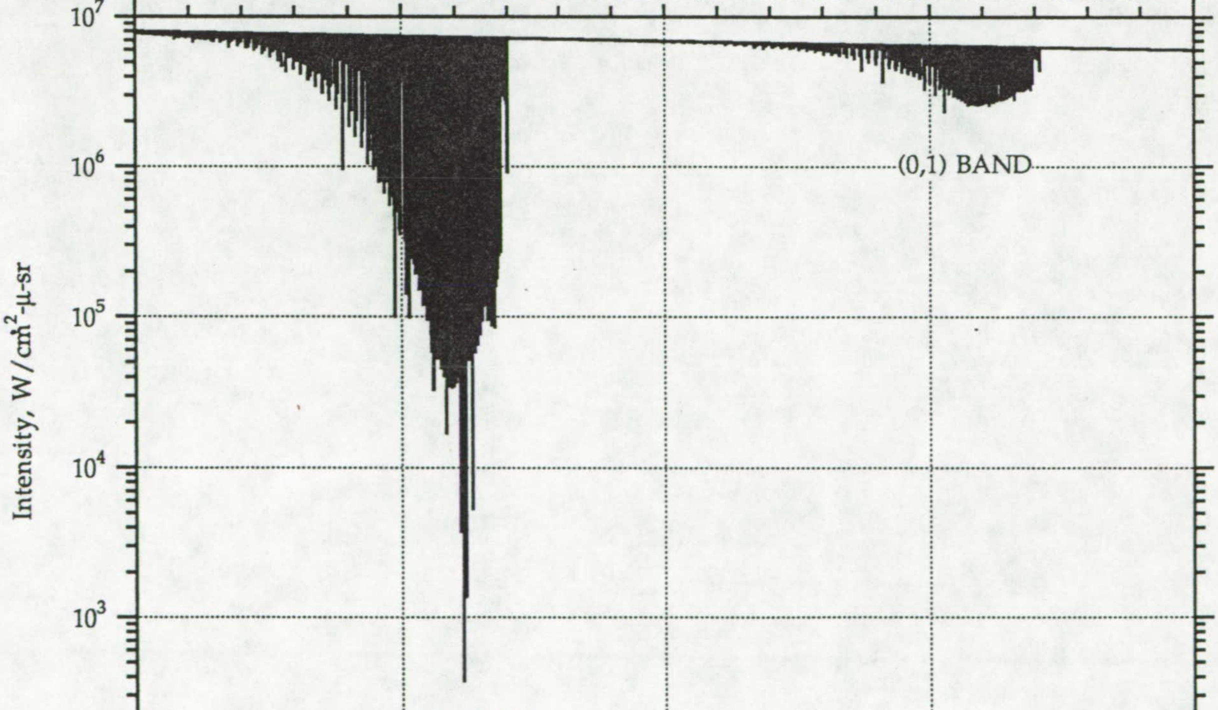

$^2\Sigma \rightarrow {}^2\Pi$

ARC 16" SHOCK TUNNEL - NOZZLE DIAGNOSTICS
COMPUTED HIGH RESOLUTION SPECTRUM OF NO(γ) BAND SYSTEM AT STATION N3
AXISYMMETRIC FLOW SOLUTION (WITH BOUNDARY LAYER)

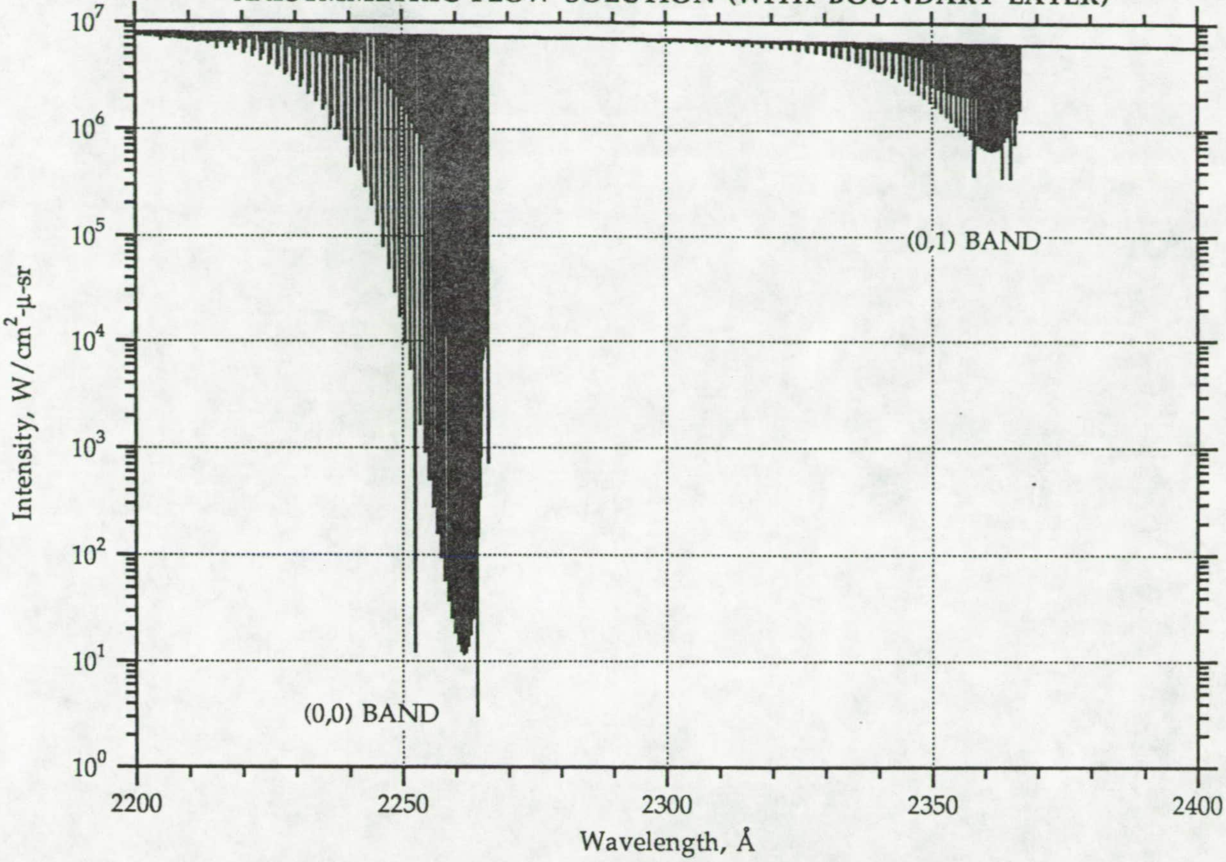

DETAILS OF THE (0,0) BAND SYSTEM - QUASI-1D FLOW

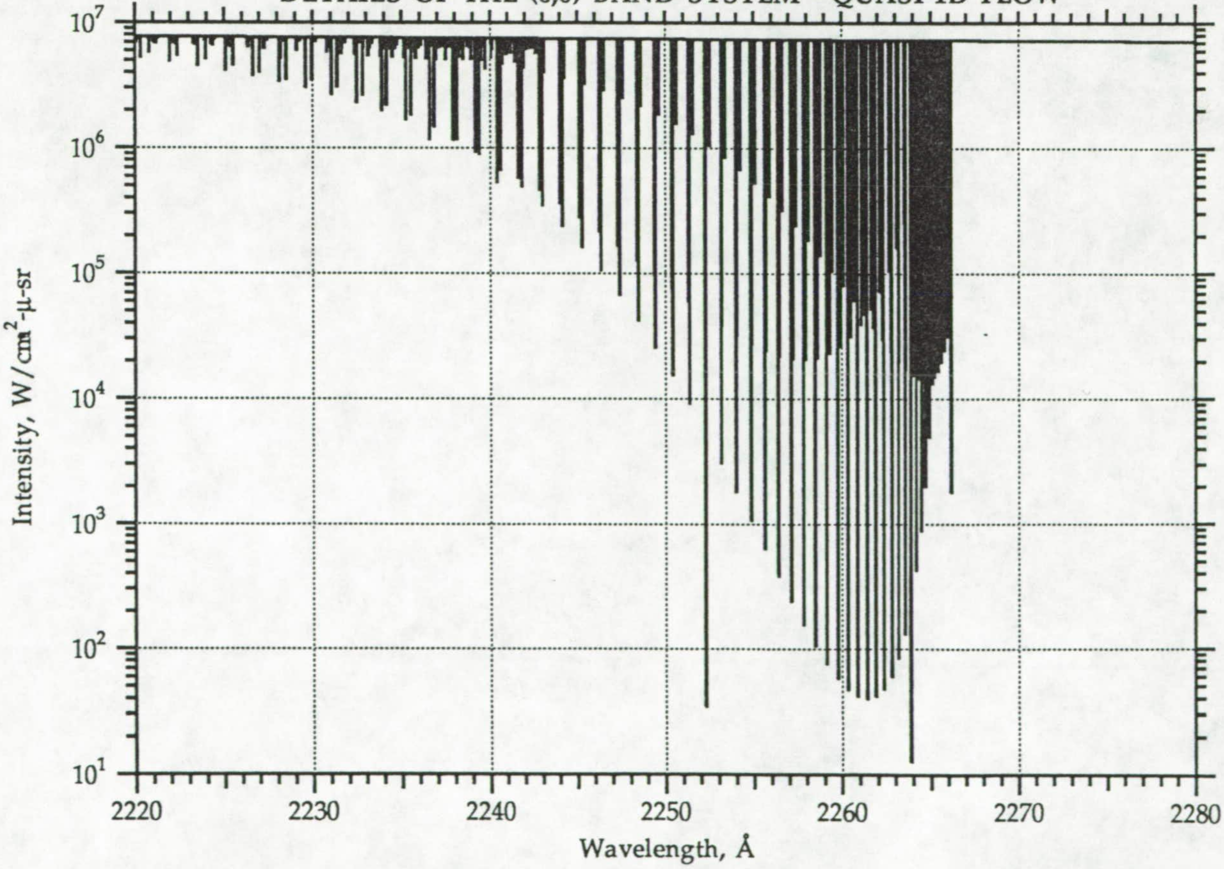

ARC 16" SHOCK TUNNEL
COMPUTED HIGH RESOLUTION SPECTRUM OF NO(γ) BAND SYSTEM AT STATION N3
AXISYMMETRIC FLOW SOLUTION (WITH BOUNDARY LAYER)

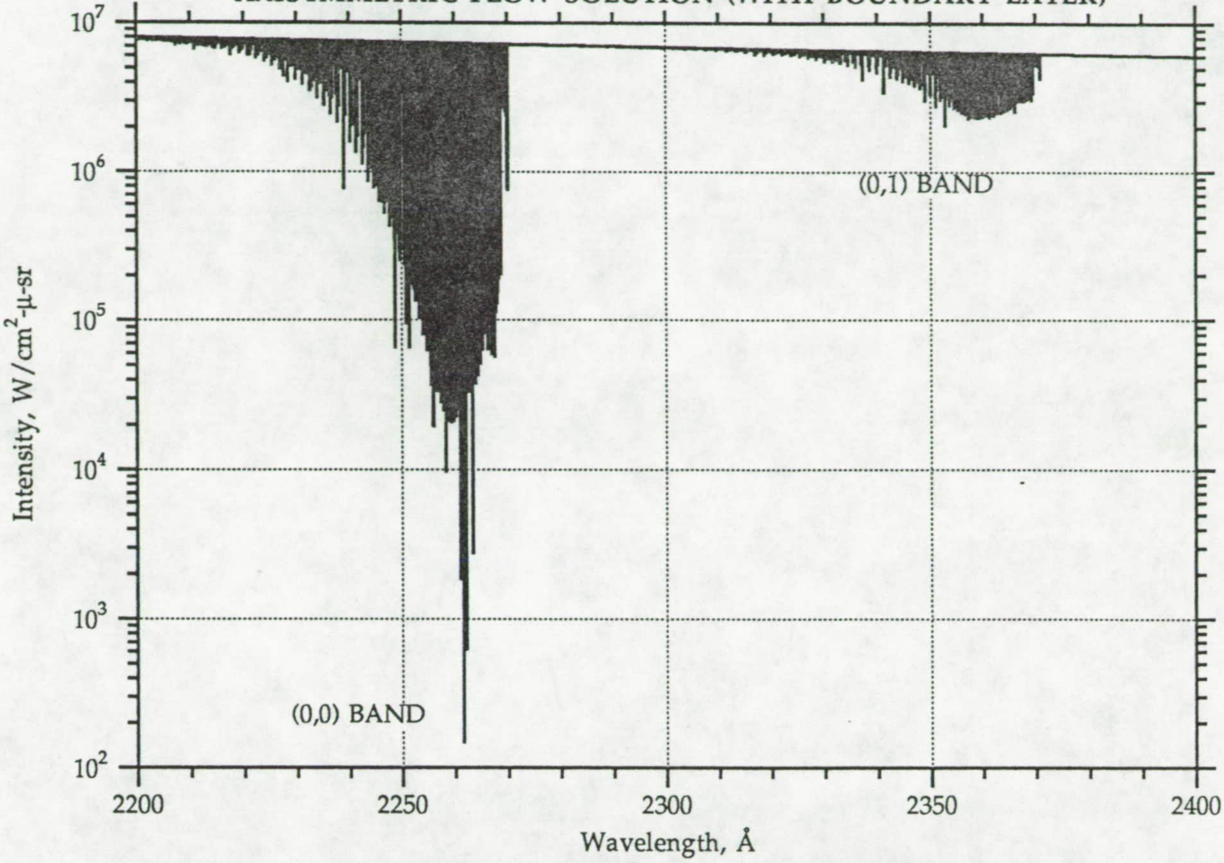

DETAILS OF THE (0,0) BAND SYSTEM - QUASI-1D FLOW

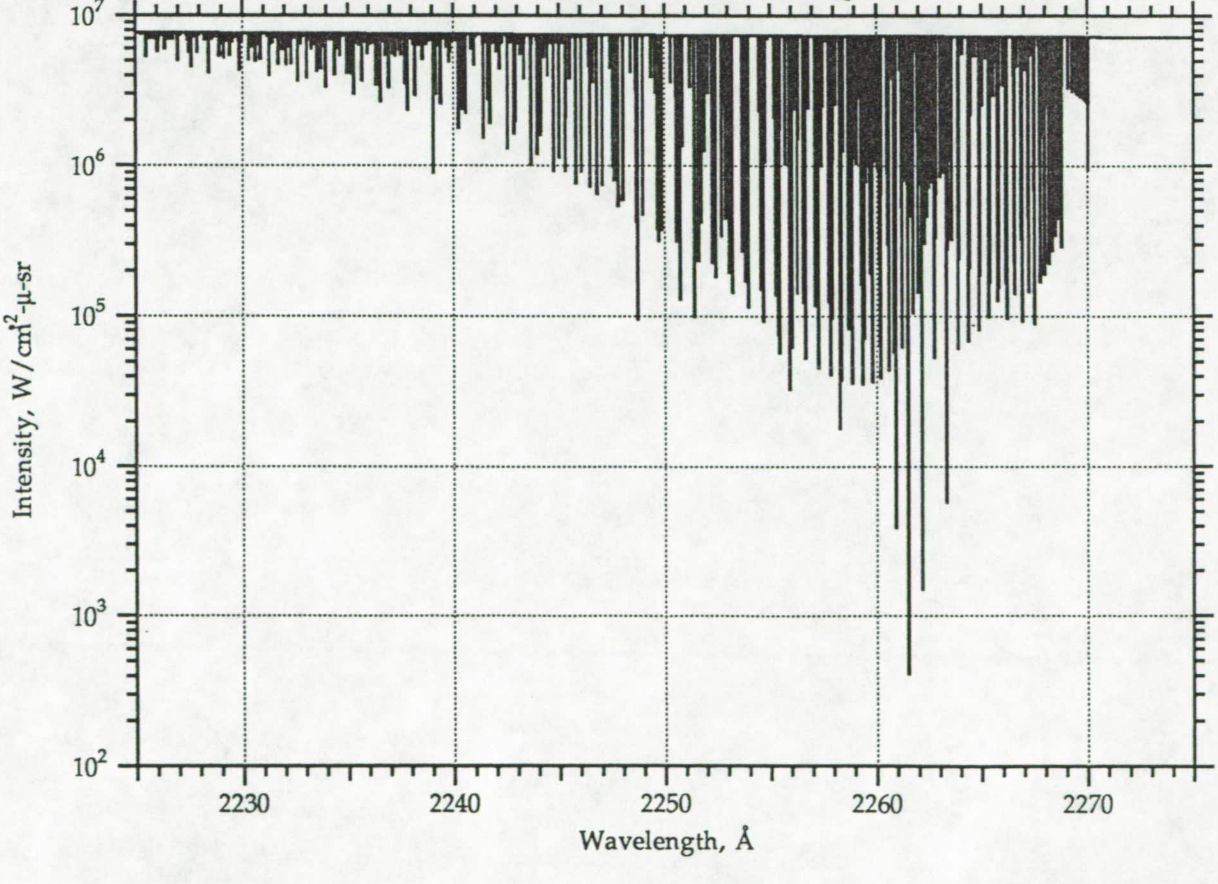

$^2\Sigma \rightarrow {}^2\Pi$

Appendix D

Susan Tokarcik

ELORET Research Institute, Palo Alto, Ca.

4/6/92

During the last work period, I worked on the following projects:

1. I participated in the Ames Technical Paper Contest for Women. I presented work on hypersonic drag devices. I was one of the winners of this contest and will be attending the Society of Women Engineers Conference in June to present my winning paper. Also, a paper on this material has been submitted to the Journal of Spacecraft and Rockets for publication.

2. I have also been working on computing the flowfield around a lunar return aerobrake concept proposed by Mike Tauber. I am working with E. Venketapathy on this project. Thus far an axisymmetric study of the aerobrake design has been completed for an aerobrake with flares at angles of 50°, 55°, and 60°. Three-dimensional calculations have also been completed at the same flare angles. It has been found that because of the large separated region created by the flares, the flow about the aerobrake is very complicated. Further investigation of this flow is anticipated and will include calculation of the base flow region. Comparisons between the axisymmetric solutions and the 3-D solutions have been made for surface pressure, size of the separated region, and total drag produced. Validation of the drag calculations and general flowfield character are to be completed by calculating a similar flowfield that has been studied experimentally. A representative picture of this work is shown in Figure 1.

3. I am continuing as point of contact for the University of Maryland. Maryland is involved in the CFD support effort for the Ames 16" shock tunnel. Thus far J.L. Cambier's axisymmetric TVD code (Emozart_2dA.f) has been transfered to the University of Maryland as well as the configuration of the ARC 16" shock tunnel nozzle and a generic combustor design. Cambier's 3-D code will eventually be transfered to the University of Maryland so that they can perform a full 3-D calculation of the test section flow with the combustor model in the test section. This study is being performed in order to determine the likelihood of choking the tunnel with the combustor model.

4. My involvement with the CFD support of the 16" shock tunnel has increased in the last six months

and will increase further when D. Prabhu leaves the project. I am also working with J.L. Cambier on this project A fully turbulent, nonequilibrium chemistry calculation of the nozzle flow has been completed. Information from this solution was used to characterize the flow in the test section and also to determine the optical character of the flow in the nozzle. A study of grid effects on the start-up solution has also been performed. This study was done assuming an inviscid, non-reacting flow. This start-up process begins at the breaking of the the diaphragm between the driven tube and the nozzle throat. A representative figure demonstrating grid effects is shown in Figure 2. A study of the entire start up procedure for a "best case" grid was also completed. This was also for inviscid, non-reacting flow. Figure 3. shows a time history of the start-up procedure.

A study of the applicability of calculating quasi-one-dimensional (Q-1D) flow of a reacting gas in order to simulate the full axisymmetric, turbulent solution was performed. It is shown that by decreasing the nozzle radius by 13% (an 87% nozzle), the flow in the turbulent, reacting case could be simulated successfully at a fraction of the CPU time required for the axisymmetric calculation. The results of this study are shown in Figure 4. Note that the Q-1D solution gives no information about boundary layer thickness or core flow profiles. This study will be continued further in order to determine if some "rules of thumb" exist for simulating axisymmetric, turbulent flows with finite rate chemistry with a Q-1D code with finite rate chemistry. The Q-1D code is also being used to study the effects of varying the chemical reaction rates for the reactions taking place in the nozzle.

Another study being done at this time is the simulation of the full driver tube, driven tube and nozzle flows in a time accurate manner. This simulation is axisymmetric, turbulent, and has finite rate chemistry. A representative figure of this flow is shown in Figure 5. In this figure, the diaphragm between the driver tube and the driven tube has partially ruptured and a shock has formed in the driven tube.

The results completed thus far for the Ames 16" shock tunnel will be presented at the AIAA Thermophysics Conference in July.

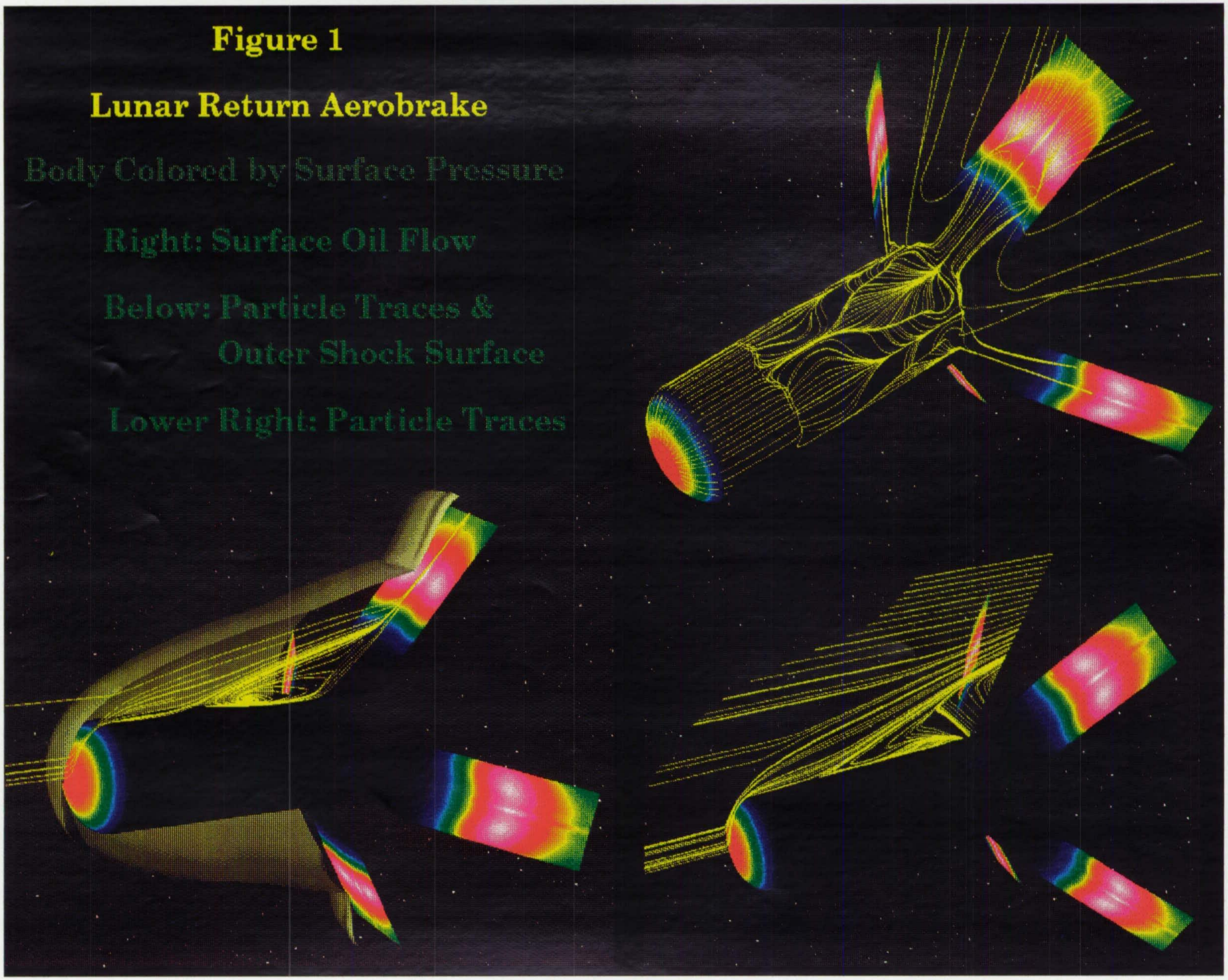

Figure 1

Lunar Return Aerobrake

Body Colored by Surface Pressure

Right: Surface Oil Flow

Below: Particle Traces &
Outer Shock Surface

Lower Right: Particle Traces

Figure 2

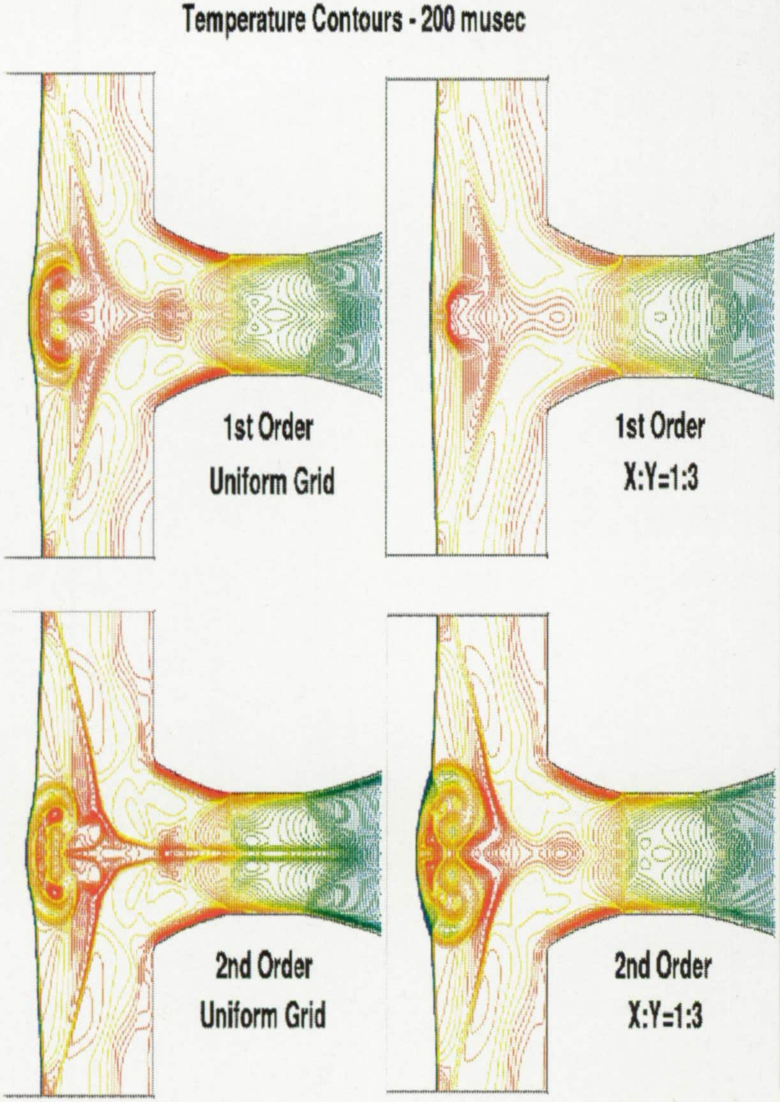

Temperature Contours - 200 musec

1st Order Uniform Grid

1st Order X:Y=1:3

2nd Order Uniform Grid

2nd Order X:Y=1:3

Figure 3

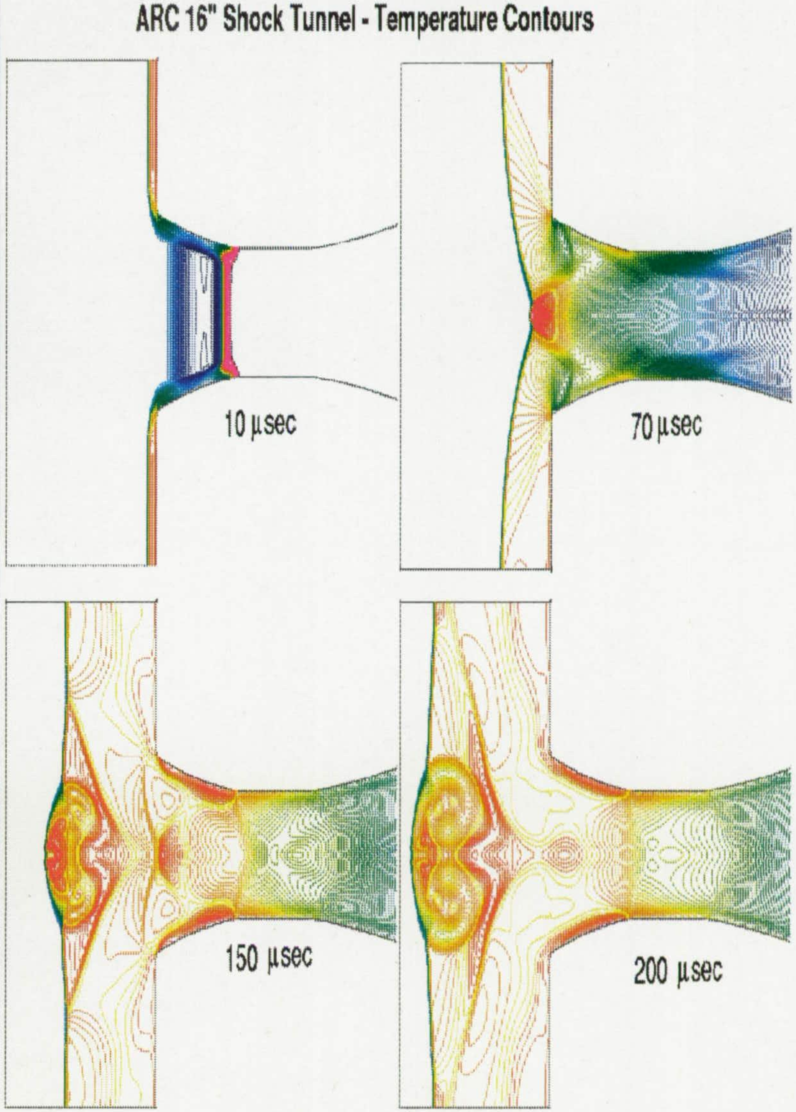

ARC 16" Shock Tunnel - Temperature Contours

10 µsec

70 µsec

150 µsec

200 µsec

ORIGINAL PAGE
COLOR PHOTOGRAPH

Fig. 4

ARC 16" SHOCK TUNNEL - PROFILES AT NOZZLE EXIT
A/A^* (geometric) = 169.8, R = 49.53 cm
Shock Speed = 3.0 km/s, Reservoir Pressure = 420.5 atm

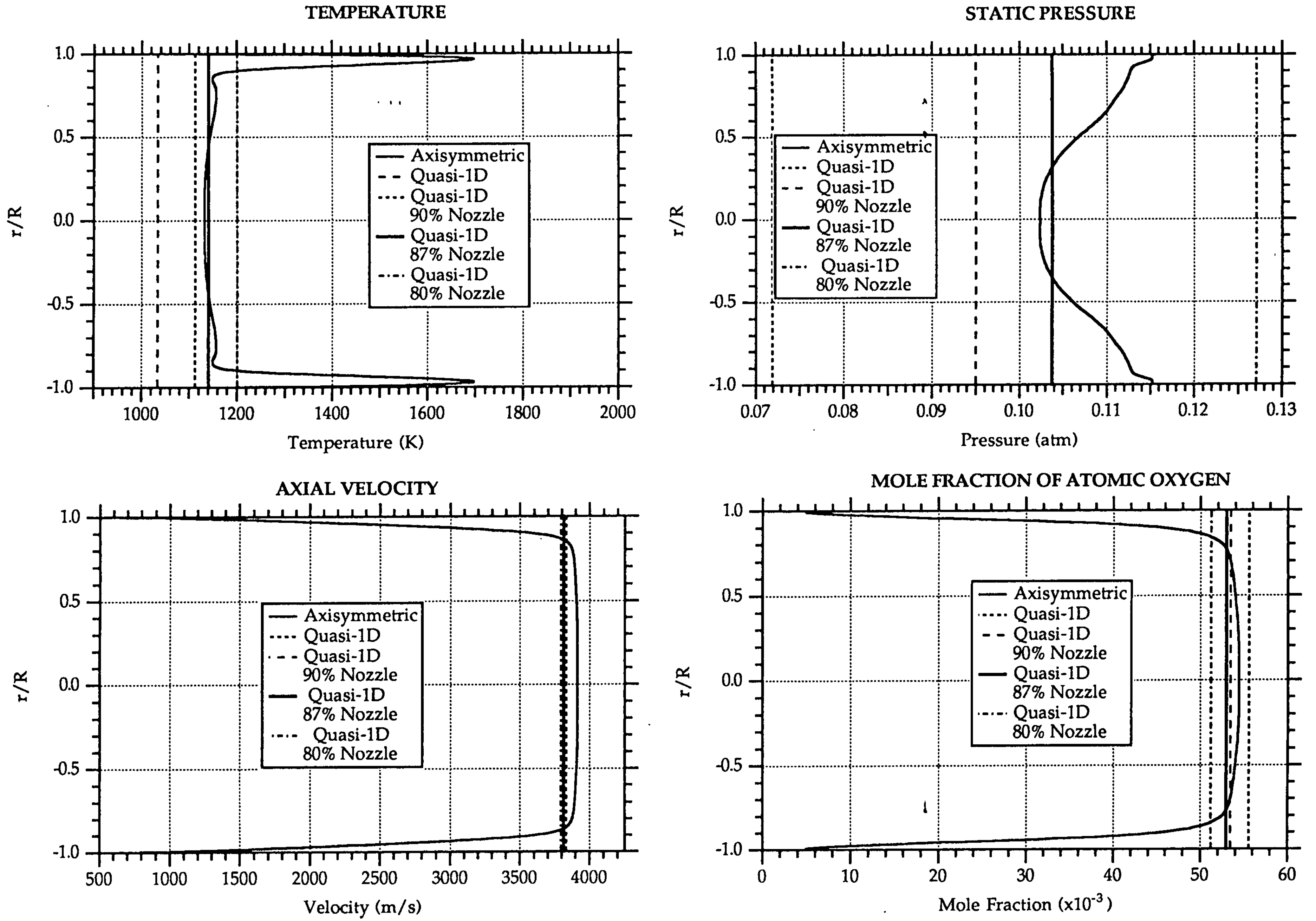

Figure 5

Temperature Contours of Driver - Driven Section with Diaphragm Partially Open

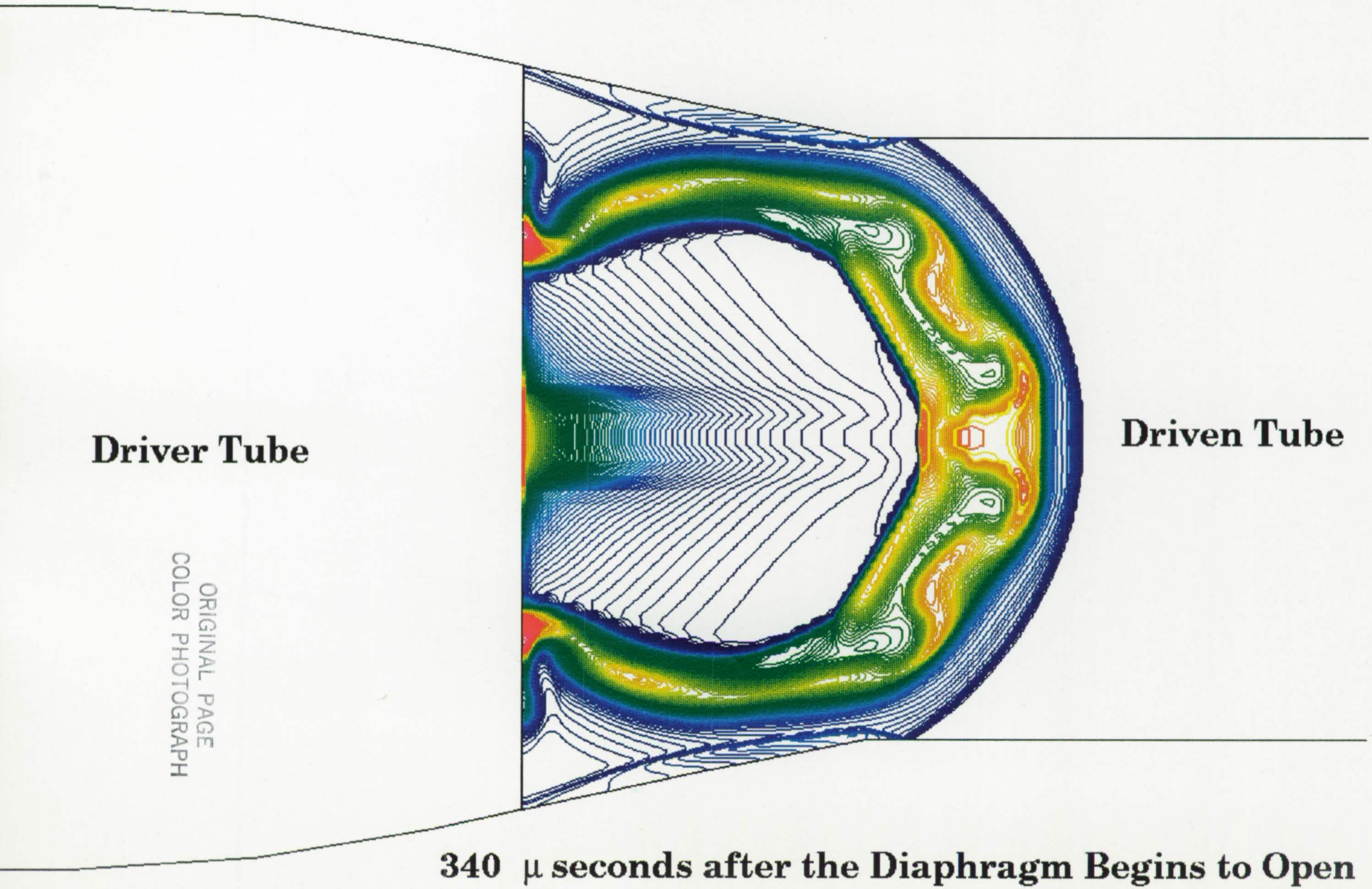

340 μ seconds after the Diaphragm Begins to Open

Appendix E

AIAA 92-0387
SINGLE EXPANSION RAMP NOZZLE SIMULATIONS

S.M. Ruffin
NASA Ames Research Center
Moffett Field, CA

E. Venkatapathy, S.H. Lee,
E.R. Keener
Eloret Institute
Palo Alto, CA

F.W. Spaid
McDonnell Douglas Research Laboratories
St. Louis, MO

30th Aerospace Sciences
Meeting & Exhibit
January 6-9, 1992 / Reno, NV

SINGLE EXPANSION RAMP NOZZLE SIMULATIONS

Stephen M. Ruffin*
Aerothermodynamics Branch
NASA Ames Research Center
Moffett Field, California

Ethiraj Venkatapathy*
Seung-Ho Lee*
Earl R. Keener*
Eloret Institute
Palo Alto, California

Frank W. Spaid**
McDonnell Douglas Research Laboratories
St. Louis, MO

ABSTRACT

The single-expansion-ramp-nozzle (SERN) experiment underway at NASA Ames Research Center simulates the National Aerospace Plane propulsive jet-plume flow. Recently, limited experimental data has become available from an experiment with a generic nozzle/afterbody model in a hypersonic wind tunnel. The present paper presents full three-dimensional solutions obtained with the implicit Navier-Stokes solver, FL3D, for the baseline model and a version of the model with side extensions. Analysis of the computed flow clearly shows the complex 3-D nature of the flow, critical flow features, and the effect of side extensions on the plume flow development. Flow schematics appropriate for the conditions tested are presented for the baseline model and the model with side extensions. The computed results show excellent agreement with experimental shadowgraph and with surface pressure measurements. The computed and experimental surface oil-flows show the same features but may be improved by appropriate turbulence modeling.

I. INTRODUCTION TO THE SERN EXPERIMENT

Hypersonic air-breathing vehicles, such as the proposed National Aerospace Plane (NASP), require an efficient integration of propulsion and aerodynamic systems. A major element of the integrated design is the interaction between the jet-plume flow, the external flow, and the afterbody. The afterbody is designed as a single- (or one-sided) expansion-ramp-nozzle (SERN) to minimize friction drag while extracting thrust from the high pressure flow on the afterbody. This complex interaction can significantly alter the thrust, aerodynamic stability and overall performance of the NASP.

Existing ground-based test facilities can only simulate some aspects of the hypersonic flight environment. Therefore, accurate and validated computational fluid dynamics (CFD) codes are needed to provide simulations of realistic flight conditions. The experimental validation data should, of course, model as many of the realistic flight conditions as possible. The validated codes can then be used to provide the most reliable predictions of the increments in performance or design parameters associated with the differences between the available test conditions and the flight environment.

An experiment has been conducted at NASA Ames Research Center which will allow greater insight into nozzle/afterbody flows relevant to the NASP. The SERN experiment was conducted in the NASA Ames 3.5 Ft. Hypersonic Wind Tunnel. This is a closed circuit, blowdown wind tunnel which has interchangeable, contoured, axisymmetric nozzles upstream of the test-section. Figures 1 and 2 illustrate the primary features of the SERN model. The side view of the model is a parallelogram. The leading- and trailing-edge angles of the model are 20°. The upper surface of the model forward of the cowl is a flat plate with a sharp leading-edge. A removable boundary-layer trip is located 4 in. downstream of the leading-edge. A perforated plate is located at the entrance of the supply pipe to the plenum, followed by two screens. The internal-nozzle downstream of the plenum, was designed to provide uniform flow at the simulated combustor exit station. A nozzle cowl, 4 in. length, begins at the combustor exit station. The internal-nozzle

---

*Research Scientist, AIAA Member
Mailing address: NASA Ames Research Center,
MS 230-2, Moffett Field, CA 94035
**Chief Scientist, AIAA Associate Fellow

exit referred to in this study corresponds to the cowl exit station.

Earlier versions of the model design included 15.2 cm. wide extensions that would attach to the side of the model and effectively increase the ramp width. The entire model is immersed in a freestream flow of $M_\infty = 7.3$ and high pressure air exits the nozzle with a jet to freestream static pressure ratio of approximately 11. Table 1 gives the flow conditions used for the present computations. A number of parametric studies were performed during the experimental investigation to understand the flow-field development under different operating conditions.

Figure 3 shows the basic flow features associated with the symmetry plane of the SERN experimental model, and the details are described below. The flow is three-dimensional, but most of the flow development can best be explained with a side view. Cross-flow views are given in a later section. The experimental model is oriented at a negative angle of attack with respect to the freestream. Leading-edge, or forebody, shocks are present both on the upper and lower surfaces of the model. Near the leading-edge, these shocks are limited to the upper and the lower surfaces. However, away from the leading-edge, the flow on the sides of the model is influenced by these forebody shocks. The internal-nozzle flow development is dictated by the contour of this nozzle which is designed to be shock free. The internal-nozzle shape is flat on the upper and side walls and only the lower wall is contoured. Due to the one-sided, contoured wall design, the flow at the exit of the nozzle will vary in the vertical direction but will be two-dimensional.

The interaction of the jet with the external flow is of main interest here. Similar to the plume flow associated with rocket nozzles[1,2] the interaction between the expanding plume and the external flow produces an outer plume shock, a shear-layer, and an inner plume shock (i.e., barrel shock). Since the ramp surface limits the plume flow development, the outer plume shock, the shear-layer and the inner plume shock will interact with the viscous wall layer on the ramp surface. The pressure differences between the upper and the lower surfaces of the model will induce a cross-flow from the lower to the upper side and a complex vortical structure will exist. The interaction between the plume flow and this side-edge flow will depend on the model geometry and flow conditions, such as angle of attack, etc. The static pressure ratio between the nozzle exit and the external flow primarily determines the size of the plume and the strength of the various flow structures associated with the plume. The pressure and skin friction on the ramp surface determine the nozzle efficiency and the thrust. The pressure and skin friction values on the ramp surface are a result of the various interactions. In addition to the flow details mentioned above, the boundary-layers and shear-layers are expected to be turbulent. The flow may separate on the upper cowl surface due to adverse streamwise pressure gradient and may also be a plume induced cross-flow separation which will be discussed in the results sections[3]. The major plume features will be present whether or not the flow separates on the cowl upper surface.

A variety of flow-field measurements have been taken both on the model surface and in the surrounding flow. At present, surface oil-flow patterns, shadowgraph visualization photographs and surface centerline static pressures are available and are presented in this paper. Complete surveys of the plume flow-field and skin friction data will be presented in a subsequent publication which also describes, in detail, the experimental program.

The experimental development has been supported by a computational effort. Earlier numerical studies were also used to help design this experiment. These efforts are described in greater detail by Ruffin et. al.[4] and by Venkatapathy et. al.[5] However, these preliminary computations were performed on an earlier model design with side extensions. In the present paper, 3-D Navier-Stokes solutions and 2-D symmetry plane solutions are presented for the baseline model at the nominal test conditions. Critical flow features are identified and the results are compared with experimental shadowgraphs, oil-flow visualization, and with surface pressure data along the model centerline. For the 3-D cases patched, and in some cases, solution adapted grids are used to map the complex 3-D geometry. Simulations of a version of the model with 15.2 cm. ramp side extensions are also presented. The effects of side extensions and other geometric features on SERN flow structure are discussed.

II. SOLUTION ALGORITHM

The computations in this study are performed with FL3D, a three-dimensional, implicit time marching Navier-Stokes solver. This code has previously been applied to axisymmetric and three-dimensional generic rocket nozzle plume flows.[1,2] All of the present calculations is for laminar flow of a perfect gas. The perfect gas assumption is valid because both the freestream and jet static temperatures are sufficiently low.

The numerical method is a LDU-ADI scheme with Roe's averaging and MUSCL differencing. This numerical formulation is detailed by Obayashi.[6] High order spatial accuracy is achieved by constructing MUSCL differencing with a differentiable limiter. The ADI sweeps of this formulation are quite efficient. The LDU-ADI algorithm is a diagonal algorithm requiring minimal CPU per iteration and is applicable to steady flows. Venkatapathy and Feiereisen[2] used this method to predict plume flows accurately.

This scheme has been applied to complex plume flows and the solutions were validated in terms of shock reflection location and plume structure for highly under-expanded axisymmetric plume flows. The calculations were performed both with supersonic external flow and with quiescent ambient conditions.[4] The success of the solver in these limited validations permits confidence in the present solutions for the experimental SERN flowfield.

Grid Generation

The computational grids used in this study are created with an algebraic grid generation code[7]. This code utilizes bi-linear interpolation to provide smoothly varying grid planes with nearly orthogonal grid cells. In order to map the complex SERN geometry, multiple grid zones are generated. The surface grid and the boundaries of each grid zone are shown in Figure 4 for the baseline model. This grid consists of 13 grid zones. Although not shown in Figure 4, each of the grid zones overlaps its neighbor by one common grid plane. The flow solver alternates grid zones on which it computes and applies the appropriate boundary condition on each of the intersecting grid planes. The computed results show seamless contours of all flow variables. The 3-D flow computation on the baseline model was performed with 338,000 total grid points and required approximately 5 hours of CPU time on a Cray YMP computer.

Boundary Conditions

The boundary conditions encountered in the present nozzle/afterbody calculations are inflow or outflow, wall boundaries, symmetry and reflection boundaries. All the boundary conditions were applied explicitly. At the supersonic inflow boundary, conservative flow variables were frozen, and at the outflow, flow variables were extrapolated from the interior. At the wall boundary viscous, no-slip, adiabatic wall boundary conditions were applied. In the case of symmetry boundaries, the flow variables were simply reflected from the interior. The various boundary conditions were unified into one generalized routine so that any specified part of the computational domain could be updated with the proper boundary condition. This unified boundary condition formulation greatly facilitated the use of 3-D zonal grids needed to map the experimental geometry.

III. 3-D RESULTS ON THE MODEL WITH SIDE EXTENSIONS

One of the afterbody design considerations for hypersonic vehicles is the width of the afterbody surface. This geometric factor influences total vehicle thrust due to nozzle plume pressure and skin friction drag on the afterbody. To study the effects of ramp width, calculations of a version of the model with 15.2 cm. side extensions were conducted. These calculations were performed at condition 1 shown on Table 1. For this case, the internal-nozzle flow was not computed. Instead, the jet flow at the nozzle exit is modeled by specifying inviscid conditions and approximate boundary-layer profiles. The boundary-layer profiles are specified by using the Pohlhausen polynomial approximation[8] for the velocities and the Crocco-Busemann relation[9] for compressible boundary-layers for the temperature profile. Figure 5 shows the computational model for this case. For this simulation a solution adapted grid was used. The 3-D adapted grid package used is described by Davies and Venkatapathy[10] and the resulting adapted grid in the plume region is shown in Figure 6. The grid-adaption package clusters existing grid points in regions of high flow gradients. For the present case, the grid was adapted on gradients of both Mach number and static temperature. Figure 7 gives computed Mach contours in the symmetry and outflow planes. The solution was adapted on gradients of both temperature and Mach number so that good resolution of the plume shocks and shear-layers are achieved.

The symmetry plane Mach contours in Figure 7 predict the outer plume shock, shear-layer and inner plume shock (i.e., barrel shock) shown in the schematic in Figure 3. This calculation is performed for the model at zero angle of attack. In the outflow plane at the end of the ramp, the Mach contours also show these features and indicate that the width of the plume extends laterally to near the side-edge of the model. The Mach contours in this outflow plane also indicate a complex viscous structure near the intersection of these plume shocks with the ramp and another complex structure just outside the plume boundary. These features can be further understood by studying Figures 8 and 9. Figure 8 shows simulated oil-flow and the Mach contours in the outflow plane, and Figure 9 shows particle traces and simulated surface oil-flow pattern. For the model with side extensions, the freestream flow expands in the region above the side extension ramp surface. The magenta particle traces in Figure 9 correspond to a large vortex which is generated in this expanding region above the side extensions. As the flow proceeds downstream, this side extension vortex lifts off the ramp surface, and follows the outside edge of the outer plume shock. The blue particle traces correspond to a vortex which begins from the trailing-edge corner of the cowl and follows the outer boundary of the plume along the surface of the ramp. The most prominent features in the predicted oil-flow pattern are cross-flow separation lines which extend from the cowl to the ramp trailing-edge. These separation lines are clearly within the plume external shock boundary and approach the symmetry line of the model as they proceed downstream. These features correspond to cross-flow separation induced by the inner plume shock (barrel shock) within the plume. The expanding cross-flow from the symmetry line experiences a strongly adverse pressure gradient from the internal plume shock and cross-flow separation is induced.

Based on the results presented, a schematic of the cross-sectional SERN flow is developed and is shown in Figure 18b. This flow schematic is appropriate in the plume region of the flow at the conditions given in Table 1. The large side extension vortex lifts off the ramp surface and interacts with the outer plume shock. Near the ramp, the inner plume shock induces a primary cross-flow separation vortex whose separation line is very prominent in the surface oil-flow pattern. Underneath this vortex, a secondary cross-flow vortex is found to exist.

IV. RESULTS ON THE BASELINE MODEL

Computations on the baseline SERN model without side extensions were conducted at condition 2 shown on Table 1. For this simulation the internal-nozzle flow was computed and solved coupled to the other grid regions. Predicted Mach contours in the symmetry and outflow planes for the baseline experimental model are shown in Figure 10. The symmetry plane shows the same features in the plume region as previous computations on the model with side extensions. The calculations on the baseline model and the experiment were performed with the model at a -1.1° angle relative to the freestream and the forebody produces a shock on the upper side of the model. From the outflow plane we see that the width of the plume extends to the side-edge of the body. Particle traces and velocity vectors which are not shown indicate a number of vortices near the model side-edge. The overall plume flow structure in the cross-flow plane for the baseline model is shown in Figure 18a for these flow conditions. The outer plume shock extends laterally over the side-edge of the model and approaches the side corner of the model near the ramp. This shock induces a vortex on the side of the model. As in the model with side extensions, the inner plume shock induces a primary cross-flow separation vortex, which is accompanied by a smaller secondary vortex. Because the baseline model has no side extensions, the large side extension vortex present in the previous results does not exist for the baseline model.

Surface pressure measurements have been taken at a variety of locations on the model ramp. At present only data along the centerline is available. Figure 11 shows a comparison of the experimental and computed static pressure along the ramp centerline. The computed results show excellent agreement with the experimental data.

The symmetry plane flow is of interest for two reasons. First, although experimental surveys of several cross-flow planes will be available, the most detailed data will be obtained along the symmetry plane. Also, very fine grids can be used in 2-D simulations to resolve critical flow features without prohibitive CPU requirements. For these two reasons, it is of interest to know if the three-dimensional features affect the symmetry plane flow. To study 3-D effects on the symmetry plane flow, 2-D symmetry plane results were compared to the predicted symmetry plane flow from a 3-D calculation. The symmetry plane grid contains 80 x 60 grid points. Figure 12 shows Mach number surveys at three streamwise locations for the 3-D and 2-D cases on the same grid. The x=24.8 in. station is upstream of the nozzle cowl. The x=41.9 in. station is in the plume region midway between the internal-nozzle exit and the end of the ramp, and the x=51.1 in station is in the plume region at the end of the afterbody ramp. It is found that the 3-D features do not significantly affect the symmetry plane flow until near the trailing-edge of the model. Similar comparisons of 2-D and 3-D results in the symmetry plane[4] also revealed little difference between the two simulations. However, overall the flow does expand somewhat faster in the 3-D case due to pressure relief in the cross-flow direction.

Calibration data obtained with the Mach 7.3 wind-tunnel nozzle used during the experimental investigation show the presence of a moderate degree of expansion (source flow) in the test-section. For most of the computational simulations, this gradient was neglected, and uniform external-flow conditions were imposed on the inflow boundaries of the computational domain. To evaluate the effect of the non-uniform external flow and to study any interaction between the non-uniform freestream and the jet plume, numerical experiments were conducted with uniform and expanding free-stream flow conditions. These numerical experiments were limited to 2-D, symmetry plane computations with a 159*119 grid. In the tunnel test-section, a normalized pressure change of $\Delta p/p_\infty = -0.138$ per meter and Mach number change of $\Delta M_\infty = 0.178$ per meter were measured. In the 2-D simulations, these gradients were imposed and through isentropic relationships[11] the freestream conditions and the conservative flow quantities at all the inflow and top boundary grid points were computed. In the uniform freestream case, the flow conditions corresponding to condition 2 in Table 1 was maintained at all grid points on the top and inflow boundary surfaces. Both cases were computed with the same nozzle sonic throat conditions for the internal-nozzle. Pressure contours from the computed solutions with uniform and non-uniform freestream conditions are shown in Figure 13 (a) and (b) respectively. Static pressure profiles, along the z-direction, at three streamwise locations, are compared in Figure 14 (a), (b) and (c). The computed solutions show that the non-uniform freestream conditions affect only the flow outside the jet-plume region. The upper forebody shock shape and the conditions behind the shock are affected by the conditions upstream of this shock, but the shock acts as a buffer to reduce the effect of the non-uniformities in the free-stream. The outer plume shock has a similar damping effect, and the flow-field in the vicinity of the jet closely resembles that of the uniform flow case. The ramp surface pressure and the flow inside the plume are unaffected by the non-uniform external flow. Though the numerical experiments were carried out only along the symmetry plane, as a 2-D study, these conclusions are also expected to hold in the 3-D case.

Symmetry plane Mach contours on a 2-D 300x300 fine grid are shown in Figure 15. This fine grid simulation resolves the outer plume shock, shear-layer, and inner plume shock quite well. It also indicates that the downward curve of the upper cowl surface induces a edge of the cowl. The curved outer boundary of the cowl followed by the shear-layer between the under-expanded jet and the freestream produces an effective compression corner.

An experimental shadowgraph photograph and a simulated shadowgraph based on the fine grid symmetry plane calculation are shown on Figure 16. Again we see the forebody shock, boundary-layer separation near the cowl trailing-edge, outer plume shock, shear-layer, and barrel-shock. The location of these features agrees very well with the computed results. One difference, however, is that the experimental boundary-layers and shear-layers are turbulent. The experimental shadowgraph shows a thick turbulent boundary-layer on the model forebody which feeds into a thick plume shear-layer. The laminar flow calculations of course do not reproduce these turbulent details but predict the overall symmetry plane flow quite well.

Predicted surface oil-flow patterns on the afterbody ramp for the baseline model and the model with side extensions are shown in Figures 17b and 17c. The experimental pattern is shown in Figure 17a. In the experimental oil pattern, the flow appears to be two-dimensional inside the cowl, with no separation at the corner. The pattern on the ramp is symmetrical and the centerline flow is straight down the ramp. The surface flow direction turns increasingly outboard with increasing distance from the centerline. The prominent cross-flow separation lines on the ramp predicted in both of the computed results are also observed experimentally. As is evident from the oil-flow patterns and indicated in schematics in Figures 18a and b, the primary cross-flow separation lines are found to exist closer to the symmetry line for the baseline model relative to the model with side extensions. The rate at which these separation lines approach the symmetry line toward the trailing-edge is different in the predicted vs the experimental results. The details of this viscous dominated effect may be strongly influenced by turbulence which is not modeled. In all of the oil-flow patterns a secondary cross-flow separation line is also seen near the side-edge of the model. In addition, the experimental oil-flow pattern shows a streamwise separation line on the upper surface of the cowl near the trailing-edge. This separation is also apparent from the computational and experimental shadowgraphs in Figure 16.

CONCLUDING REMARKS

The latest version of FL3D, an implicit, 3-D Navier-Stokes solver is used to predict the experimental hypersonic flow-field. Multiple, and in some cases, solution adapted grids are used to map the 3-D nozzle/afterbody geometry. TVD enhancements are used to model critical flow features. These modifications have greatly improved the efficiency of the code and its ability to provide accurate modeling of complex flow-fields. Three-dimensional calculations of the two SERN geometries and 2-D symmetry plane calculations have been performed which simulate the cold-jet perfect gas experimental conditions. Flow schematics appropriate for the conditions tested are presented for the baseline model and the model with side extensions.

The computed results show excellent agreement with experimental shadowgraph and with centerline surface pressure measurements. The computed and experimental surface oil-flows show favorable agreement but demonstrate the need for turbulence modeling. At present, several candidate algebraic and two equation turbulence models are being validated in jet plume flows. Turbulent code validation cases will be conducted and presented along with detailed calibrated experimental data in a subsequent publication. All of the flow features observed experimentally are also seen in the computed results, thus the success of the current predictions with the available data is quite promising.

Table 1.

	Condition-1	Condition-2
M_∞	7.3	7.4
α	0.0	-1.1
T_∞ (°K)	57.2	71.5
p_∞	756 Pa	673 Pa
Re/m	1.2×10^8	1.5×10^8
$p_{t_{jet}}/p_\infty$	300	337
$T_{t_{jet}}/T_\infty$	5.0	3.9
p_{jet}/p_∞	10.6	≈10.7
M_{jet}	2.83	≈2.87
Note: Both the freestream and jet gas are air.		

REFERENCES

[1]Venkatapathy, E., and Feiereisen, W.J., "3-D Plume Flow Calculations with an Upwind Solver," AIAA Paper 88-3158.

[2]Venkatapathy, E., and Feiereisen, W.J., Obayashi, S., "Computational Studies of Hard Body and 3-D Effects in Plume Flows," AIAA Paper 89-129.

[3]Venkatapathy, E, and Feiereisen, W. J., "Computational Analysis of Plume Induced Separation," AIAA Paper 91-0711.

[4]Ruffin, S.M., Venkatapathy, E., Keener, E.R., and Nagaraj, N., "Computational Design Aspects of a NASP Nozzle/Afterbody Experiment," AIAA Paper 89-0446.

[5] Venkatapathy, E., Ruffin, S.M., Lee, S.H., Deiwert, G.S., Feiereisen, W.J., "Development and Applications of a Nozzle/Afterbody Flow Solver," NASP CR 1068, Jan. 1990.

[6] Obayashi, S., "Numerical Simulation of Underexpanded Plumes using Upwind Algorithms," AIAA Paper 88-4360-cp.

[7] Venkatapathy, E, "Notes on Algebraic Grid Generation," unpublished.

[8] Pohlhausen, K., Z. Angew. Math. Mech., vol. 1, pp. 252-268, 1921.

[9] White, F.M., Viscous Fluid Flow, McGraw-Hill, New York, p. 587, 1974.

[10] Davies, C.B., Venkatapathy, E., "Application of a Solution Adaptive Grid Scheme, SAGE, to Complex Three-Dimensional Flows," AIAA Paper 91-1594.

[11] Ames Research Staff, "Equations, Tables, and charts for Compressible Flow," NACA Report 1135, 1953.

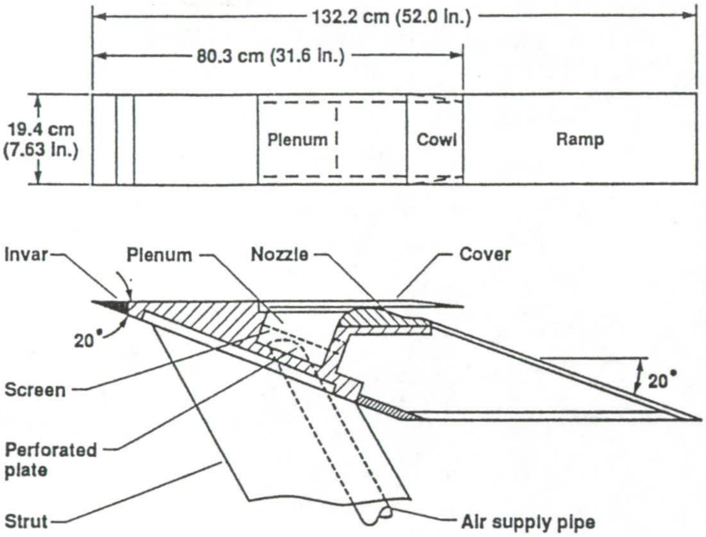

Figure 1. Schematic of the baseline SERN Model

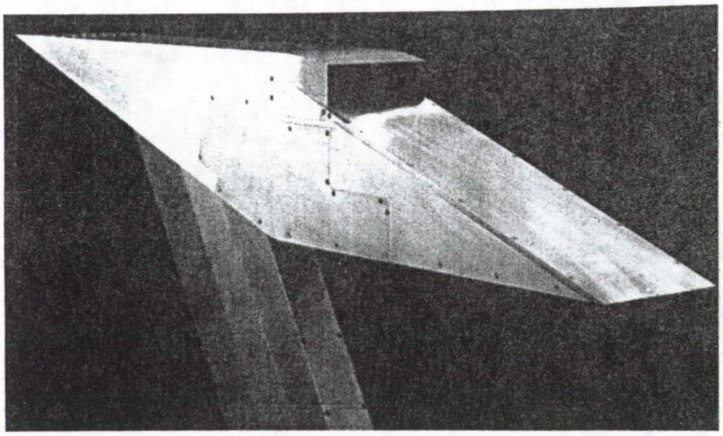

Figure 2. Photograph of the baseline SERN Model

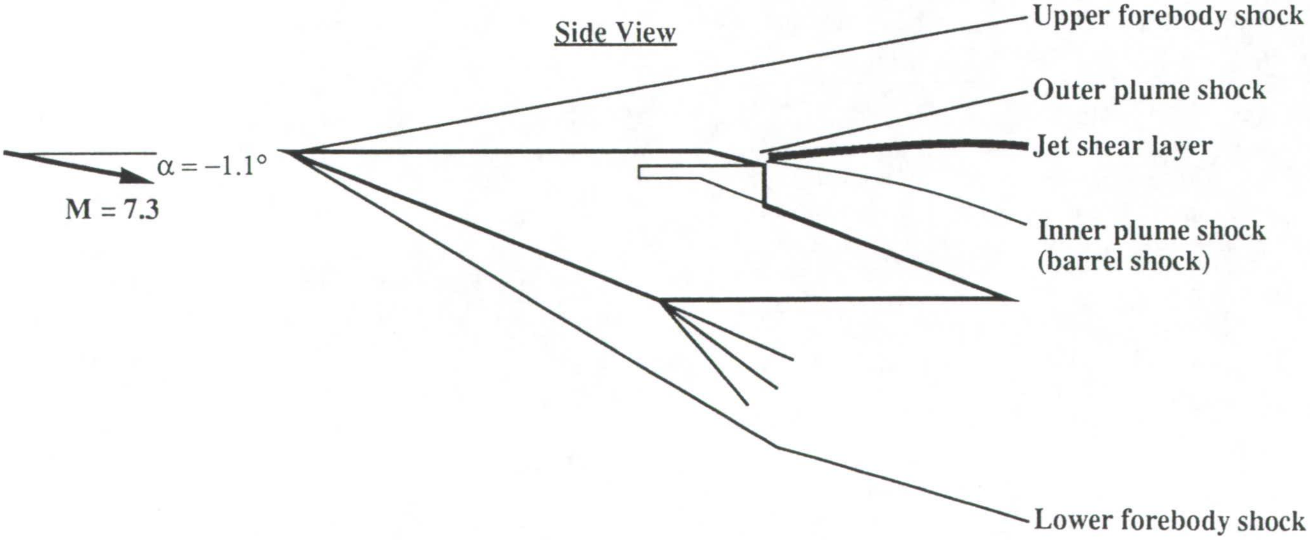

Figure 3. Symmetry plane schematic of the SERN flow-field.

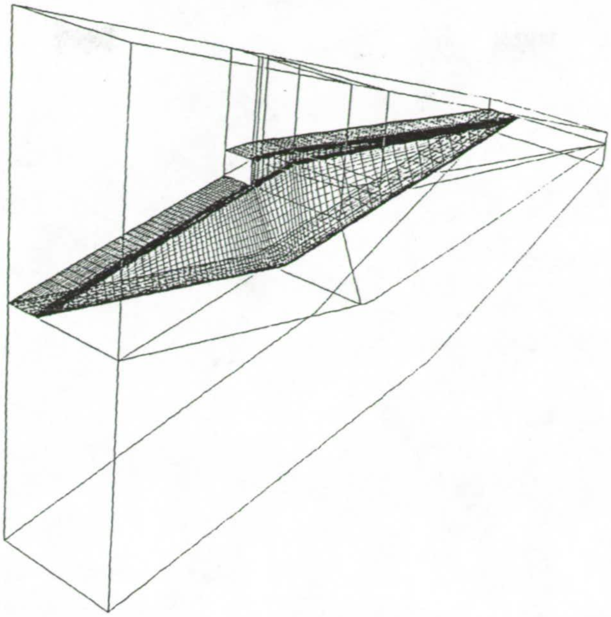

Figure 4. Surface grid and grid zone boundaries for baseline model computations.

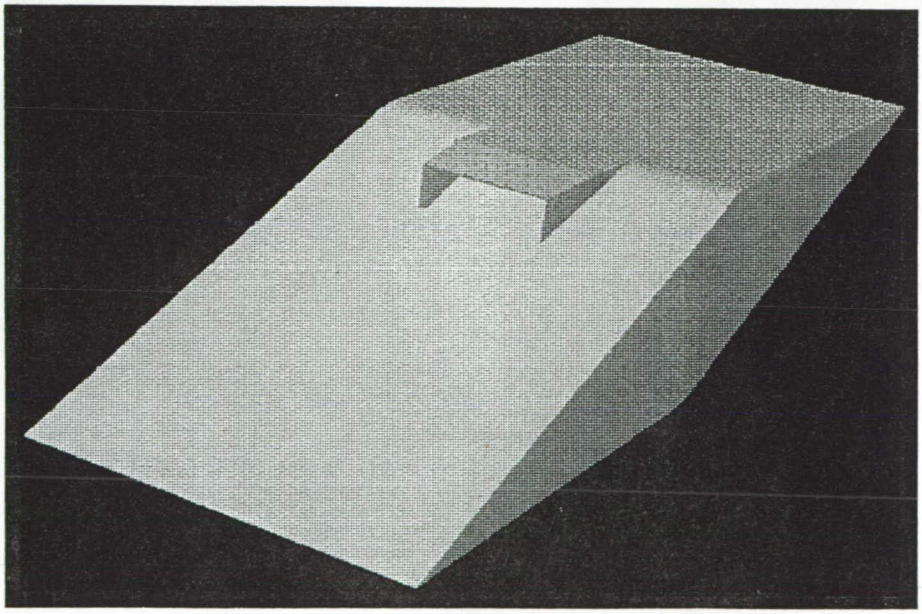

Figure 5. Computational body for model with 15.2 cm. wide side extensions.

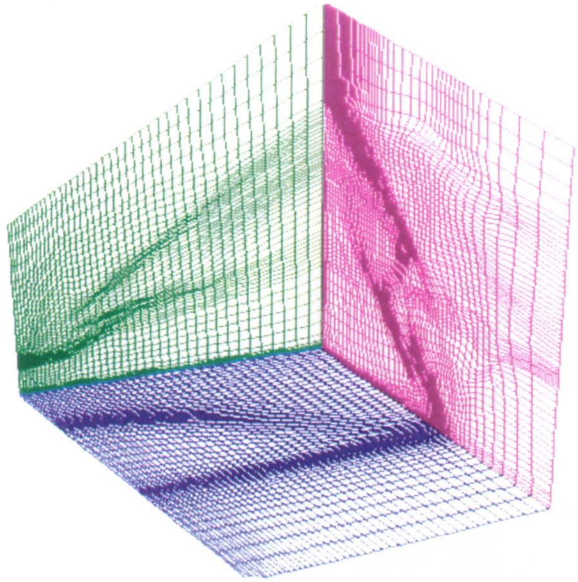

Figure 6. Solution adapted grid for computations on model with side extensions.

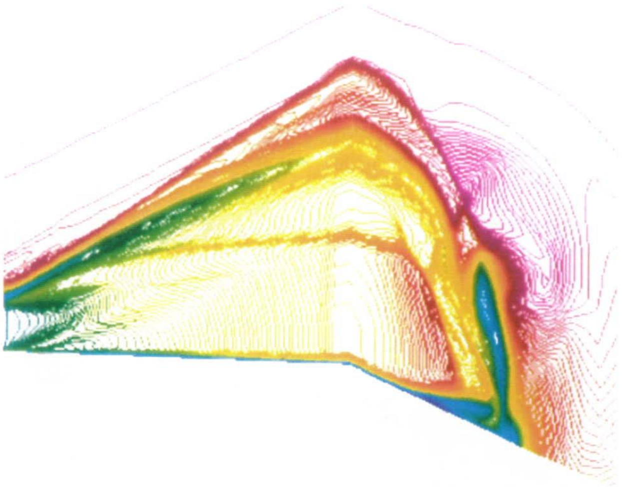

Figure 7. Computed Mach contours in the symmetry and outflow planes in the plume region of the model with side extensions. Solution adapted grid is used.

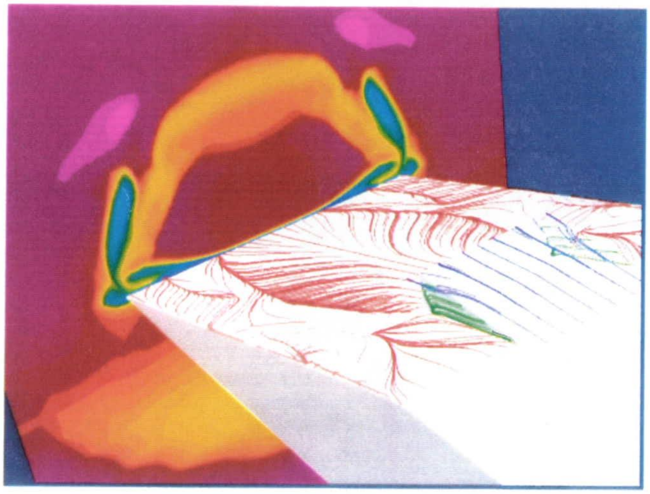

Figure 8. Simulated surface oil flow pattern and Mach contours in the outflow plane for model with side extensions.

Figure 9. Simulated surface oil flow pattern and particle traces for the model with side extensions.

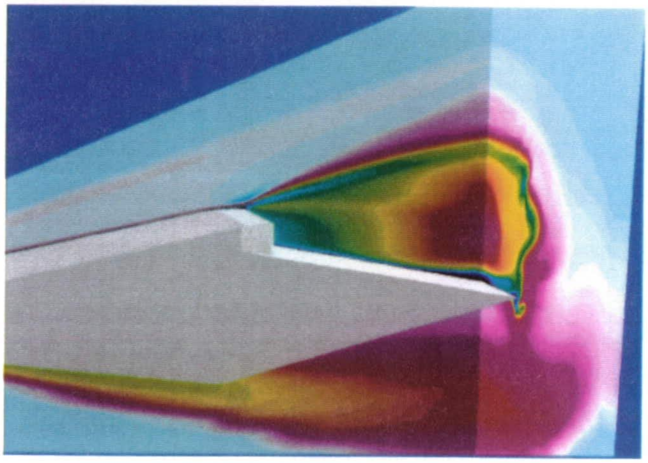

Figure 10. Computed Mach contours in the symmetry and outflow planes for baseline model.

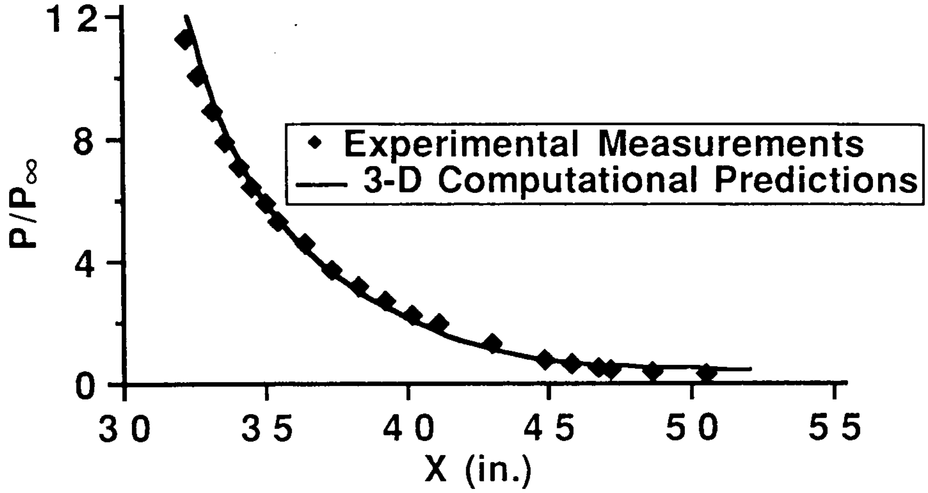

Figure 11. Comparison of computed and experimental surface static pressure along the baseline model centerline.

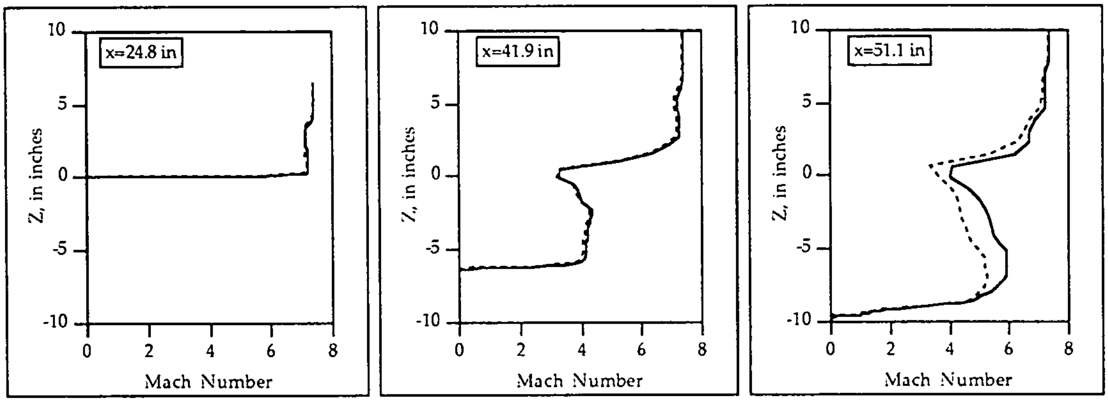

Figure 12. Comparison of symmetry plane Mach number at three streamwise stations for 3-D and 2-D calculations. Solid line = 3-D solution, Dashed line = 2-D solution on the same symmetry plane grid.

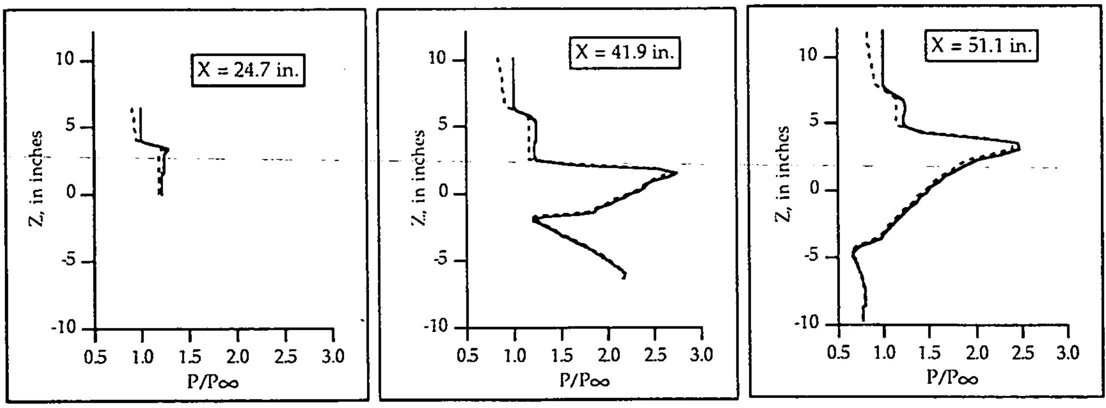

Figure 13. Comparison of symmetry plane pressure at three streamwise stations for flow with uniform freestream and flow with expanding freestream variation. Solid line = uniform freestream, Dashed line = expanding freestream.

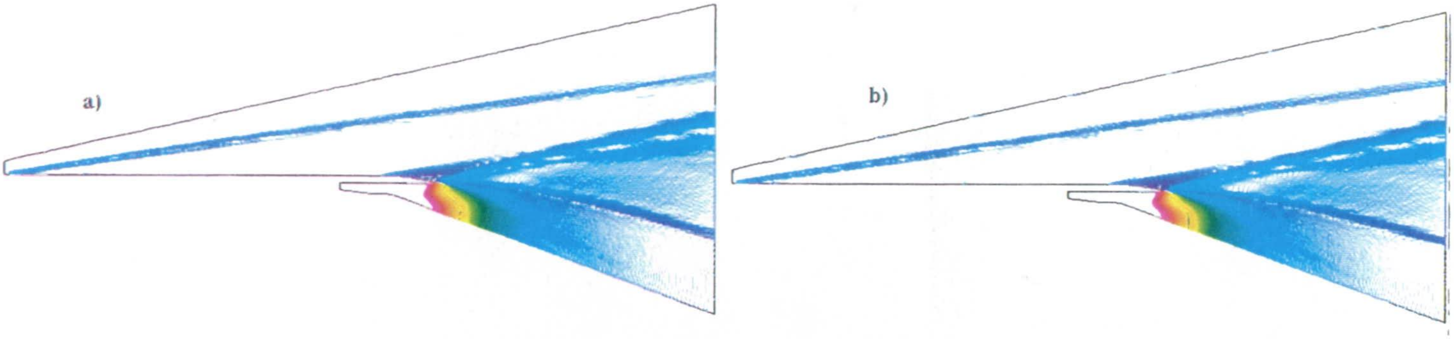

Figure 14. Comparison of symmetry plane pressure contours for a) flow with uniform freestream and b) with expanding freestream variations.

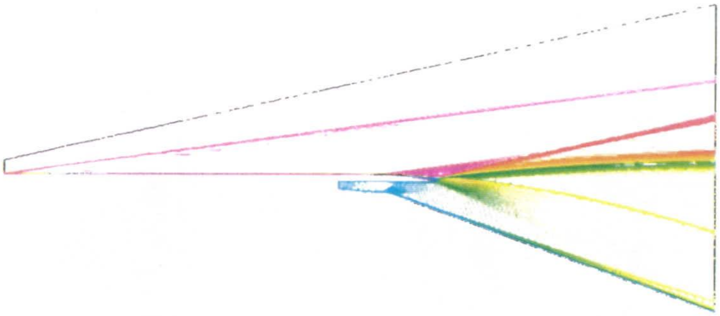

Figure 15. Computed Mach contours in the symmetry plane of the base line model using a 2-D fine grid.

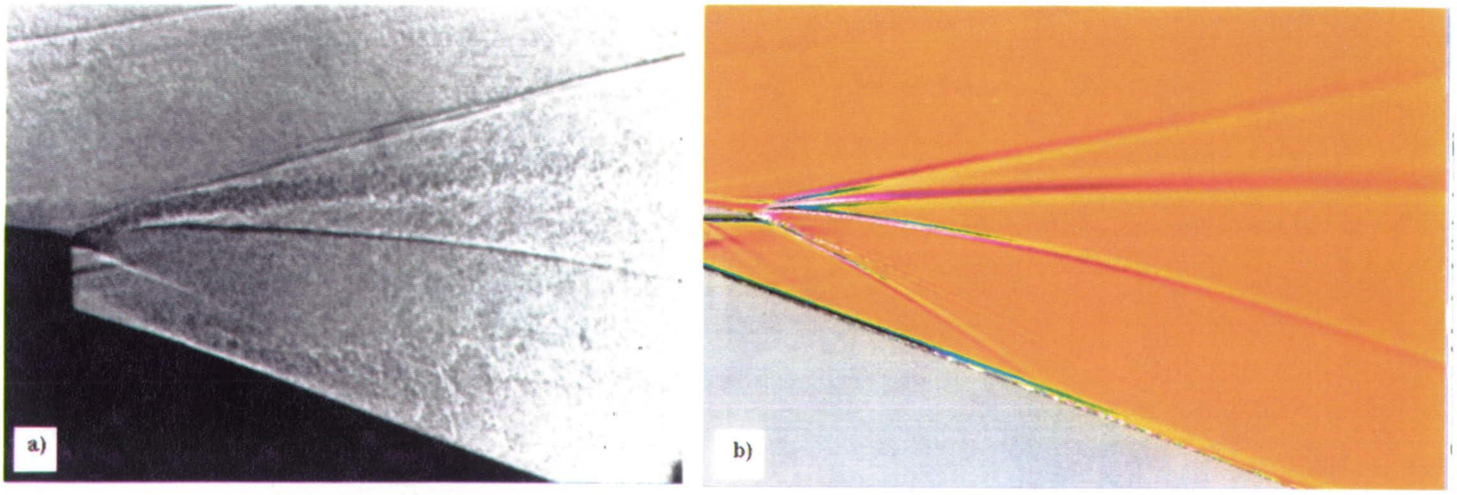

Figure 16. a) Experimental and b) computational shadowgraphs in the symmetry plane of the baseline model. Simulated shadowgraph is based on 2-D fine grid results.

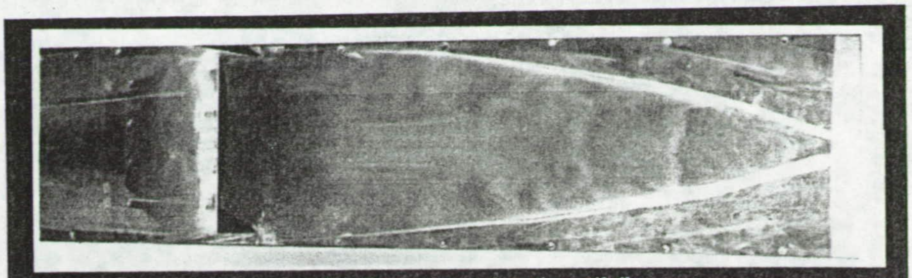

17a) Experimental surface oil-flow

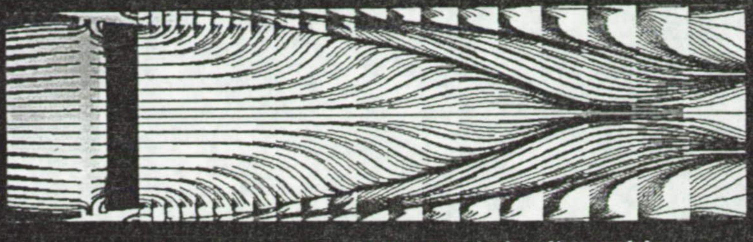

17b) Simulated surface oil-flow for the baseline model

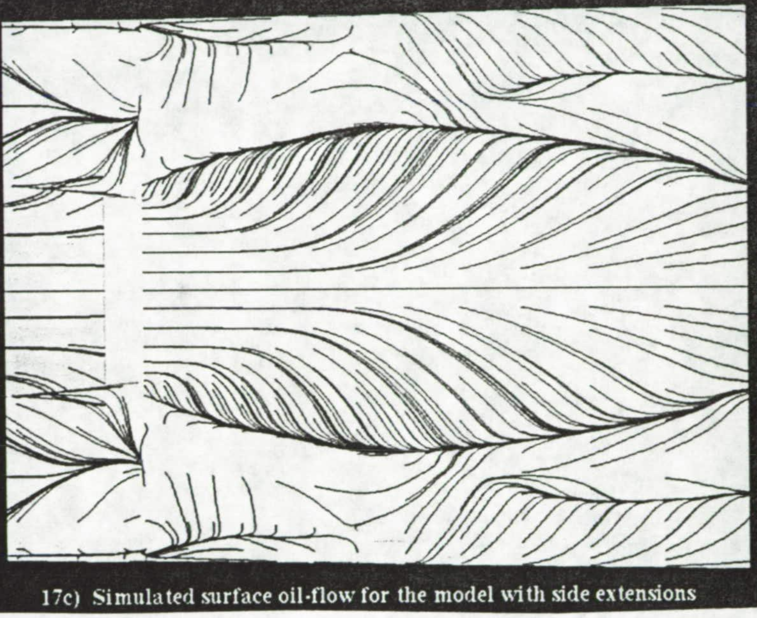

17c) Simulated surface oil-flow for the model with side extensions

Figure 17. Experimental and simulated oil-flow on the ramp surface.

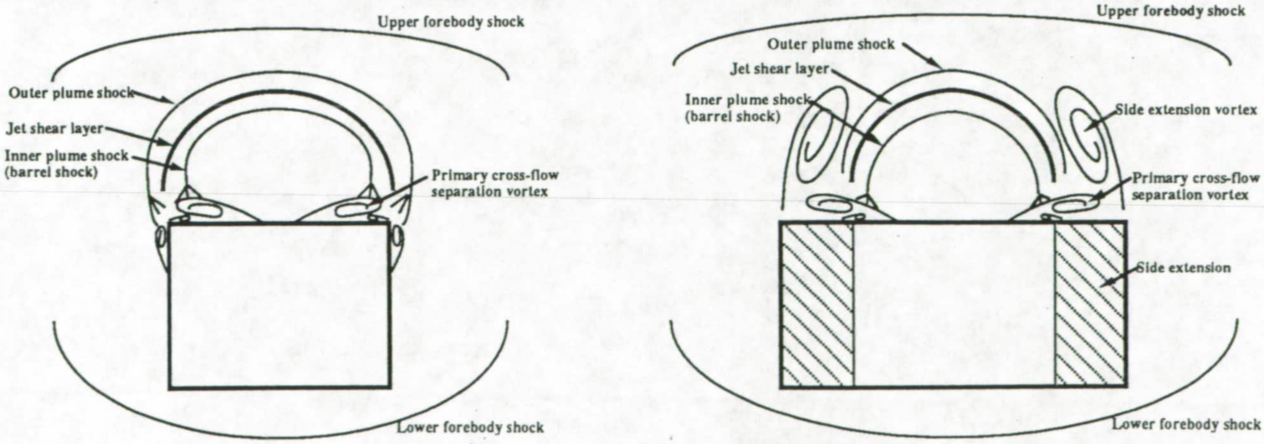

a) baseline model

b) model with side extensions.

Figure 18. Cross-sectional schematics of SERN flow field in the plume region.

AIAA-92-0545
Effective Treatments of the Singular Line Boundary Problem for Three Dimensional Grids

Grant Palmer
NASA Ames Research Center
Moffett Field, CA

Ethiraj Venkatapathy
Eloret Institute
Palo Alto, CA

30th Aerospace Sciences Meeting & Exhibit
January 6-9, 1992 / Reno, NV

Effective Treatments of the Singular Line Boundary Problem For Three Dimensional Grids

Grant Palmer*
Aerothermodynamics Branch
NASA Ames Research Center
Moffett Field, Ca.
and
Ethiraj Venkatapathy*
Eloret Institute, 3788 Fabian Way
Palo Alto, CA 94303

Abstract

The axis singularity problem for three dimensional blunt body flows is addressed in this paper. Two methods of eliminating the axis-singularity difficulty are outlined for use with finite-difference codes. In the first method, the three-dimensional Navier-Stokes equations are reformulated using a redefined grid Jacobian that is non-zero at the singular line. The resulting equations along with appropriate boundary procedure at the axis are solved using the finite-difference form of a flux-split, upwind scheme. In the second method, the three-dimensional Navier-Stokes equations are solved using the Roe flux-difference splitting method with a finite-volume based method for evaluation of the metrics and grid Jacobian, and appropriate boundary conditions. Solution symmetry is preserved independent of the orientation and location of the singular line boundary with respect to the free-stream velocity vector. Inviscid solutions are compared to the results of Lyubimov and Rusanov[1] who employed a shock-fitting technique. Viscous and real-gas computations are also presented demonstrating the generality of the two techniques.

Introduction

Most three dimensional (3-D) grids constructed to solve for flow over a blunt body consist of series of grid planes distributed radially about a common or singular line. Generally, this singular line extends from the nose of the body. It is referred to as a singular line because it introduces a mathematical singularity into the solution algorithm, which can cause non-physical perturbations in the flow solution. Dealing with the singular line is one of the most vexing problems in the computation of 3-D blunt body flows. A number of recent references[2-6] have reported the occurrence of non-physical solutions in the vicinity of the singular line.

Generally some form of extrapolation is used to determine the Jacobian, metric terms, and flow quantities along the singular line. The most commonly used methods include a simple zeroth-or first-order extrapolation-averaging boundary condition. These methods can cause numerical problems in the flow solution. Irregularities are created in the pressure and velocity field.This is readily apparent if a

---

* Research scientist, member AIAA. Mailing address: Mail Stop 230-2, Moffett Field, Ca 94035.

grid where the singular line coincides with the stagnation line of the flow is used. A zeroth-order extrapolation causes the peak pressure to occur away from the stagnation point, and the radial velocity along the stagnation line will not be zero. Similar behavior has been observed both by Peery and Imlay[2], and Josyula and Shang[4].

This study attacks the singular line boundary condition problem with two different approaches. The first is a reformulation of the governing equations based on a cylindrical-type grid Jacobian that is non-zero on the singular line. This allows the flux emanating from the singular line to be properly computed. This method in essence moves the singularity to two source-like vectors that are not evaluated along the singular line. In the second approach the governing equations in generalized coordinate system, obtained from the the Cartesian system, are solved using Roe's approximate Riemann solver[7] along with MUSCL extrapolation scheme. A finite-volume based formulation is utilized in evaluating the grid Jacobian and the metric terms. With second order accurate boundary procedures, the singular line problem is eliminated in this approach.

Because the singular line problem is due to fluid dynamics and the evaluation of metric and flux terms, the derivation of the techniques and most of the solutions shown in this work are for perfect gas flow. The two approaches are tested by computing a Mach 20 inviscid flow over a sphere for comparison with accurate solutions reported in Ref.1. To evaluate the applicability of the solution techniques for a wide range of problems, a grid refinement study along with numerous computations for viscous, adiabatic and isothermal walls, three-dimensional ideal gas conditions and three- dimensional reacting-gas conditions were conducted.

Method One: Reformulation of the Governing Equations

A typical grid over a three dimensional blunt body is shown in Fig. 1. It consists of a series of radial grid planes that meet along a common or singular line usually emanating from the nose of the body. Cell volumes adjacent to the singular line are wedge-shaped instead of cube-shaped. In the following discussions the singular line is assumed to lie on the x-axis.

The solution procedure normally employed by CFD algorithms is to transform the governing equations and grid coordinates from a Cartesian (x, y, z) coordinate system to a generalized (ξ, η, ζ) coordinate system. In this and subseqent discussions in this section ξ-lines march along the longitudinal-, η-lines the circumferential-, and ζ-lines the body normal-direction. The Navier-Stokes equations expressed in vector form in generalized coordinates are

$$\frac{\partial \widehat{Q}}{\partial t} + \frac{\partial \widehat{E}}{\partial \xi} + \frac{\partial \widehat{F}}{\partial \eta} + \frac{\partial \widehat{G}}{\partial \zeta} = \frac{\partial \widehat{R}}{\partial \xi} + \frac{\partial \widehat{S}}{\partial \eta} + \frac{\partial \widehat{T}}{\partial \zeta} \quad (1)$$

with

$$\begin{aligned} \widehat{Q} &= J^{-1}Q \quad (2)\\ \widehat{E} &= J^{-1}\left[\xi_x E + \xi_y F + \xi_z G\right]\\ \widehat{F} &= J^{-1}\left[\eta_x E + \eta_y F + \eta_z G\right]\\ \widehat{G} &= J^{-1}\left[\zeta_x E + \zeta_y F + \zeta_z G\right] \end{aligned}$$

where E, F, and G are the inviscid Cartesian flux vectors. The grid Jacobian, J, used in the above expressions and to compute the metric terms, $\xi_x, \xi_y, \xi_z, \eta_x$,etc., is defined as

$$\begin{aligned} J^{-1} = [&x_\xi(y_\eta z_\zeta - y_\zeta z_\eta) - x_\eta(y_\xi z_\zeta - y_\zeta z_\xi)\\ &+x_\zeta(y_\xi z_\eta - y_\eta z_\xi)] \quad (3) \end{aligned}$$

Most modern CFD algorithms use upwind differencing, splitting the inviscid flux vectors into positive and negative components according to the direction of signal propagation. The term $\frac{\partial \widehat{E}}{\partial \xi}$,for instance, is split into $\frac{\partial \widehat{E}^+}{\partial \xi}$ and $\frac{\partial \widehat{E}^-}{\partial \xi}$ components. In the finite-difference formulation, the evaluation of $\frac{\partial \widehat{E}}{\partial \xi}$ at the grid points adjacent to the singular line involves evaluating the $\widehat{E}^+$ flux at the singular line.

Along the singular line, the spatial derivatives in the circumferential direction, x_η, y_η, and z_η, are all zero making the grid Jacobian defined by eq. (3)

zero. This causes the $\widehat{E}^{+}$ flux to be incorrectly set to zero along the singular line. Essentially, no information is allowed to pass from the singular line boundary to the interior causing spurious perturbations in the computed flow solution.

A finite value for the singular line Jacobian can be obtained by extrapolation from interior grid points or by setting y_η and z_η, or x_η and y_η depending on the axis orientation, to small finite values. As will be shown these approximate methods yield unsatisfactory results and lead to nonphysical flowfield perturbations in the region of the singular line.

The first method for treating the singular line boundary problem presented in this study involves re-defining the grid Jacobian such that it is no longer zero on the singular line. The grid Jacobian is written as the product of two quantities

$$J^{-1} = r\bar{J}^{-1} \qquad (4)$$

where r is the radial distance from the singular line, $(y^2 + z^2)^{\frac{1}{2}}$. The modified Jacobian, $\bar{J}^{-1}$, is non-zero throughout the entire computational domain. It is equivalent to the grid Jacobian obtained if the Navier-Stokes equations were originally expressed in cylindrical, (x, r, θ), coordinates and can be computed from the expression

$$\begin{aligned}\bar{J}^{-1} = [&x_\xi(r_\eta\theta_\zeta - r_\zeta\theta_\eta) - x_\eta(r_\xi\theta_\zeta - r_\zeta\theta_\xi)\\ &+x_\zeta(r_\xi\theta_\eta - r_\eta\theta_\xi)] \qquad (5)\end{aligned}$$

If Eq. (4) is inserted in Eq. (1) and the chain rule used to remove the r-term from the partial differential equations, the resulting equation is:

$$\frac{\partial\bar{Q}}{\partial t}+\frac{\partial\bar{E}}{\partial\xi}+\frac{\partial\bar{F}}{\partial\eta}+\frac{\partial\bar{G}}{\partial\zeta}+\frac{\bar{H}}{r} = \frac{\partial\bar{R}}{\partial\xi}+\frac{\partial\bar{S}}{\partial\eta}+\frac{\partial\bar{T}}{\partial\zeta}+\frac{\bar{W}}{r} \quad (6)$$

The vector quantities are now scaled by the modified, or cylindrical, grid Jacobian.

$$\bar{Q} = \bar{J}^{-1}Q$$

$$\bar{E} = \bar{J}^{-1}\Big[\xi_x E + \xi_y F + \xi_z G\Big]$$

$$\bar{F} = \bar{J}^{-1}\Big[\eta_x E + \eta_r y F + \eta_z G\Big]$$

$$\bar{G} = \bar{J}^{-1}\Big[\zeta_x E + \zeta_y F + \zeta_z G\Big]$$

The viscous vectors are similarly scaled. The metric quantities, $\xi_x, \xi_y, \xi_z, \eta_x, etc$, and Cartesian flux vectors are unchanged. Equation (6) is identical to that obtained if the cylindrical Navier-Stokes equations are transformed to generalized coordinates. The additional source-like vectors, $\bar{H}$ and $\bar{W}$, are defined as

$$\begin{aligned}\bar{H} &= [r_\xi\bar{E} + r_\eta\bar{F} + r_\zeta\bar{G}] \qquad (7)\\ \bar{W} &= [r_\xi\bar{R} + r_\eta\bar{S} + r_\zeta\bar{T}]\end{aligned}$$

The singularity has, in effect, been transfered to these two source-like vectors. Since the source vectors are not evaluated along the singular line where $r = 0$, the source vectors are never singular. For grids over bodies of rotation where $x_\eta = r_\eta = 0$, the source vector, $\bar{H}$, is given by

$$\bar{H} = \bar{J}^{-1}\begin{bmatrix}\rho v_r\\ \rho u v_r\\ \rho v v_r + p\ cos\theta\\ \rho w v_r + p\ sin\theta\\ (e+p)v_r\end{bmatrix} \qquad (8)$$

$$v_r = v\ cos\theta + w\ sin\theta$$

$$\theta = tan^{-1}\left(\frac{z}{y}\right)$$

For purposes of comparison, the same zeroth-order extrapolation/averaging boundary condition along the singular line was used with both the formulation using the customary Cartesian grid Jacobian and the new formulation using the cylindrical-type grid Jacobian. For zero angle of attack, the velocity components v and w are set to zero along the singular line which is also the stagnation line for these cases. For non-zero angle of attack cases, the Cartesian v velocity component is still zero due to symmetry. The w component is obtained by extrapolation/averaging.

Method Two: Three-Dimensional Roe Upwind Solver

In the second method, both the Navier-Stokes equations and the Euler equations are solved using the upwind flux-difference splitting scheme due to

Roe[7]. The equations in generalized coordinates are obtained from the Navier-Stokes or Euler equations written in the Cartesian coordinate system. The transformation from the physical (Cartesian coordinate) to the computational (generalized) coordinate system is performed numerically. The transformed equations in the computational coordinate are then solved using Roe's approximate Riemann solver. The singular line problem is easier to study with an explicit formulation rather than an implicit formulation. Thus, only an explicit upwind formulation is studied and reported in this paper.

In the finite-difference representation, appropriate flux evaluation in the neighborhood of the singular line becomes an issue since the transformation from the physical to the computational coordinate is singular at the singular line. Instead if a finite-volume representation is followed, then the metric and Jacobian are determinate and the singular line difficulty can be avoided. In the present method, following Vinoukur[9] and Obayashi[10], we combine the finite-difference method of solving the governing equations with the finite-volume method of evaluating the grid metrics and the Jacobian. For all the flows solved using the present method, a finite- difference grid was selected such that grid points were located along the singular line (see Figure 1).

The finite-difference representation of equation (1), with the upwind-biased flux-difference splitting of inviscid terms due to Roe[7] and with central-difference representation of the viscous terms is written as :

$$[\widehat{Q}^{n+1} - \widehat{Q}^{n}]_{(i,j,k)} =$$

$$-\Delta t[(\widehat{E}_{(i+\frac{1}{2},j,k)} - \widehat{E}_{(i-\frac{1}{2},j,k)}) + (\widehat{F}_{(i,j+\frac{1}{2},k)} - \widehat{F}_{(i,j-\frac{1}{2},k)})$$
$$+(\widehat{G}_{(i,j+\frac{1}{2},k)} - \widehat{G}_{(i,j-\frac{1}{2},k)}) - (\widehat{R}_{(i,j+\frac{1}{2},k)} - \widehat{R}_{(i,j-\frac{1}{2},k)})$$
$$-(\widehat{S}_{(i,j,k+\frac{1}{2})} - \widehat{S}_{(i,j,k-\frac{1}{2})}) - (\widehat{T}_{(i,j,k+\frac{1}{2})} - \widehat{T}_{(i,j,k-\frac{1}{2})})] \quad (9)$$

In the above equation, the change in $\widehat{Q}$ at the grid point (i,j,k) between two time levels is represented as the the difference in the fluxes (inviscid and viscous) around the surfaces elements of the control volume placed at the grid point (i,j,k). These fluxes are evaluated at the cell interfaces placed half-way between the grid points in each computational direction. The inviscid fluxes are upwind differenced and are evaluated using Roe's flux-difference splitting method. For example, the inviscid flux in the ξ-direction at $(i+1/2,j,k)$ interface, utilizing Roe's approximate Riemann solver, is given by

$$\widehat{E}_{(i+1/2,j,k)} = 1/2[\widehat{E}(Q_R, \vec{\mathrm{S}}^{\xi}_{i+1/2,j,k})+$$
$$\widehat{E}(Q_L, \vec{\mathrm{S}}^{\xi}_{i+1/2,j,k}) - |\mathbf{A}(Q_L, Q_R, \vec{\mathrm{S}}^{\xi}_{i+1/2,j,k})|(Q_R - Q_L)] \quad (10)$$

where $|\mathbf{A}|$ is the Roe-averaged Jacobian of $\widehat{E}$ and Q_L and Q_R are the state variables to the left and right of the interface at $(i+1/2,j,k)$ and $\vec{\mathrm{S}}^{\xi}_{i+1/2,j,k}$ is the surface area vector of the interface. The surface area vectors are related to the metric terms. For example $\vec{\mathrm{S}}^{\xi}_{i,j,k} = J^{-1}\left[\xi_x\vec{i} + \xi_y\vec{j} + \xi_z\vec{k}\right]$. Roe-averaged flux-difference representations, similar to equation (10) are used for inviscid fluxes in η and ζ direction. The viscous fluxes are central differenced and each viscous flux at the half- cell interfaces involves the state vector Q and the metric terms from the neighbouring grid points. For example, the viscous flux in the ξ direction at the cell interface $(i+1/2,j,k)$ will be of the form

$$\widehat{R}_{i+1/2,j,k} = \widehat{R}(Q_{i,j,k}, Q_{i,j+1,k}, Q_{i,j-1,k},$$
$$Q_{i,j,k+1}, Q_{i,j,k-1}, Q_{i+1,j+1,k}, Q_{i+1,j-1,k},$$
$$Q_{i+1,j,k+1}, Q_{i+1,j,k-1}, \vec{\mathrm{S}}^{\xi}_{i+1/2,j,k}, \vec{\mathrm{S}}^{\eta}_{i+1/2,j,k},$$
$$\vec{\mathrm{S}}^{\zeta}_{i+1/2,j,k}) \quad (11)$$

The above difference scheme can be spatially first, second or third order accurate depending on the approximation used for Q_L and Q_R. Through MUSCL extrapolation[7] for Q_L and Q_R in equation (10), second and third order spatial accuracy can be achieved. When applying MUSCL extrpolation, the primitive variables are limited so as to be Total Variation Diminishing (TVD) and in the present study, a differential limiter[7] is used. In addition, in evaluating the flux Jacobian matrix, $|\mathbf{A}|$, entropy correction is required when the magnitude of the eigenvalues become small. The entropy correction used here is similar to the one suggested by Yee[11] and used by Obayashi[10] but with the coefficient term proportional to the second derivative of the pressure. The entropy corrected eigenvalue $\widehat{\lambda}$ of the left and right states are

$$\widehat{\lambda} = (\lambda^2 + \epsilon^2)/2\epsilon \quad if \quad |\lambda| < \epsilon \tag{12}$$

where

$$\epsilon = c_1(|\delta^2 p|/|p_{average}|)(|\lambda_{max}|). \tag{13}$$

In equation 13, p is the pressure and $0.2 < c_1 < 1.0$.

The evaluation of inviscid and viscous fluxes involve not only the state vectors, Q, but also the surface area vectors (the metric terms) and the Jacobian. The metric terms, represented by the area vectors $\vec{S}^\xi$, $\vec{S}^\eta$ and $\vec{S}^\zeta$ and the Jacobian of the transformation (which is related to the volume by $J^{-1} = V$, where V is the volume) are all evaluated by constructing a finite-volume around each grid point (i,j,k). For the grids used in the present study, the volumes are made up of 6-sided elements away from the singular line and 5-sided elements near the singular line. At all interior points, where the volume is 6-sided , the surface area vectors and volume can be evaluated[9] as :

$$\vec{S}^\xi_{i,j,k} = \frac{1}{8}(\vec{r}_{(i,j+1,k+1)} - \vec{r}_{(i,j-1,k-1)})\times (\vec{r}_{(i,j-1,k+1)} - \vec{r}_{(i,j+1,k-1)}) \tag{14}$$

where $\vec{r}$ is the position vector, and

$$V = \frac{1}{12}(\vec{S}^\xi_{i+1,j,k} + \vec{S}^\xi_{i-1,j,k} + \vec{S}^\eta_{i,j+1,k} + \vec{S}^\eta_{i,j-1,k} + \vec{S}^\zeta_{i,j,k+1} + \vec{S}^\zeta_{i,j,k-1})\bullet(\vec{r}_{(i+1,j+1,k+1)} - \vec{r}_{(i-1,j-1,k-1)}) \tag{15}$$

The surface area vectors required in expressions similar to equations (10,11) are at the cell interfaces and are computed by averaging the area vectors at the grid points.

$$S^\xi_{i+1/2,j,k} = \frac{1}{2}(S^\xi_{i+1,j,k} + S^\xi_{i,j,k}) \tag{16}$$

The flux-difference terms in the right hand side of equation 9 can be evaluated accurately without any difficulty at all interior points. Since the solution at the singular line boundary is not solved for but computed by applying appropriate boundary conditions, evaluation of the metric terms and the Jacobian at the singular line are not required. But the solution at grid points adjacent to the singular line requires the surface area vectors half-way between these points and the singular line. The required surface area vectors and the volume elements, for all the grid points adjacent to the singular line, are evaluated by constructing appropriate surface and volume elements around these grid points instead of using equations 14, 15 and 16. These evaluations are very simple and are not shown. Once the appropriate area vectors and the Jacobian are evaluated at all the interior points, the state vector can be updated from one time level to the next.

Using equation (9) the solution vector at all the interior points are explicitly updated. To compute axisymmetric flows, only three computational planes along the η or circumferential direction are used and the solution is sought only on the mid-plane (see Figure 9). The state vector on the adjacent planes are obtained through rotation. Three planes along the η direction are required to impose axisymmtery. At the boundaries, such as wall, inflow, outflow or symmetry , appropriate boundary condition procedures are employed to extrapolate the state vector Q to the boundary surfaces. Second order accurate extrapolation , involving Q(2,j,k), Q(3,j,k) and Q(4,j,k) grid points result in Q(1,j,k) at the grid points on the singular line boundary.

For three-dimensional flows, a complete three-dimensional grid is used. If the flow is bi-symmteric then the grid is constructed in only one-half of the three-dimensional volume. The boundary conditions for the wall, inflow or outflow boundaries are similar to the axisymmteric (3-plane) boundary conditions. But for the grid points on the singular line, in addition to the second-order accurate extrapolation, an averaging procedure (in the η direction) at the singular line for $(p, \rho, |U|)$ is applied and the velocity $|U|$ is rotated to coincide with the velocity direction of the state vector at the adjacent grid point, (2,j,k). The accuracy of the present method is demonstrated through numerical examples in the next section.

Results

Solutions computed using both methods are compared against data produced by Lyubimov and

Rusanov[1]. They utilized a shock-fitting iterative difference scheme, referred to as a constant direction scheme, to compute inviscid flow over simple bodies of revolution at various Mach numbers. The method used the non-conservative form of the governing equations to solve for the vector of primitive variables $X = [\rho, u, v, w, p]$ as well as the function F which defined the shape and location of the shock subject to the initial and boundary conditions. The results given in Ref. 1 are particularly useful for this study because they are presented as a series of tables showing shock standoff distance and numerical values of normalized density, pressure, and velocity between the body and shock at various angles along the body surface. This allows a one-to-one comparison between an independent calculation and the results computed in this study.

The general test case selected was that of Mach 20, inviscid perfect gas flow over a sphere at various angles of attack. This case was chosen to permit comparison with Ref. 1. The techniques presented are equally effective for viscous and real gas flows as will be demonstrated.

Results Using the Cylindrical Formulation

The first series of line plots concerns solutions for zero angle of attack, effectively axisymmetric flow over a sphere. Results are shown for both the 3-D Cartesian grid Jacobian and 3-D cylindrical grid Jacobian versions of the codes. Henceforth, the Cartesian grid Jacobian and cylindrical grid Jacobian solutions will be referred to as the Cartesian and cylindrical solution respectively. Both codes utilize shock-capturing with first-order accurate differencing used for the inviscid fluxes. Both codes used the same grid and the same zeroth-order boundary condition along the singular line. To give the grid Jacobian some non-zero but infinitesimally small value for the Cartesian grid Jacobian case the points on the singular line were given finite values of y and z corresponding to the points being distributed on a circle of radius 1.0×10^{-7} normalized with respect to the sphere radius centered on the x-axis . The metric terms are identical for both cases. Thus, the only difference between the two codes is the use of the Cartesian or cylindrical grid Jacobian formulation. Data from Ref. 1 is also included on the charts for comparison as well as data from an axisymmetric version of the code.

Figures 2a and 2b show normalized values of density and pressure along the body surface. The stagnation point and singular line correspond to $\theta = 0$. The 3-D cylindrical, axisymmetric, and Ref. 1 data all compare very closely. The Cartesian code, however, has difficulty near the singular line. The peak values of density and pressure occur away from the stagnation line and are too high. The radial velocity is not zero along the stagnation line as it should be. Away from the singular line, the results from the Cartesian code gradually approaches that of the other solutions. A close-up of the surface pressure around the singular line region is shown in Fig. 2c. The Cartesian solution is clearly unsatisfactory exhibiting a sawtooth pattern. This is the consequence of the positive longitudinal flux being incorrectly set to zero along the singular line. The cylindrical code does a much better job of representing that flux. Note also the effect of the zeroth-order boundary condition on the 3-D cylindrical solution. The axisymmetric solution does not have a grid line at $y = 0$ but instead has two symmetric grid lines above and below the x-axis.

Figure 2d shows computed shock standoff distance as a function of θ around the body. Once again the cylindrical, axisymmetric, and Ref. 1 data correspond very closely. Another consequence of using the Cartesian code is that the stagnation line shock standoff distance is underpredicted by more than 10%. Away from the singular line, the shock standoff distance is overpredicted.

Normalized density, pressure, and u-velocity profiles along the stagnation line are shown in Figs. 3a-c. These plots also highlight the fact the 3-D Cartesian code underpredicts the shock standoff distance while the other three solutions are essentially identical. Figures 4 and 5 show density and pressure profiles along the 45 and 75 degree lines. The peak values computed by the two shock capturing codes are somewhat lower than the shock-fitted values from Ref. 1 as would be expected. The Cartesian code does somewhat better along these lines that are removed from the singular region. Pressure and shock standoff distance are somewhat over predicted.

The cylindrical formulation is equally effective when applied to viscous flows. Mach 31.7 perfect gas flow was computed over the Aeroassist Flight

Experiment (AFE) vehicle, shown in Fig. 6, using both the Cartesian and cylindrical formulations with the same singular line boundary conditions used in the sphere calculations. The Cartesian code had a great deal of difficulty resolving velocity and pressure near the singular line. A surface pressure profile plot along the pitch plane is shown in Figure 7. With the Cartesian solution, the distortion around the singular line causes two localized pressure peaks away from the stagnation point. Clearly, this is a non-physical distortion caused by the numerics of the solution process. This pressure distortion affects the pressure distribution in the entire subsonic region of the flow, which for the AFE vehicle is most of the forebody. This illustrates how important it is to accurately resolve the flow near the singular line. The cylindrical solution shows a smooth pressure distribution with the peak value at the stagnation line.

Finally, to show how readily extendable the cylindrical formulation is to real-gas flows, velocity magnitude contours using both Cartesian and cylindrical formulations are presented in Figs. 8a and 8b for Mach 31.7 viscous flow over the AFE vehicle at its flight trajectory point at 77.8 km. The solutions were computed using an explicit, finite-rate, thermochemical nonequilbrium flow solver[12]. The same behavior as seen in the perfect gas computations is evident here. The cylindrical formulation does a far superior job in resolving flow quantities near the singular line.

Results Using the Roe-Upwind Solver

Table 1. shows the various numerical experiments conducted to verify the accuracy of the Roe-upwind solver. As before, results from the inviscid computations are compared with the results of Ref. 1. To simulate the axisymmetric flow around the spherical body, either a grid consisting of three planes separated by 1 deg. angle, shown in Fig. 9 or a full three-dimensional grid around one-half of the body, similar to the grid shown in Fig. 1, is used. For inviscid cases, the grid points are placed uniformly between the body and the outer boundary and for viscous flows, the grid is stretched towards the wall. The singular line boundary exists in both the 3-plane grid and the full three-dimensional grid. Only explicit solutions were sought for this study and in all but one case, global time accuracy was maintained in obtaining solutions to the steady state. For the case where local time step was used, the step size in time was selected based on the maximum local eigenvalue and the grid size such that the local Courant number was less than unity. For the viscous cases on a stretched grid, the flow near the body may restrict the time step size based on viscous stability criterion. However in the cases studied here, the inviscid step size limitation from the shock region seems to determine overall time step size. Both the $L_2(\Delta Q)$ and Max (ΔQ) norms were monitored during the iterative process and the convergence criteria of at least 4 orders of magnitude reduction in both these norms were required. The 3-D code is vectorized and required 10 microseconds of CPU time on CRAY-YMP per grid point per iteration.

The computed solutions for the inviscid flow around the sphere geometry at a freestream Mach number of 20 are presented in terms of surface density, pressure and shock standoff distances in Figures 10 (a), (b) and (c) respectively. The coarse-grid first-order solution (case 1), coarse-grid second-order solution (case 2), fine-grid third-order accurate solution (case 5) and the solution from Ref.1 and are also compared in these Figures. The present computed solutions did not show any problem at or near the singular line region. The surface density, pressure and shock standoff distance comparisons between the present computations and that of Ref. 1 is found to be very good. The grid sensitivity analysis (case 2 and 5) did not show any significant difference , due to sufficient second/third-order solution accuracy, but the coarse-grid, first-order solution showed some differences, as seen in Figs. 10(a), (b) and (c).

To compare the solution accuracy across the shock, normalized density $(\frac{\rho}{\rho_\infty})$, normalized pressure $(\frac{p}{p_\infty})$ and normalized u-velocity ($\frac{u}{c_\infty}$, where c_∞ is the free-stream speed of sound) are shown in Figure 11(a), (b), and (c) respectively. The first-order solution, as expected, shows considerable shock spread compared to the higher-order solutions. The fine grid (case 5) solution captures the shock better and the shock location is also predicted well. The normalized density and pressure along $\theta = 45^\circ$ and $\theta = 75^\circ$ lines were compared and are shown in Figure 12 (a), 12(b), 13(a) and 13(b) respectively. Though the overall comparison between the present computations and the solution from Ref. 1 is good, the peak density and pressure behind the shock at $\theta = 75^o$ is underpredicted by the present shock capturing computations relative to the shock fitting values. This is to be expected.

The use of local time step to achieve faster convergence to steady state solution is common technique. The solution process, during convergence to steady state, is found to be non-conservative if local time step is employed. If the local maximum eigenvalues are significantly different (as the case is near the shock region, where $\max(\lambda^{upstream})/\max(\lambda^{downstream})$ is of the order of freestream Mach number) then the conservation is violated the most in such a region. Use of local time step may allow waves to travel at best possible speeds based on local conditions, but the solution is conservative and steady only if ΔQ at each and every grid point is guaranteed to be less than the convergence criterion. With the local time step method, moinitoring the local state variables at each grid point, such as the $\max\Delta Q$ norm, is necessary. In Figure 14, the stagnation density profiles from a apparently converged solution, based on L_2 norm, computed with local time step is shown. The solution near the singular line and near the shock has not converged completely. Further convergence to steady state was found necessary and was achieved by reducing the $\max\Delta Q$ norm. Hence caution is advised in the use of local time step method.

To further validate the present technique for viscous flows, an adiabatic and an isothermal wall boundary cases were computed with a viscous grid. The Reynolds number based on freestream conditions and the radius of the sphere was 3.7 x 10^6 and the wall temperature was set to freestream static temperature for the isothermal case. Surface pressure and shock standoff distances from the viscous computations are compared with the inviscid solutions in Figures 15 (a) and (b) respectively. The surface pressure has no significant effect due to the growth of the viscous boundary and shows smooth solution behavior near the singular line. The differences observed in the shock standoff distance is due to the viscous layer at the wall. The isothermal wall conditions (with cold wall boundary) has the largest thermal and momentum boundary layer and shows the maximum deviation for the inviscid shock standoff distance. In Figures 16 (a) and (b), density contours on the symmetry plane from the inviscid and isothermal cases are shown. The smooth variation of the contours near the singular line demonstrates the effectiveness of the present solution procedure.

To further demonstrate that the singular line boundary does not present any problem, the 3-D, inviscid, Mach 20, flow around the sphere at zero and 15 deg. angles of attack were computed using the present solver. The grid used in both these cases was the same and was similar to the grid used in case (2) except 12 circemferential planes were constructed to span one-half of the sphere. The singular line coincided with the freestream direction for the 0 deg. angle of attack case and for the 15 deg. angle of attack case, the freestream and the singular line were 15 deg. apart. The intent here was not only to demonstrate the effectiveness of obtaining accurate solutions when there is flow across the singular line, but also to show that the solution symmetry regardless of the location and orientation of the singular line. Since the geometry is a sphere, the 15 deg. angle of attack solution can be rotated by (-15) degrees and compared with the 0 deg. solution.

In Figure 17(a) and (b), pressure contours on the bi-symmetry plane are shown for the 0 deg. and 15 deg. angles of attack cases. In these figures, in addition to the pressure contour lines, the grid on the spherical surface and the singular line boundary are shown. The computed solution is very symmteric about the stagnation point in both these cases. The surface pressure on the bi-symmtery plane are compared with the solution of Ref. 1 in Figures 18 (a) and (b). The comparison is good and the location of the singular line has no effect on the solution. These two computations demonstrates the effectiveness of the present solution methodology to compute 3-D flows with grids that contain singular line boundaries.

Concluding Remarks

The methods presented in this study effectively reduce the difficulties associated with the singular line in 3-D blunt body flows. The first method reformulated the governing equations in terms of a modified definition of the grid Jacobian. The resulting 3-D solutions showed marked improvement over solutions when the usual, Cartesian grid Jacobian is used. The singularity is essentially moved to two source vectors which are not evaluated at the singular line. Both codes used identical grids, singular line boundary conditions, and first-order differencing of the inviscid fluxes. The Cartesian code underpredicted stagnation line shock standoff distance and placed the point of peak surface pressure away from the stagnation point. The cylindrical method was equally effective in improving viscous and real-gas solutions.

The second method, which utilizes finite-volume techniques to properly evaluate of the metric and Jacobian of the transformation and accurate boundary condition procedures, demonstrated that the singular line problem can easily be avoided for axisymmteric and 3- D flow problems. Though the present solution procedure is found to work well with Roe's upwind differencing technique and with MUSCL extrpolation with differential limiters, other forms of flux-splitting and flux-limiting schemes have yet to be explored.

Both of the methods presented in this study illustrate that the key to effectively treating the singular line boundary lies not in the boundary conditions themselves but rather in the proper determination of the metric and flux terms on the singular line.

Acknowledgment

Support for E. Venkatapathy was provided by NASA Grant NCC2-420.

References

[1]Lyubimov, A.N., and Rusanov, V.V., "Gas Flows Past Blunt Bodies, Part II. Tables of the Gasdynamic Functions, "NASA TT F-715, Feb, 1973.

[2]Peery, K. M., and Imlay, S. T., "Blunt-Body Flow Simulations, "AIAA Paper 88-2904, 24th Joint Propulsion Conference, Boston, MA, 1988.

[3]Shang, J.S. and Josyula, E., "Numerical Simulations of Non-Equilibrium Hypersonic Flow Past Blunt Bodies, "AIAA Paper 88-0512, AIAA 26th Aerospace Sciences Meeting, Reno, NV., Jan. 1988.

[4]Josyula, E., and Shang, J.S., "Numerical Simulation of Nonequilibrium Hypersonic Flow with Adaptive Grid, "AIAA Paper 90-1490, AIAA 21st Fluid Dynamics, Plasma Dynamics and Laser Conference, Seattle, WA, June 1990.

[5]Tam, L.T., and Li, C.P., "Comparison of Thermochemical Nonequilibrium Viscous Flowield Predictions for AFE Vehicle, "AIAA Paper 90-0141, AIAA 28th Aerospace Sciences Meeting, Reno, NV. 1990.

[6]Gnoffo, P. A., Price, J. M., and Braun, R. D., "On the Computation of Near Wake, Aerobrake Flowfields, "AIAA Paper 91-1371, AIAA 26th Thermophysics Conference, Honolulu, HA, June, 1991.

[7] Roe, P.L., "Some Contributions to the Modelling of Discontinuous Flows, "Large-Scale Computations in Fluid Mechanics,*Lectures in Applied Mathematics*, Vol. 22, Part 2, American Mathematical Society, 1985, pp. 163-193.

[8] Anderson, W.K., Thomas, J.L., and Van Leer, B., "Comparison of Finite Volume Flux Vector Splittings for the Euler Equations, "*AIAA Journal* , Vol. 24, 1986, pp 1453-1460.

[9] Vinokur, M.,"An Analysis of Finite-Difference and Finite-Volume Formulations of Conservation Laws, "NASA CR 177416, June 1986.

[10] Obayashi, S.,"Numerical Simulation of Underexpanded Plumes using Upwind Algorithms, "AIAA Paper 88-4360, AIAA Atmospheric Flight Mechanics Conference, 1988.

[11] Yee, H.C.,"Upwind and Symmetric Shock-Capturing Schemes, "NASA TM 89464, 1987.

[12]Palmer, G.E., "Enhanced Thermochemical Nonequilibrium Computations of Flow Around the Aeroassist Flight Experiment Vehicle, "AIAA Paper 90-1702, Seattle, 1990.

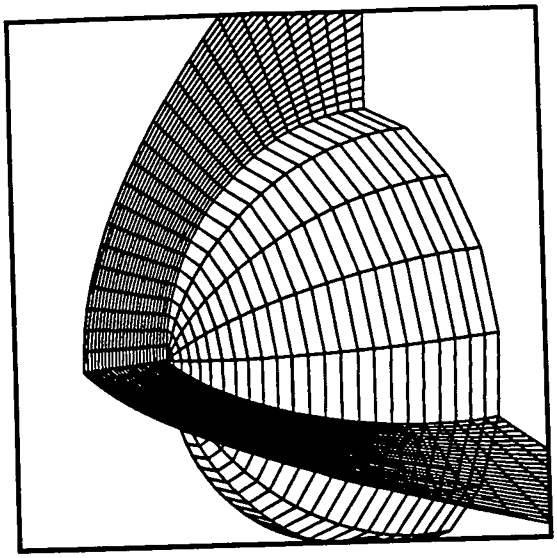

Figure 1. Generic blunt body grid with axis-singular line.

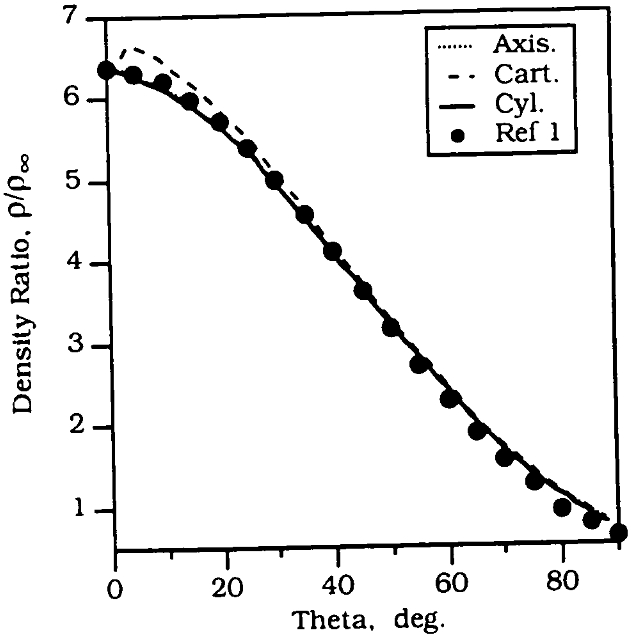

Figure 2(a). Density along the surface

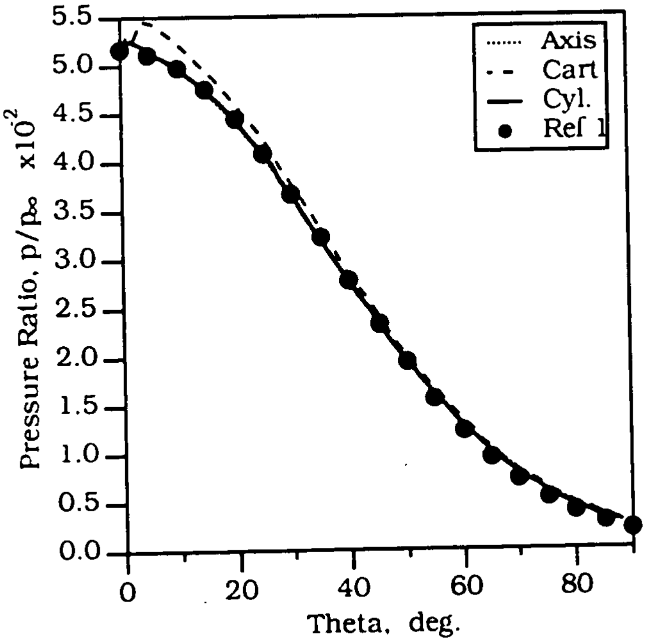

Figure 2(b). Pressure along the surface

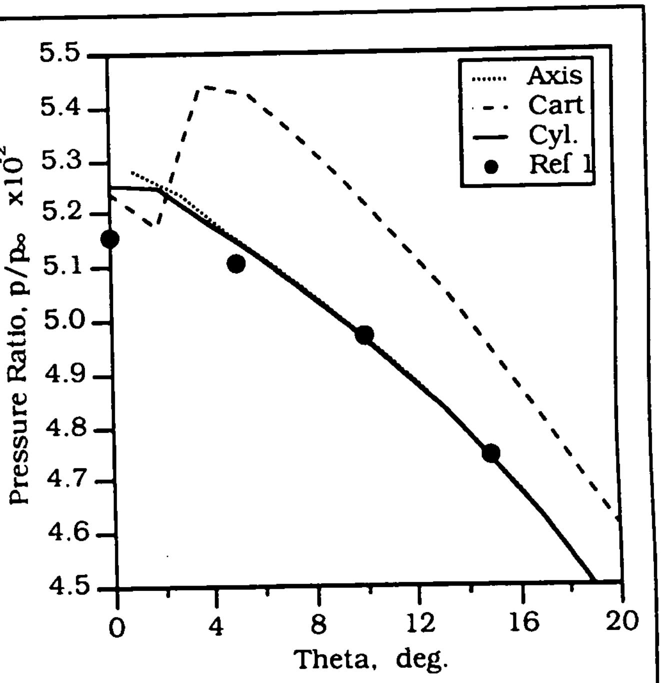

Figure 2(c). Pressure along the surface : close up near the singularity

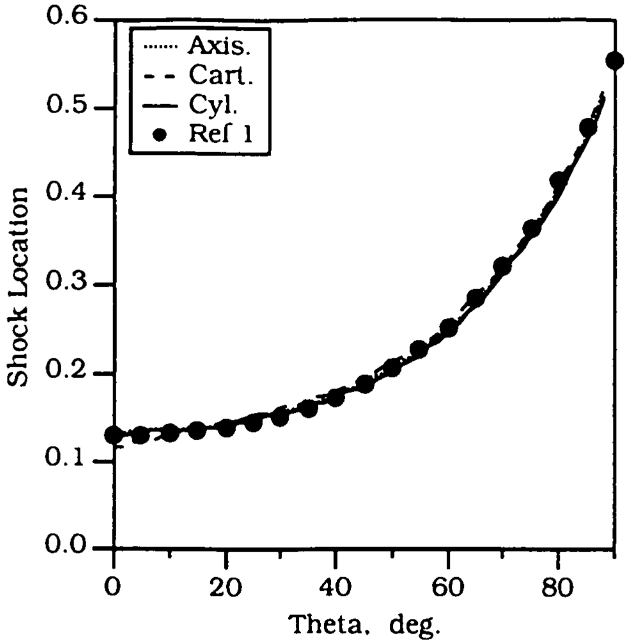

Figure 2(d). Shock standoff distance

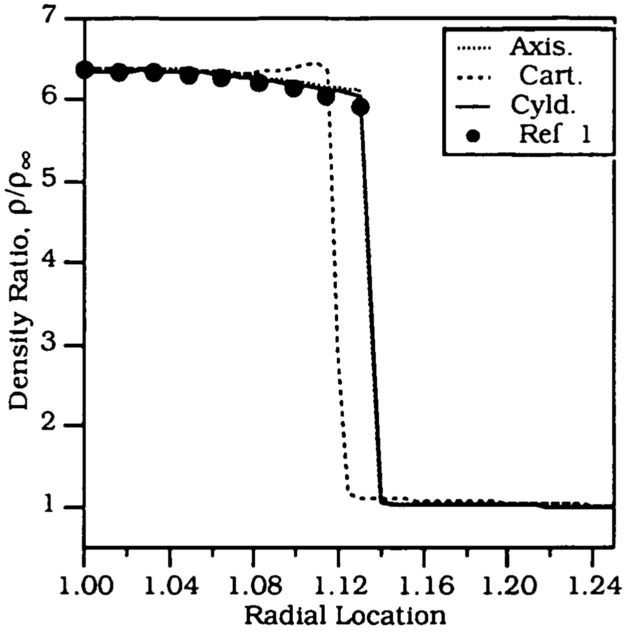

Figure 3(a). Density along the stagnation line.

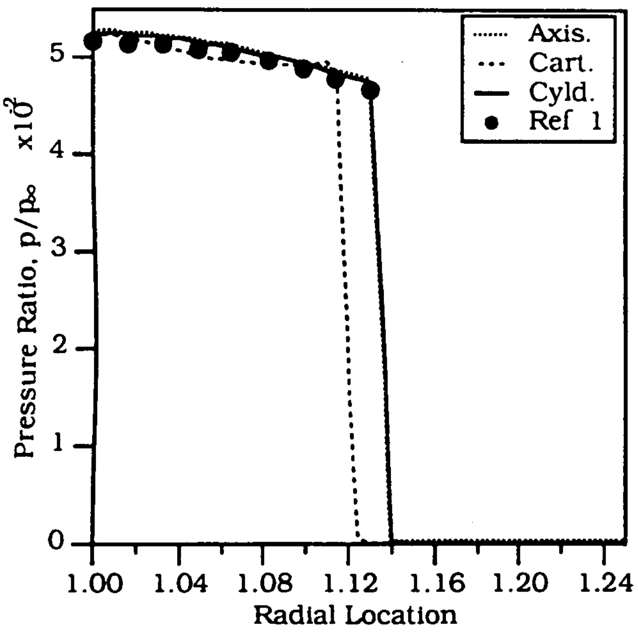

Figure 3(b). Pressure along the stagnation line.

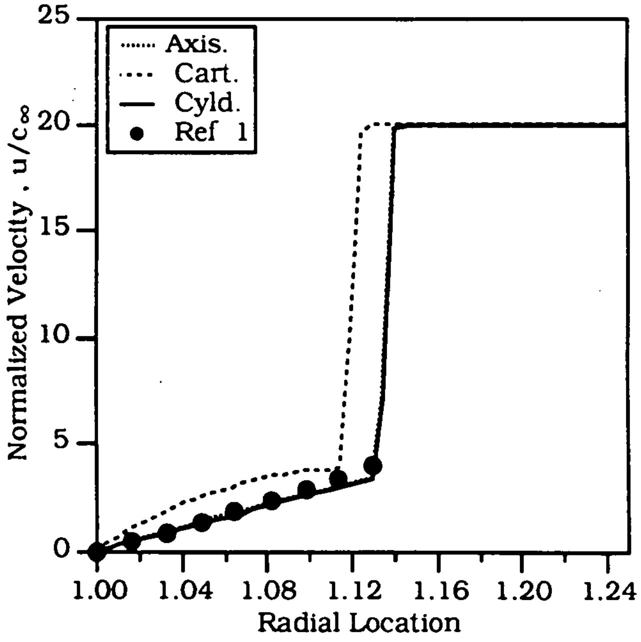

Figure 3(c). U-velocity along the stagnation line.

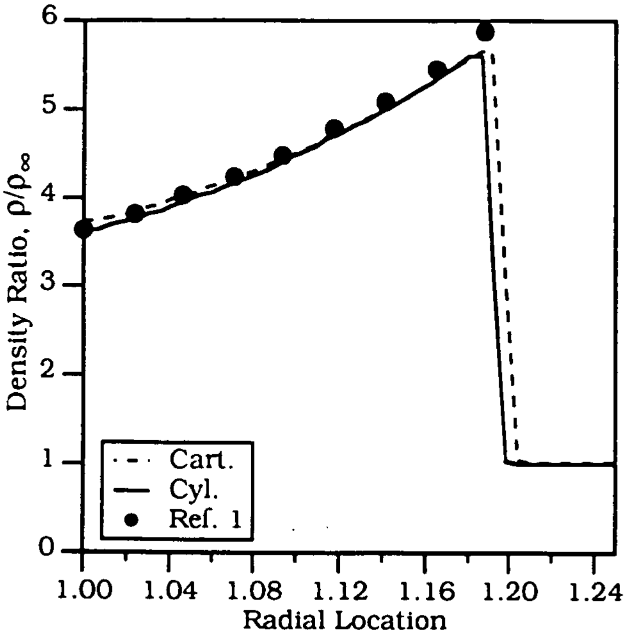

Figure 4(a). Density along θ = 45 deg. line

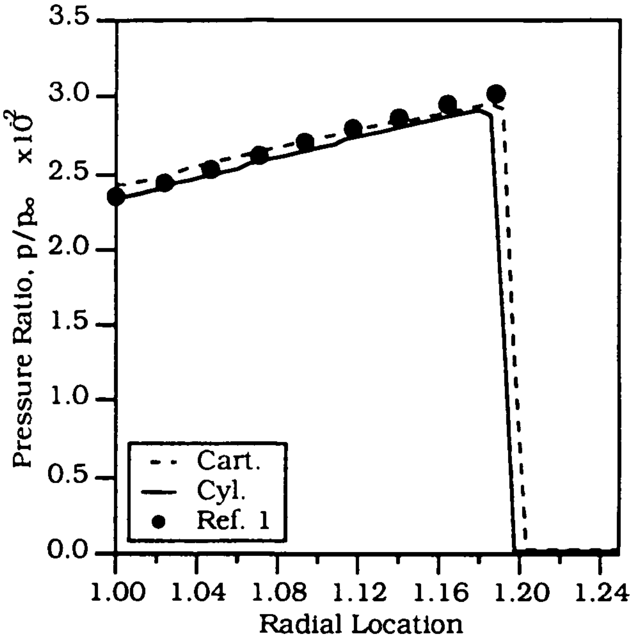

Figure 4(b). Pressure along θ = 45 deg. line

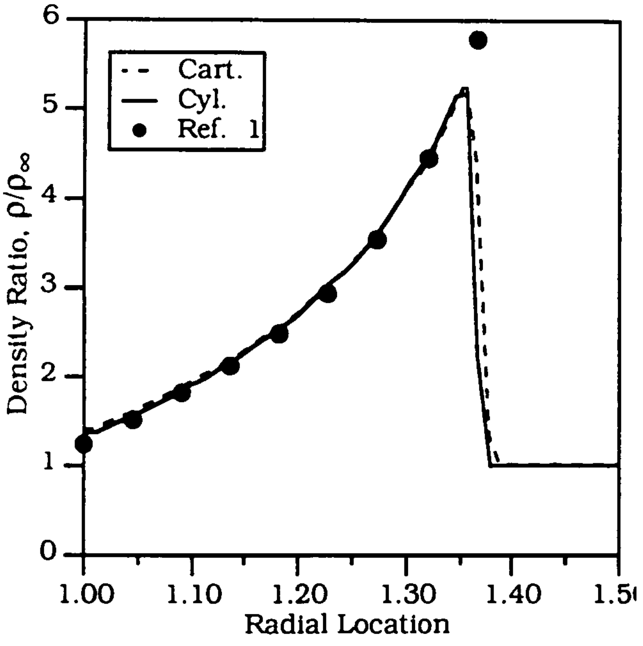

Figure 5(a). Density along θ = 75 deg. line

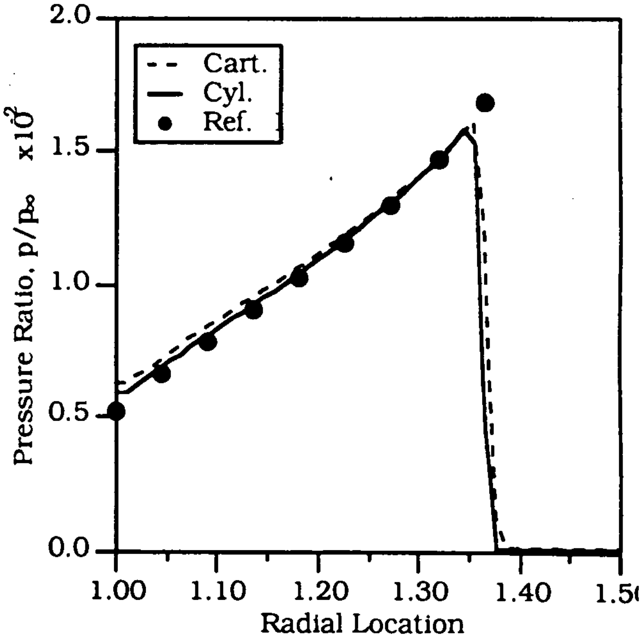

Figure 5(b). Pressure along θ = 75 deg. line

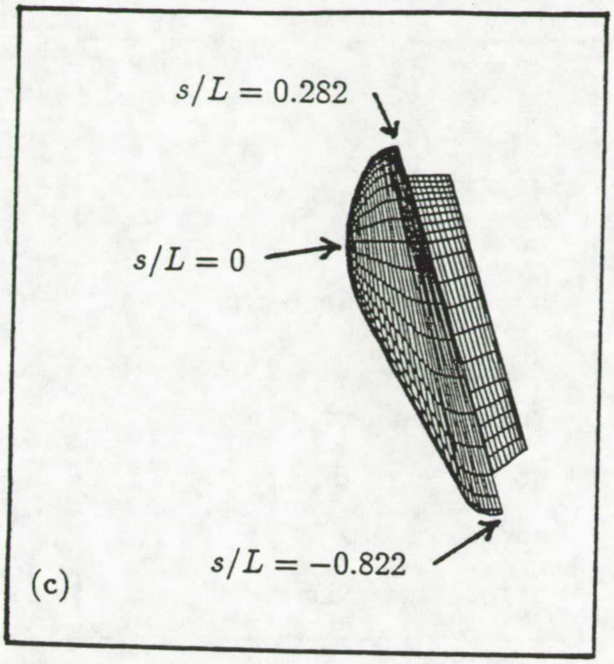

Figure 6. AFE Geometry and surface grid.

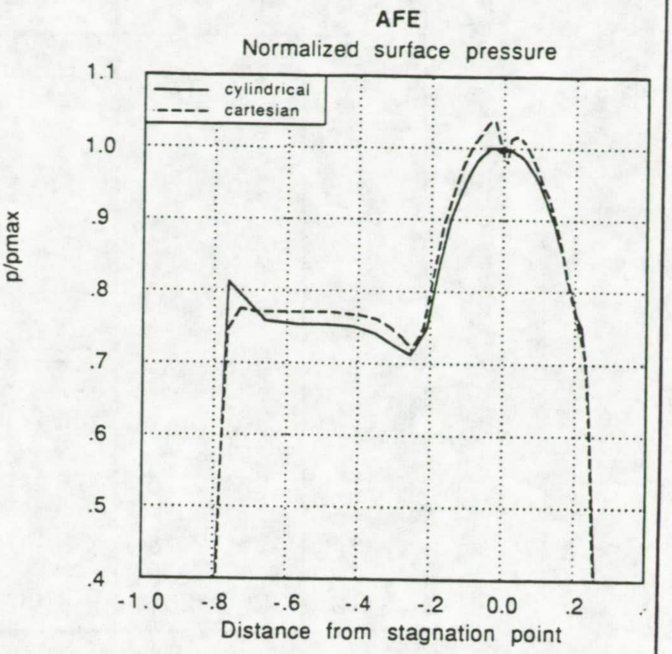

Figure 7. Normalized surface pressure along the pitch plane

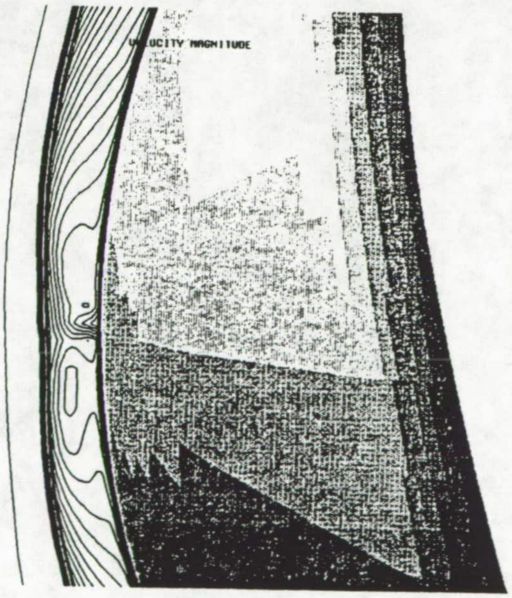

Figure 8(a). Velocity magnitude contours - Cartesian formulation.

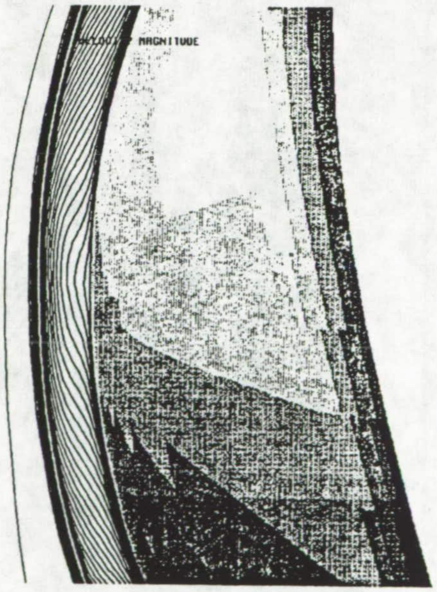

Figure 8(b). Velocity magnitude contours - cylindrical formulation.

Case	Grid Size	Order	Comments
1	25*3*25	1st Order	Inviscid
2	25*3*25	2 & 3 Order	Inviscid
3	49*3*49	1st Order	Inviscid
4	49*3*49	2 & 3 Order	Inviscid, variable/local time steps
5	49*3*49	2 & 3 Order	Inviscid, global time step
6	49*3*49	3rd Order	Viscous, adiabatic wall
7	49*3*49	3rd Order	Viscous, isothermal wall
8	25*12*25	3rd Order	Inviscid , $\alpha = 0.0$
9	25*12*25	3rd Order	Inviscid, $\alpha = 15$
10	25*3*25	3rd Order	Inviscid, adapted grid

Table 1. Details of the cases run with the 3-D solver

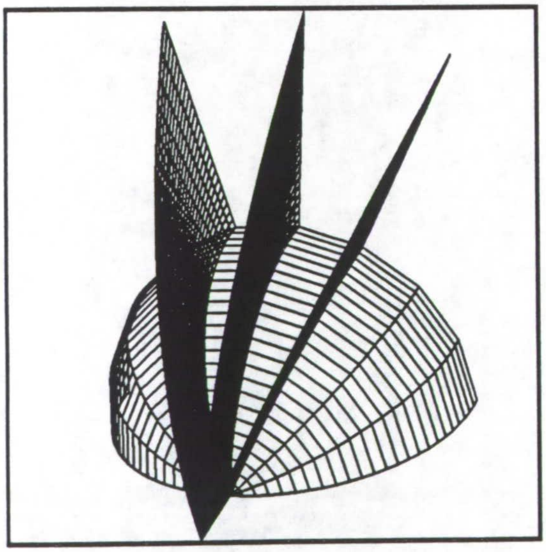

Figure 9. Three-plane 3-D grid for axisymmteric flow

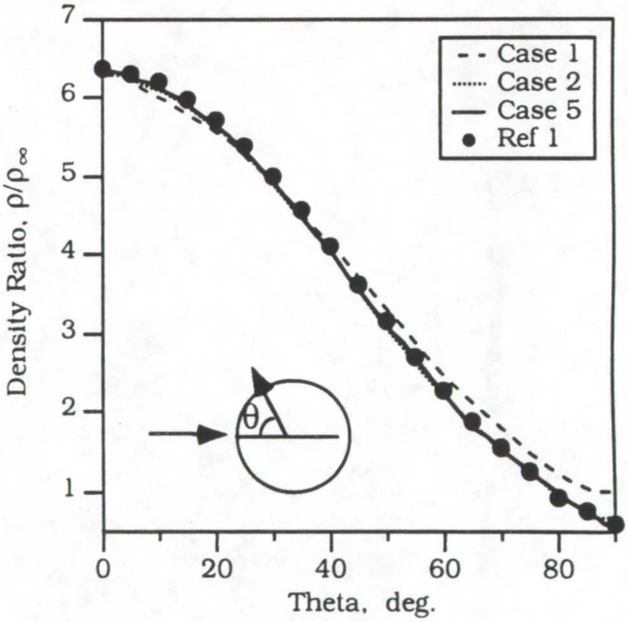

Figure 10(a) . Density along the surface

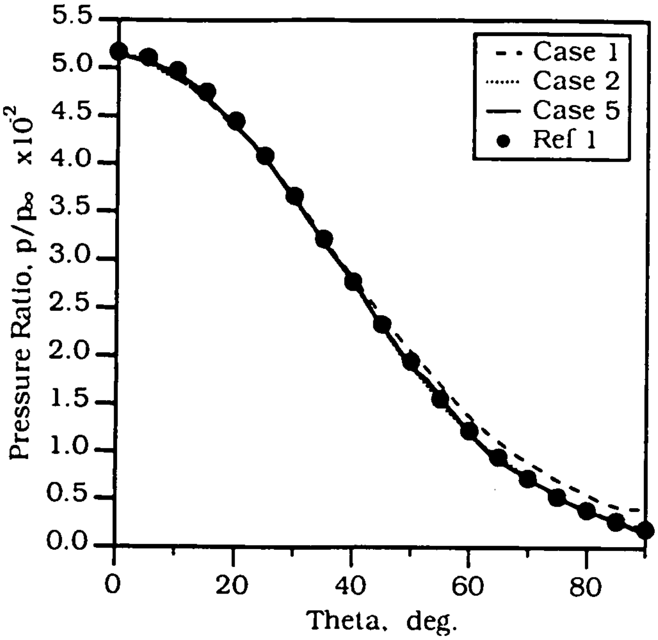

Figure 10(b). Pressure along the surface

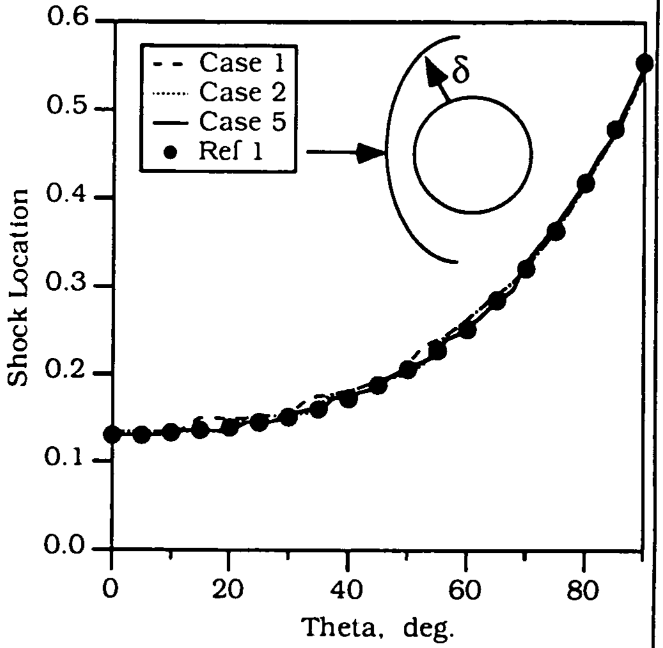

Figure 10(c). Shock standoff distance

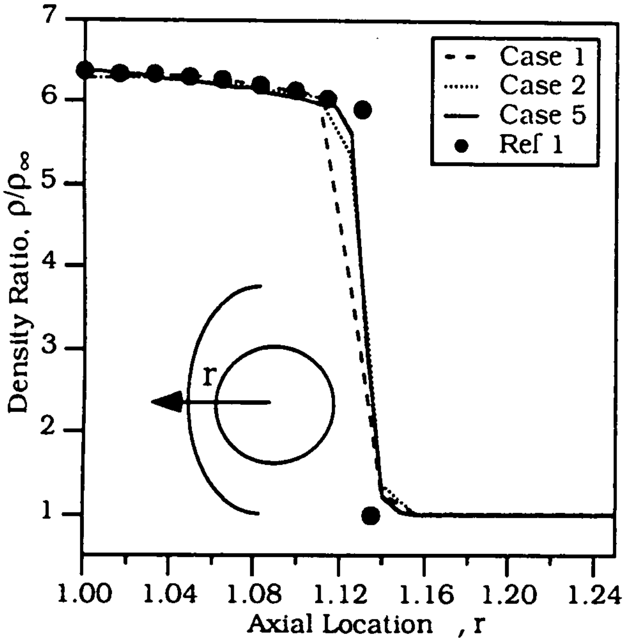

Figure 11(a). Density along stagnation line

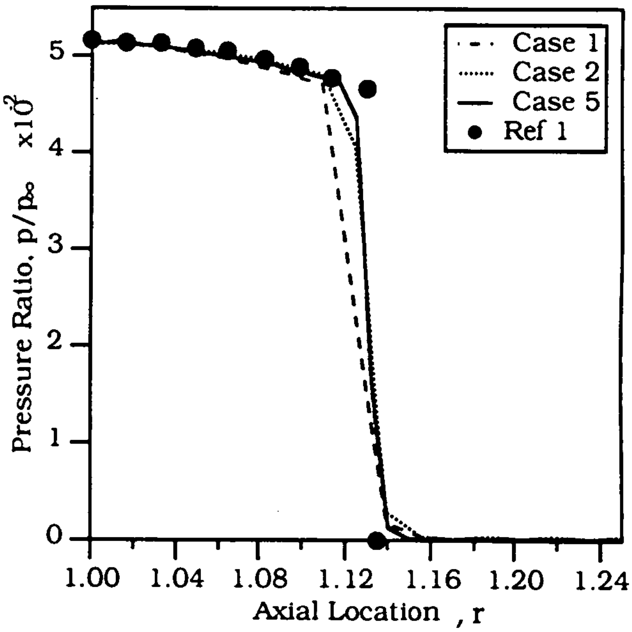

Figure 11(b) Pressure along stagnation line

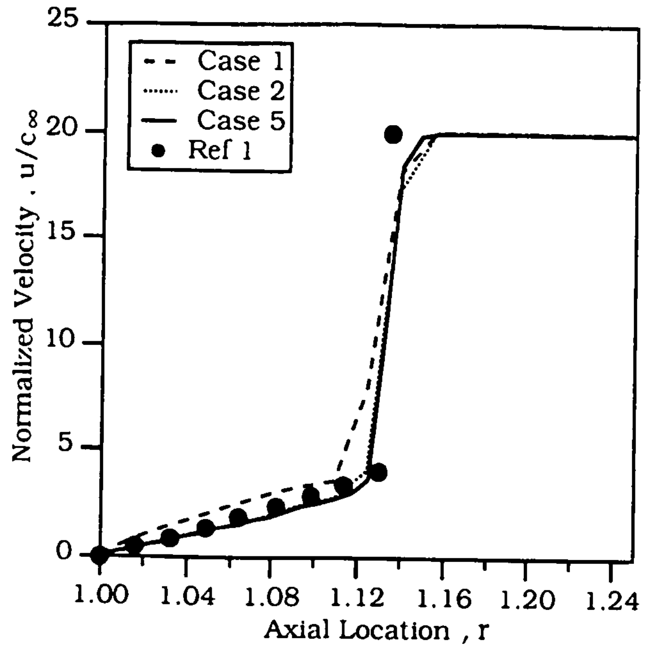

Figure 11(c) Velocity along stagnation line

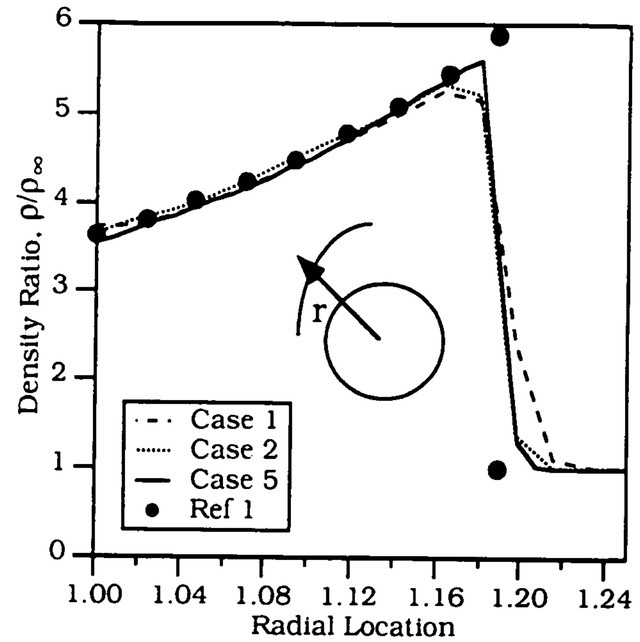

Figure 12(a). Density along Θ = 45 deg. line

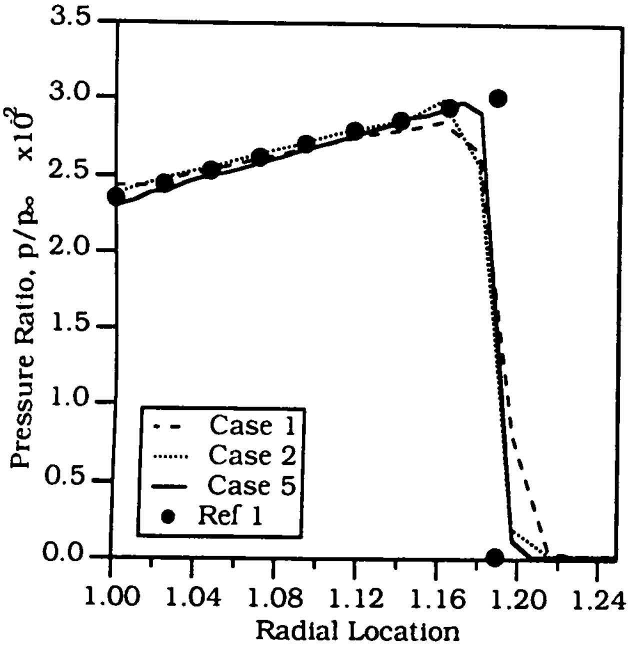

Figure 12(b). Pressure along Θ = 45 deg. line

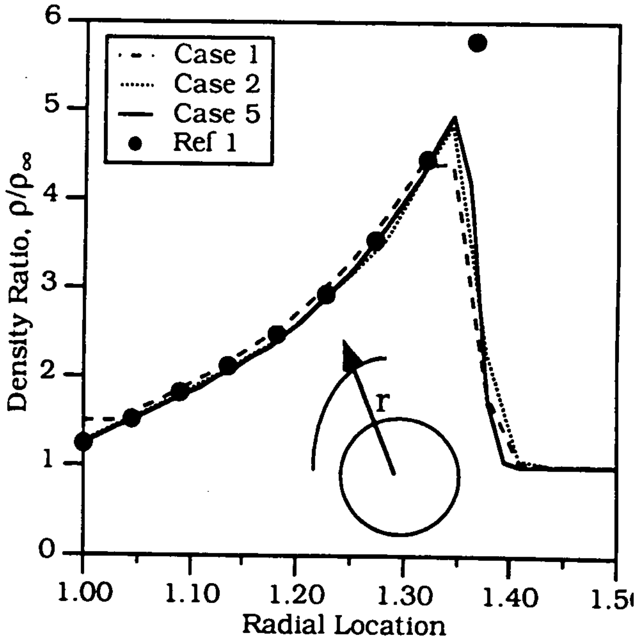

Figure 13(a). Density along Θ = 75 deg. line

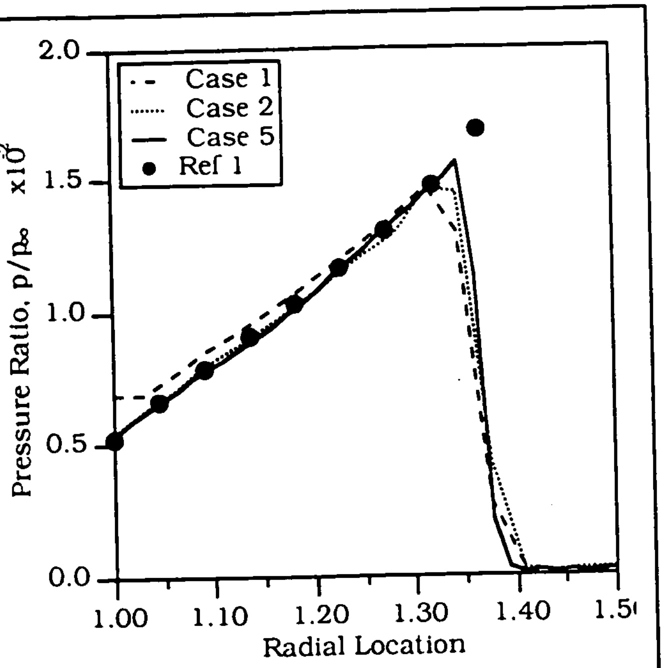

Figure 13(b). Pressure along Θ = 75 deg. line

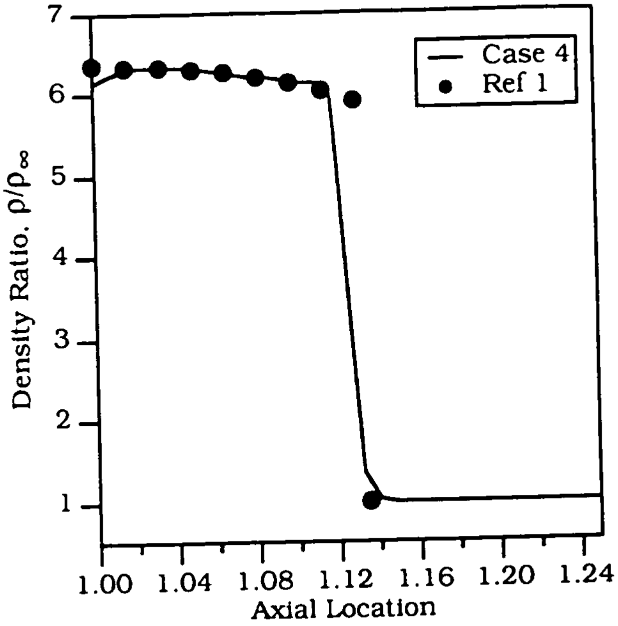

Figure 14. Stagnation line density profile : use of local time step.

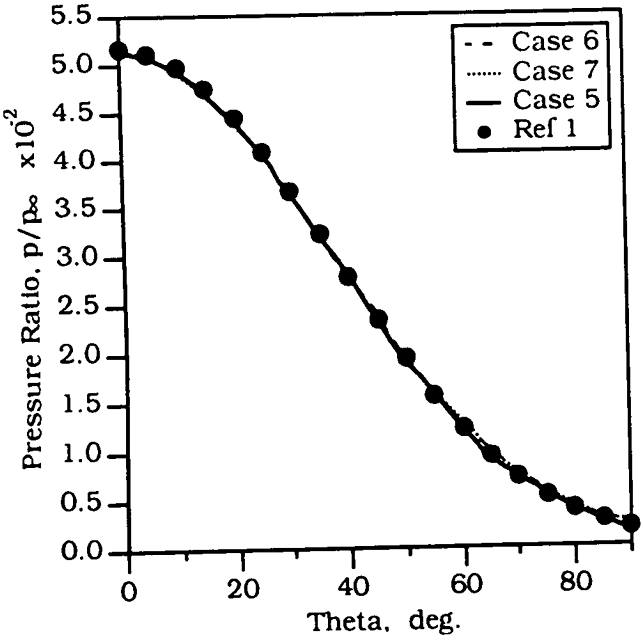

Figure 15(a). Pressure along the surface : Adiabatic, isothermal and inviscid cases

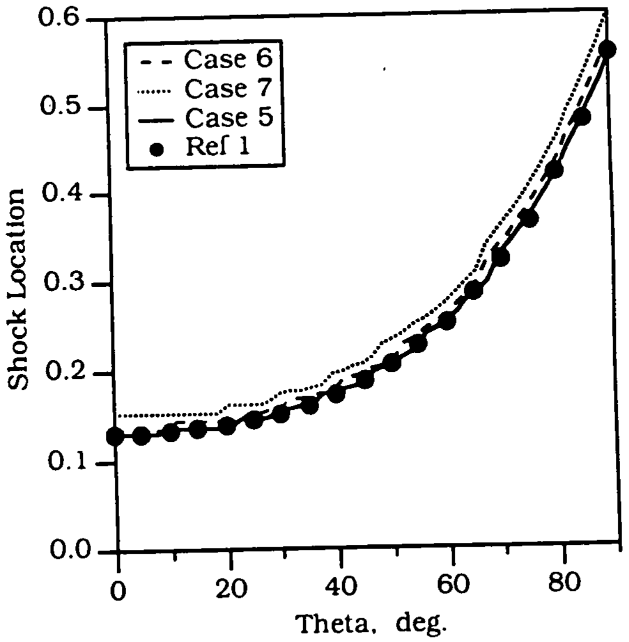

Figure 15(b). Shock standoff distance : Adiabatic, isothermal and inviscid cases

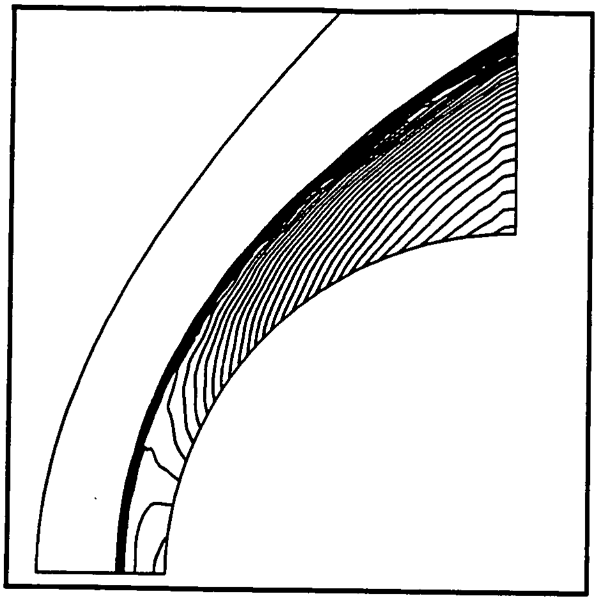

Figure 16(a). Density Contours on the symmetry plane , invscid conditions (case 5)

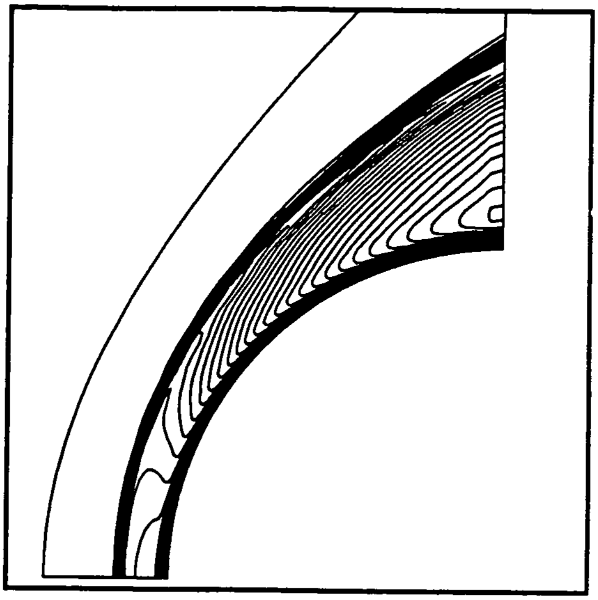

Figure 16(b). Density Contours on the symmetry plane : viscous conditions (case 7)

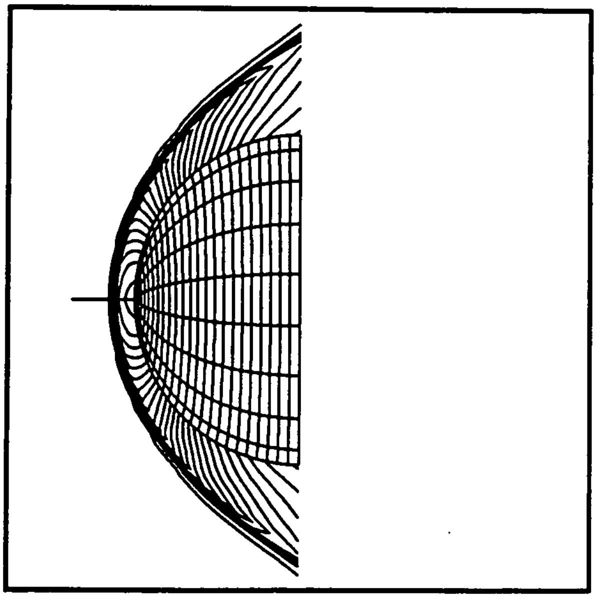

Figure 17(a). Pressure contours on the bi-symmtery plane - Case 8

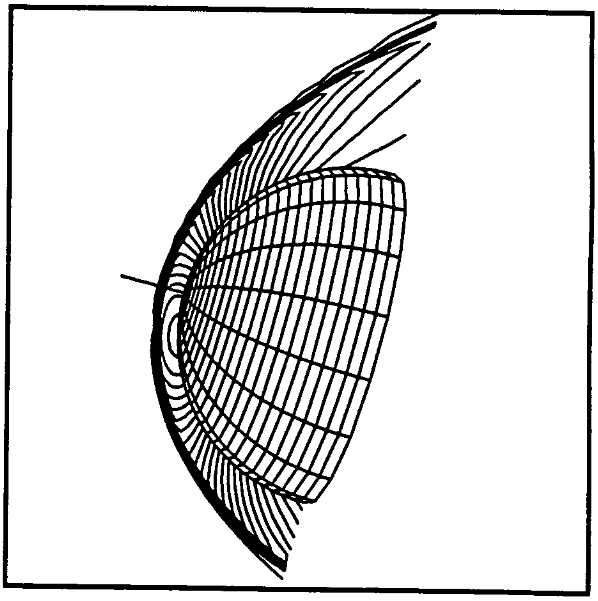

Figure 17(b). Pressure contours on the bi-symmtery plane - Case 9

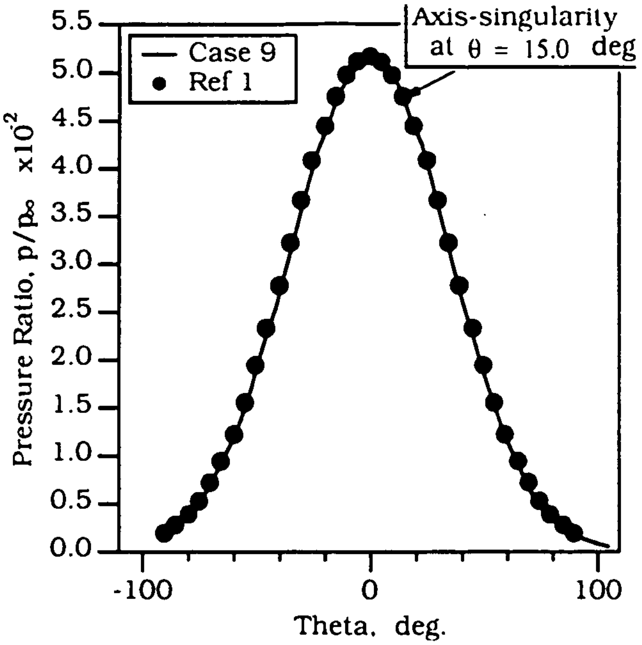

Figure 18(a). Surface pressure on the bi-symmtery plane - case 8

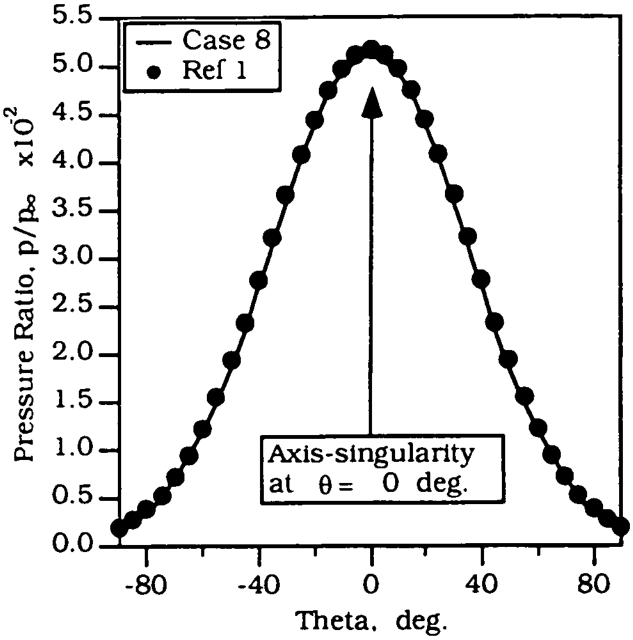

Figure 18(b). Surface pressure on the bi-symmtery plane - case 9

Appendix F

Computation of Unsteady Shock-Induced Combustion Using a Logarithmic Form of the Species Conservation Equations

Gregory J. Wilson*

Eloret Institute

3788 Fabian Way

Palo Alto, California 94303

Myles A. Sussman**

Department of Aeronautics and Astronautics

Stanford University, Stanford, CA 94305

---

* Currently Research Scientist, Member AIAA. Mailing address: NASA Ames Research Center, MS 230-2, Moffett Field, CA 94305

** Graduate Student, Student Member AIAA

Abstract

Numerical simulations are used to investigate periodic combustion instabilities observed in ballistic-range experiments of blunt bodies flying at supersonic speeds through hydrogen-air mixtures. The computations are validated by comparing experimental shadowgraphs to shadowgraphs created from the computed flowfields and by comparing the frequency of the experimental and computed instabilities. The numerical simulations utilize a logarithmic transformation of the species conservation equations which recently has been proposed as a way to reduce grid requirements for computing flows with shock-induced combustion. The transformation is applied to the Euler equations coupled to a detailed hydrogen-air chemical reaction mechanism with thirteen species and thirty-three reactions. The resulting differential equations are solved using a finite-volume formulation and a two-step predictor-corrector scheme to advance the solution in time. Results are presented and compared for both a flux-vector splitting scheme and an upwind TVD scheme. The simulations add insight into the physical processes observed in the experiments and help establish the advantages of a logarithmic form of the species conservation equations for combustion flows. The usefulness of the ballistic-range experiments for the validation of numerical methods and chemical kinetic models is also demonstrated.

Introduction

Ballistic-range experiments performed in the 1960s and early 1970s[1-7] provide excellent data for studying the coupling between supersonic fluid dynamics and nonequilibrium chemical kinetics as well as for evaluating combustion flow codes. In these experiments, small projectiles were fired at supersonic speeds into a variety of premixed combustible mixtures. Shadowgraphs of the flowfields exhibit two distinguishing features: one is the bow shock ahead of the projectile and the other is an energy-release front created by the ignition of the heated mixture behind the bow shock. Both features can be seen in the shadowgraph by Lehr[5] of a steady ballistic-range experiment at Mach 6.46. The region between the bow shock and the energy-release front is called the induction zone and it exists because there is an ignition delay caused by chemical nonequilibrium. The induction zone is characterized by near-constant values (the post-shock values) of temperature, density, pressure, and velocity. The size of the induction zone is determined by the fluid speed downstream of the shock and the ignition time corresponding to the post-shock conditions. When ignition occurs, the energy is released over an interval much shorter than the ignition delay time and appears as a discontinuity which is referred to as the energy-release front. Across the energy-release front the pressure is nearly constant, the temperature rises, and the density drops. Such behavior can be seen in the ballistic-range shadowgraph of Figure 1 where the shift from light to dark across the bow shock corresponds to the density increase across the shock while the shift from dark to light across the energy-release front indicates a drop in density.

Depending on the conditions of the experiment, one will observe either steady or unsteady flow. Projectile speeds greater than the detonation wave speed tend to induce steady flows while speeds less than the detonation wave speed can produce unsteady flows. The unsteady flows are characterized by two different regimes. One is called the regular regime and the other is called the large disturbance or irregular regime. All the unsteady simulations presented in this work are in the regular regime (see Alpert and Toong[7] for more on the large disturbance regime). Figures 2*a* and 2*b* show an unsteady ballistic-range experiment with the same free stream conditions as in Figure 1 (the detonation wave speed is Mach 5.11) except that the projectile speed is Mach 4.79. The shadowgraphs reveal remarkable high-frequency oscillations. The frequency of the observed instability is approximately 720 KHz as deduced from the the projectile speed and counting the number of oscillations which occur over a known distance. Figures 2*a* and 2*b* are from the same ballistic-range shot but show different view angles. The view axis of Figure 2*a* is perpendicular to the flight axis and Figure 2*b* is off-axis and reveals some of the three-dimensional structure of the flowfield. While being complex in many ways, the physics of these ballistic-range flows are predominantly driven by reaction kinetics and convection phenomena; therefore, the complications and uncertainties of diffusion and mixing are removed from the problem. As a result, differences between the experimental data and numerical calculations can be attributed either to numerical errors or to improperly modeled chemical kinetics.

An earlier work by Wilson and MacCormack[8] focused on the steady ballistic-range experiments and established the physical and numerical modeling requirements for accurate computations of these flows. It was shown that one of the most challenging aspects is providing adequate resolution in the induction zone between the bow shock and the energy-release front. Fine grid resolution is required in this region not because there are large changes in the flow quantities such as pressure, density, or velocity (these quantities are nearly constant in the induction zone) but because the mass-fractions of the important radical species change exponentially in this region. Adaptive grid techniques offer one way to efficiently distribute points so that grid resolution is provided where it is needed most. These techniques, however, are not always adequate. The induction zone may cover such a large region of the flowfield that grid requirements still remain large. Also, complex flow structures such as those seen in the unsteady ballistic-range cases require very sophisticated (and probably very expensive) grid adaption techniques. Furthermore, the small grid spacings in the adapted regions result in undesired time step limitations.

To avoid small grid spacing in the induction zone, Sussman and Wilson[9] proposed a logarithmic transformation of the species conservation equations. The reasoning for this transformation is discussed below. Figure 3 shows the mass fraction of the hydroxyl radical (OH) in the induction zone for the case of shock-induced combustion which was presented by Sussman and Wilson.[9] The exponential growth of the hydroxyl mass fraction is seen as linear growth on the logarithmic scale. Many grid points are required to accurately capture this growth because a finite-difference approximation for a derivative of an exponentially varying function can result in large errors. In contrast, fewer points are needed to resolve the linear behavior seen on the logarithmic scale.

The use of the logarithmic transformation allows accurate simulations of both the steady and unsteady ballistic-range cases on grids more coarse than have been used in previous works. The reduced grid densities make it possible for the first time to simulate the unsteady ballistic-range cases with a detailed chemical kinetic model. The chemical kinetic model used in this work can be found in Wilson and MacCormack.[8] It is the mechanism proposed by Jachimowski[10] containing 13 chemical species and 33 reactions except that one of the reaction rate expressions (the expression most influential for ignition times) has been replaced by an expression recommended by another source. This modification was found by Wilson and MacCormack[8] to give better agreement with experiment. Additional details on the chemical kinetics are found in Wilson.[11]

The simulations of the unsteady flows in this work add insight into the combustion instabilities observed in ballistic-range experiments and allow previously proposed mechanisms for the instabilities to be assessed. In particular, this work considers the wave interaction mechanism of McVey and Toong[6] and the modified mechanism proposed by Matsuo and Fujiwara[12]. McVey and Toong developed their mechanism by using experimental data and analytical calculations. Matsuo and Fujiwara used modern computational fluid dynamics techniques, fine grids, and a two-equation, two-step combustion model to do qualitative simulations which led them to propose their modified mechanism. The use of detailed combustion kinetics in this work allows quantitative studies and direct comparison to experiment to be made. The experimentally measured oscillation frequencies are compared to the values predicted by numerical simulations. In addition to adding greater physical understanding, the current method also provides a tool to validate and possibly "tune" proposed chemical kinetic models.

Logarithmic Form of the Species Conservation Equation

This section gives an overview of the logarithmic transformation of the species conservation equations as presented by Sussman and Wilson.[9] The transformation is based on the definition

$$\pi_s \equiv \rho \ln\left(\frac{\rho_s}{\rho}\right) \equiv \rho \ln(c_s), \tag{1}$$

where ρ is the total density, ρ_s is the density of species s, and c_s is the mass fraction of species s. When c_s is a exponentially varying quantity, π_s is a linearly varying quantity (assuming constant ρ). A special property of the relationship in Equation (1) is that it can be used along with the total mass conservation equation,

$$\frac{\partial}{\partial t}\rho + \frac{\partial}{\partial x_j}\rho u_j = 0, \tag{2}$$

to transform the species mass conservation equation (neglecting diffusion),

$$\frac{\partial}{\partial t}\rho_s + \frac{\partial}{\partial x_j}\rho_s u_j = w_s, \tag{3}$$

into a transformed species equation,

$$\frac{\partial}{\partial t}\pi_s + \frac{\partial}{\partial x_j}\pi_s u_j = w_s \frac{\rho}{\rho_s}, \tag{4}$$

where u_j is the j^{th} component of velocity and w_s is the chemical source term for species s. The transformation from Equation (2) to (4) retains conservation form.

In theory, all of the species mass conservation equations can be replaced with Equation (4). In practice, however, this is not done. Although Equation (4) is in conservation form, it does not guarantee conservation of mass or conservation of the individual elements. Enforcement of these constraints is achieved by replacing some of the logarithmic equations with element mass conservation equations which are written in the form

$$\frac{\partial}{\partial t}\rho_e^\star + \frac{\partial}{\partial x_j}\rho_e^\star u_j = 0, \tag{5}$$

where $\rho_e^\star$ is the total density of element e contained in all of the species (the * is used to avoid confusion between element and species densities; $\rho_N^\star \neq \rho_N$). There are as many of these equations as there are elements in the chemical model. The total density is given by

$$\rho = \sum_{e=1}^{N_{elements}} \rho_e^\star. \tag{6}$$

The chemical reaction mechanism used in this work involves 13 species: N_2, O_2, H_2, NO, OH, NO_2, HNO, HO_2, H_2O, H_2O_2, N, O, H. Since three elements are present in the mechanism (N, O, H), three equations of the form of Equation (5) are required. The densities $\rho^\star_N$, $\rho^\star_O$, and $\rho^\star_H$ are defined using expressions which are the sum of the contributions from each of the species containing the element of interest. For example, the expression for $\rho^\star_N$ depends on N_2, NO, NO_2, HNO, and N and is written

$$\frac{\rho^\star_N}{M_N} = 2\frac{\rho_{N_2}}{M_{N_2}} + \frac{\rho_{NO}}{M_{NO}} + \frac{\rho_{NO_2}}{M_{NO_2}} + \frac{\rho_{HNO}}{M_{HNO}} + \frac{\rho_N}{M_N}. \tag{7}$$

where M_s is the molecular mass of species s. The choice of which three species conservation equations to replace with element mass conservation equations is not unique. The selection of N_2, O_2, and H_2 seems appropriate because these species do not exhibit exponential growth of mass fraction. The removal of these 3 species conservation equations means that the corresponding 3 species densities do not appear in the set of conserved variables. They can, however, be written in terms of the conservation variables with the equations of the type in Equation (7). The remaining ten species conservation equations are written in the logarithmic form of the mass conservation equation, Equation (4) (for species NO, OH, NO_2, HNO, HO_2, H_2O, H_2O_2, N, O, and H).

Numerical Formulation

This section presents the Euler equations with the logarithmic form of the species conservation equations. The 13 species mass conservation equations of the conventional formulation have been replaced by equations of similar form except that 3 are elemental mass conservation equations (See Equation (5)) and 10 are in the logarithmic variable π_s (See Equation (4)). The momentum and energy equations in the logarithmic formulation are the same as they were in the conventional formulation. In vector notation the governing equations are written

$$\frac{\partial U}{\partial t} + \frac{\partial F}{\partial x} + \frac{\partial G}{\partial y} = W, \tag{8}$$

where U is the state vector of conserved quantities, F and G are the convective (inviscid) flux vectors in the x and y coordinate directions, respectively, and W is the vector of source terms. These vectors are given below:

$$U = \begin{pmatrix} \rho_N^\star \\ \rho_O^\star \\ \rho_H^\star \\ \pi_{NO} \\ \vdots \\ \pi_H \\ \rho u \\ \rho v \\ E_v \\ E \end{pmatrix}, \quad F = \begin{pmatrix} \rho_N^\star u \\ \rho_O^\star u \\ \rho_H^\star u \\ \pi_{NO} u \\ \vdots \\ \pi_H u \\ \rho u^2 + p \\ \rho uv \\ uE_v \\ u(E+p) \end{pmatrix}, \quad G = \begin{pmatrix} \rho_N^\star v \\ \rho_O^\star v \\ \rho_H^\star v \\ \pi_{NO} v \\ \vdots \\ \pi_H v \\ \rho uv \\ \rho v^2 + p \\ vE_v \\ v(E+p) \end{pmatrix}, \quad W = \begin{pmatrix} 0 \\ 0 \\ 0 \\ w_{NO}/c_{NO} \\ \vdots \\ w_H/c_H \\ 0 \\ 0 \\ w_v \\ 0 \end{pmatrix}, \quad (9)$$

where E_v is vibrational energy per unit volume, w_v is the source term representing vibrational relaxation, E is the total energy per unit volume, and p is pressure. A separate vibrational energy equation is not required for the present computations but has been retained from previous work. For the cases presented here, thermal equilibrium is simulated by using a small time constant for vibrational relaxation.

In Equation (8), pressure is a homogeneous function of degree one in the conserved variables U and the flux Jacobians ($\frac{\partial F}{\partial U}$ and $\frac{\partial G}{\partial U}$) have the same eigenvalues as that of the formulation with the conventional form of the species mass conservation equations. Therefore, existing numerical techniques can be applied in a straightforward manner. In this work, two commonly used shock-capturing numerical techniques are employed. One is a modified Steger-Warming flux-vector splitting technique based on work by MacCormack[13] and Candler[14] (this method shall be referred to as the flux-vector splitting scheme) and the other is the Harten-Yee upwind TVD (non-MUSCL) scheme[15] (referred to as the upwind TVD scheme). Both techniques are spatially second order and solved in a point-implicit manner. That is, the convective terms are treated explicitly whereas the source terms are treated implicitly in time (because of the small time scales of the combustion chemistry and vibrational relaxation). Therefore, a block inversion is required at each point at each time step. Details on the flux-vector splitting scheme using the logarithmic formulation can be found in Wilson.[11]

Numerical Simulations

This section presents numerical simulations of ballistic-range shadowgraphs by Lehr.[4,5] The particular experiments of interest used spherical-nosed projectiles with cylindrical afterbodies of 15 millimeters diameter. The cases include a range of Mach numbers so that both steady and unsteady flows are represented. All the cases to be considered have freestream with a temperature of 292 K, a pressure of 320 mm Hg, and a premixed stoichiometric hydrogen-air mixture. At these conditions, the detonation wave speed is Mach 5.11.

Before unsteady simulations are presented, a simulation of the steady Mach 6.46 case in Figure 1 is shown to demonstrate the advantage of the logarithmic formulation and to give an understanding of why it is practical to use this formulation for the unsteady cases. Figure 4 contains density contours for computations of the Mach 6.46 case using flux-vector splitting and the upwind TVD methods, respectively. Both computations use the 52 × 52 grid shown in Figure 5. The experimental bow shock and energy-release front positions are overplotted on the density contours and show that both numerical methods provide good agreement with the experiment. A numerical simulation using the conventional form of the species conservation equations can be found in Wilson and MacCormack.[8] Good agreement with experiment was found in that work as well but a 321 × 64 (321 points around the body and 64 points normal to the body) mesh with grid adaption was required. The grid for the calculation using the logarithmic formulation is more than 8 times smaller because the induction zone is adequately resolved with fewer grid points.

Simulations of Lehr's unsteady Mach 4.79 case shown in Figure 2 are now presented. The computations were started from a flowfield that was initially set to freestream conditions everywhere and advanced in time without chemistry until a bow shock was established at which time the combustion chemistry was turned on. No other special procedures were used. The computations used a nearly equally-spaced 375 × 161 grid. The fine grid was not needed to capture the unsteady behavior but was used to resolve some of the finer structures of the flow. Computation on a 375 × 81 grid yielded similar overall flow features and an oscillation frequency near that predicted by the 375 × 161 grid.[11] Density contour plots for both the flux-vector splitting and upwind TVD methods are presented in Figures 6*a* and 6*b*, respectively. The figures represent one point in time and one point in the period of the instability (the two solutions are not at exactly corresponding points within a period) and show that both computational methods predict unsteady behavior. As in the steady computation of Figure 4, the density contours exhibit an outer bow shock followed by an induction zone and an energy-release front. The most obvious difference between the unsteady calculation and the steady one is the pulsing structure of the energy-release front. These pulses are seen in the experimental shadowgraph with the off-axis view in Figure 2*b*.

Figures 7*a* and 7*b* contain shadowgraphs computed from the flux-vector splitting and upwind TVD flowfields, respectively.[16] A comparison of these computed shadowgraphs with the enlargement of Figure 2*a* presented in Figure 8 clearly shows many similarities. Note that the pulses in the energy-release front create the vertical line pattern when the axisymmetric flowfield is projected onto a plane. There is a larger streamwise separation between the vertical lines in the computed shadowgraph compared to the experiment and thus the computation predicts a lower frequency than the experiment. Both numerical methods predict an instability frequency of approximately 530 KHz compared to the measured value of 720 KHz. The primary difference between the flux-vector splitting and upwind TVD solutions is the resolution of the flow structures near the shoulder region of the projectile. The flux-vector splitting smears the features in this region to a larger degree.

Further validation of the computations is provided by comparing the smaller features in the flow. A schematic of the flowfield which labels the different structures is found in Figure 9. A thorough analysis of these structures by McVey and Toong[6] identified the wave extending from the maximum amplitude of each energy-release front pulsation to the bow shock as a contact discontinuity (McVey and Toong refer to it as an entropy wave). Its identity was established by observing that the wave remained at a fixed position on a pulsation as the pulsation was convected downstream. A compression or expansion wave would have moved faster than the local flow with a relative speed which depends on the speed of sound in the mixture. The wave that looks like a reflection of the contact discontinuity off the bow shock does move at a speed greater than the local flow and is identified as a compression wave. The dark-light shadings across the waves further support the asserted identities of the waves. All of these features can be observed in both the experimental and simulated shadowgraphs.

Perhaps the most convincing observation supporting the accuracy of the numerical simulation is the presence of some of the weakest observable flow structures in both the experiment and computation. Although the literature only mentions one contact discontinuity originating from the tip of each pulsation, two contact discontinuities can be observed if the flowfield is examined closely. The additional contact discontinuity is weaker than the first and is at a more shallow angle. Both of these features are observed in the computed shadowgraph as well as in the experimental shadowgraph.

Investigation of other flowfield quantities adds information that cannot be deduced from the shadowgraphs. Pressure contours reveal that each pulse of the energy-release front creates a compression wave which travels both upstream toward the bow shock and downstream toward the projectile body. Figure 10 shows the pressure contours at one point in time. The wave patterns between the bow shock and the projectile appear quite complicated but are simplified by noting that there are primarily two families. One family is made up of compression waves originating directly from the energy-release front and the other family is made up of compression waves from the first family which have reflected off the projectile body.

Instability Mechanism

The phenomenon which causes and sustains the combustion instabilities observed in the ballistic-range has not been directly observed. Therefore, plausible explanations for the unsteadiness have been developed by extrapolating data from outside the nose region (mostly from the shadowgraphs) and by transferring knowledge from other flow situations. It was not until the work of Toong and his associates that plausible detailed mechanisms for the regular[6] and large-disturbance[7] regimes were put forward.

The work of McVey and Toong[6] is discussed further here because it is supported by the present numerical simulations. McVey and Toong used what they called a wave-interaction model to explain the oscillations observed in the regular regime. All of the important processes in this model occur between the energy-release front and the bow shock front in the stagnation region of the nose. As an aid to understanding the model, several of the primary components of the model are isolated and described first.

A major component in the McVey and Toong model is the interaction between the bow shock and a compression wave. Figure 11 depicts a one-dimensional flow at several different times (time proceeds from bottom to top). Initially there is a stationary normal shock and a compression wave downstream of the shock moving toward the shock. At a later time the compression wave overtakes the shock, strengthening it and causing the shock to move forward. The strengthened shock causes a change in the fluid properties behind it. Most important for the instability is a higher fluid temperature. This higher temperature fluid is separated from the fluid which has crossed the shock at the original strength by a contact discontinuity which convects downstream at the fluid velocity. Additionally, a rarefaction wave is created which travels downstream.

Interesting flow features are created when the interaction of Figure 11 is combined with the flow of a combustible mixture. This is the situation presented in Figure 12a. As in Figure 11, there is initially a stationary normal shock wave with a compression moving toward it from the downstream side. Now, there is also burned fluid downstream of the shock at some induction length. As before, the compression wave overtakes the bow shock, strengthening it and creating a contact discontinuity and a rarefaction wave. Because the fluid on the upstream side of the contact discontinuity is hotter it has a shorter induction time and burns more quickly. The result is that for a time there are two regions of burning, one at an induction length corresponding to the conditions behind the original shock strength and one determined by the shorter induction length of the hotter fluid behind the strengthened bow shock (McVey and Toong show that the effect of the contact discontinuity is more important than the effect of the compression wave or rarefaction wave on the burning locations). Figure 12*b* is an x-t diagram corresponding to the interaction in Figure 12*a*. The general features of this diagram are recognizable in the McVey and Toong mechanism presented next.

The McVey and Toong mechanism is schematically depicted in the x-t diagram in Figure 13. The diagram contains the features along the stagnation streamline in time and is explained in the following four steps:

1) A compression wave on the downstream side of the bow shock approaches the bow shock. The compression wave overtakes the bow shock causing the bow shock to move forward, thus creating a reflected rarefaction (which is weak and is ignored in the model) and a contact discontinuity. The gas on the upstream side of the contact discontinuity is hotter than on the downstream side because it has passed through the strengthened bow shock.

2) The rarefaction wave propagating upstream from the energy-release front overtakes the bow shock, weakening it and restoring it to its original strength. The origin of the rarefaction wave is discussed in Step 4.

3) The contact discontinuity created in Step 1 convects downstream. At a point between the bow shock and the energy-release front, a new energy-release front is produced because the hotter gas on the upstream side of the contact discontinuity is ignited more

quickly than the gas on the downstream side of the discontinuity. Because the ignition delay time has an exponential (Arrhenius) dependence on temperature, the change in ignition time is significant even with small temperature changes across the contact discontinuity. The creation of a new zone of combustion, in turn, creates compression waves which propagate both upstream toward the bow shock (this is the wave which overtakes the bow shock in step 1) and downstream toward the projectile. It can be shown that the upstream and downstream compression waves are necessary to match the fluid velocity jumps across the new energy-release front and satisfy conservation of momentum (see Alpert and Toong[7]).

4) The contact discontinuity (with burning on the upstream side) eventually reaches the position of the original energy-release front. This extinguishes the original energy-release front and creates rarefaction waves which propagate in the upstream and downstream direction. The energy-release front then begins to recede toward the location of the original front as colder gas (through a the bow shock of original strength) reaches the front.

McVey and Toong describe how the compression waves and contact discontinuities present in the interaction model can explain the various features observed in experimental shadowgraphs. From Figure 13 it is seen that the period of an oscillation is the time required for the contact discontinuity to travel from the shock to the reaction front and then for an acoustic wave to travel back to the bow shock. If the post-shock conditions are known, an analytical expression for the period of observed experimental oscillations can be found. Given a period of oscillation provided from an experiment, McVey and Toong were able to use the expression to predict the induction time for the gas mixture. Their predicted induction times agreed with previously published data.

Figure 14 contains computed x-t diagrams of density and pressure along the stagnation streamline for the Mach 4.79 case from the computations presented earlier. A comparison of these computed diagrams with the McVey and Toong mechanism in Figure 13 reveal many similarities. The density contours show a changing position of energy-release front in time that is identical to the pattern predicted by the wave interaction model (i.e. note that the jagged edge of the energy-release front appears in both Figures 13 and 14*a*). In the region between the bow shock and the energy-release front, density contours also show that a contact discontinuity is created at the bow shock when a compression wave originating from the energy-release front overtakes it. The hotter gas on the upstream side of the contact discontinuity reduces the ignition delay time and causes a new energy-release front to be created. The new energy-release front is the source of the compression waves traveling in both the upstream and downstream direction. These compression waves are clearly seen in the pressure contours of Figure 14*b*. The identity of the contact discontinuities labeled in Figure 14*a* is verified by their absence in the pressure contours of Figure 14*b* because a contact discontinuity has no pressure jump across it.

A phenomenon seen in the computations which was apparently not anticipated by McVey and Toong is the existence and/or importance of the compression waves reflecting off the projectile nose. Figure 14*b* shows that a compression wave created at the energy-release front travels toward the projectile nose, reflects, and eventually overtakes the bow shock. In this particular calculation, the compression wave reflects off the nose and moves toward the bow shock overtaking it at nearly the same time that the most recently created compression wave arrives at the bow shock. The coordination between the compression wave and the reflected compression wave is not always exact and therefore the two waves sometimes hit the bow shock at slightly different times. This tends to slightly smear or deform some of the structures. The importance of considering the reflection of the compression waves off the projectile has been also been recognized by the recent calculations of Matsuo and Fujiwara.[12]

Figure 15 contains computed x-t diagrams of density and pressure from a case at Mach 5.04. This case is interesting because the interaction of the wave reflected off the projectile is significantly different than is seen in the Mach 4.79 case. As in the Mach 4.79

case, the interactions occuring between the bow shock and energy-release front corresponds to the model proposed by McVey and Toong. The contact discontinuities are clearly defined by the density contours and are absent from the pressure contours. This case differs from the Mach 4.79 case because during the time that a compression wave travels from the energy release front to the projectile body and back, two new compression waves are created (i.e. two periods have passed). The computed frequency is 820 Khz while the measured frequency is 1.04 MHz. A thorough discussion of this case is given in Wilson[11] along with a comparison to an experiment at Mach 4.18 with a much lower oscillation frequency.

Frequency Sensitivity to the Hydrogen-Air Reaction Mechanism

The nearly constant values of the instability frequency predicted by the numerical simulations using different grid sizes (375 × 321, 375 × 161, and 375 × 81) and two different numerical schemes suggests that the underprediction of the frequency in the computations is not caused by numerical error but by the chemical kinetic model. Wilson and MacCormack[8] established that the blunt body exothermic flow fields are quite sensitive to the chain-branching reaction

$$H + O_2 \rightarrow OH + O. \tag{R1}$$

In that work, flowfields were computed with two different rate expressions for this reaction. One was the original expression from the Jachimowski[10] reaction model and the other was from Warnatz[17]. The rate expression recommended by Warnatz was adopted because it gave better agreement with experiment for the steady cases (this is the rate expression that has been used for all cases presented in this paper). To investigate the influence of the chemical kinetic mechanism on the frequency of the oscillations, the Mach 4.79 simulation is repeated using the Jachimowski rate expression for Reaction (R1). This rate expression gives shorter ignition times at high temperatures ($T > 1400K$) than the rate constant recommended by Warnatz. This change should lead to an increase in the oscillation frequency because the induction zone is smaller and therefore the travel time between the energy-release front and the bow shock is reduced. Consistent with this expectation, the computed frequency of the oscillations increased from approximately 530 KHz to 820 KHz. Since the experimentally determined frequency is 720 KHz, it is concluded that the uncertainties in the rate constants for the reaction mechanism could explain the differences between the experiments and the computations. The sensitivity of the oscillation frequency to the chemical reactions make the simulations a useful validation tool for kinetic models. The unsteady cases appear to provide a better measure of a kinetic model than the steady cases because with the available data the oscillation frequency can be determined with greater precision than the positions of the bow shock and energy-release front.

As a final note, it is mentioned that the arrival of new compression waves and reflected pressure waves at the bow shock sometimes differ significantly (this occurred in the Mach 4.79 case with the Jachimowski rate expression[11]). The separate interactions with the bow shock by each wave lead to separate contact discontinuities and cause the x-t diagrams to appear less organized. It seems, however, that even with these waves out of phase, an overall periodic nature can exist because the reflected waves have a secondary effect. Further investigations are required to assess the precise contribution to the combustion instability by the compression waves reflected off the projectile nose. It is possible that the reflected waves are more important to the instabilities seen in the large-disturbance regime investigated by Alpert and Toong[8] than they are to the regular regime cases considered here.

Conclusion

The successful simulations of both steady and unsteady exothermic ballistic-range experiments have added to the understanding of high speed flows with combustion and have led to improvements in the numerical techniques for these types of flows. Namely, proper grid resolution is a primary challenge of simulations with combustion phenomena and these grid requirements are reduced significantly by the use of the logarithmic transformation of the species conservation equations. The simulations have also provided information about combustion instabilities which may, in turn, help interpret unstable combustion phenomena in other settings. The accuracy of the simulations is supported by grid refinement studies and the use of two different numerical methods, a flux vector splitting scheme and an upwind TVD scheme. Further validation is provided by comparison to past analytical and numerical predictions of the instabilities. Finally, the simulations have reaffirmed the value of ballistic-range experiments as a source of data for high speed flows with combustion and have demonstrated their usefulness for validating numerical methods and chemical kinetic mechanisms. It was shown that differences in the experimental and computed instability frequencies are probably due to uncertainties in the chemical reaction rates and therefore the experiments provide a means of validating proposed chemical kinetic models.

Acknowledgements

We are most grateful to Dr. H.F. Lehr of ISL for providing original photographs of his ballistic-range experiments and to Leslie A. Yates for computing shadowgraph images from our flowfield solutions. We also acknowledge the support and encouragement of our advisor at Stanford University, Professor Robert W. MacCormack. Funds for the support of this study have been allocated by the NASA Langley Research Center and by the NASA Ames Research Center under the joint research interchange number NCA2-455 and is greatly appreciated. This material is also based upon work supported by a National Science Foundation Graduate Fellowship and by NASA under Hypersonic Training and Research Grant No. NAGW 965. The authors would also like to acknowledge the computer resources provided by Steve Deiwert, Chief of the Aerothermodynamics branch of NASA Ames and Ajay Kumar, Chief of the Theoretical Flow Physics Branch at NASA Langley. Additional computer resources were provided by the National Aerodynamic Simulator Facility (NAS).

References

1) Ruegg, F. W., and Dorsey, W. W., "A Missile Technique for the Study of Detonation Waves," *Journal of Research of the National Bureau of Standards*, Vol. 66C,1962, pp. 51-58.

2) Behrens, H., Struth, W., and Wecken, F., "Studies of Hypervelocity Firings into mixtures of Hydrogen With Air or With Oxygen," *Tenth Symposium (International) on Combustion*, 1965, pp. 245-252.

3) Chernyi, G. G., "Onset of Oscillation in the Presence of Detonation Wave Weakening," *PMM*, Vol. 33, 1969, pp. 465-475.

4) Lehr, H. F., Institute Saint Louis (ISL) Final Report 20/71, 1971.

5) Lehr, H. F.,"Experiments on Shock-Induced Combustion," *Astronautica Acta*, Vol. 17, 1972, pp. 589-596.

6) McVey, B.J., and Toong, T.Y., "Mechanism of Instabilities of Exothermic Hypersonic Blunt-Body Flows," *Combustion Science and Technology*, Vol. 3, 1971, pp. 63-76.

7) Alpert, R. L., and Toong, T. Y., "Periodicity in Exothermic Hypersonic Flows about Blunt Projectiles," *Astronautica Acta.*, Vol. 17, 1972, pp. 539-560.

8) Wilson,G. J. and MacCormack, R. W., "Modeling Supersonic Combustion using a Fully-Implicit Numerical Method," AIAA paper 90-2307, July 1990.

9) Sussman, M. A., and Wilson, G. J., "Computation of Chemically Reacting Flow Using A Logarithmic Form of the Species Conservation Equations," *Proceedings of the 4th International Symposium on CFD*, Davis, CA, Vol. 2, Sept. 1991, pp. 1113-1118.

10) Jachimowski, C. J., "An Analytical Study of the Hydrogen-Air Reaction Mechanism With Application to Scramjet Combustion," NASA TP-2791, February 1988.

11) Wilson, G. J., "Computation of Steady and Unsteady Shock-Induced Combustion Over Hypervelocity Blunt Bodies," *Ph.D Thesis*, Stanford University, December, 1991.

12) Matsuo, A., and Fujiwara, T., "Numerical Simulation of Shock-Induced Combustion Around an Axisymmetric Blunt Body," AIAA Paper 91-1414, June 1991.

13) MacCormack, R. W., "Current Status of Numerical Solutions of the Navier-Stokes Equations," AIAA paper 85-0032, Jan. 1985.

14) Candler, G. V., "The Computation of Weakly Ionized Hypersonic Flows in Thermo-Chemical Nonequilibrium," *Ph.D Thesis*, Stanford University, June 1988.

15) Yee, H. C., "A Class of High-Resolution Explicit and Implicit Shock-Capturing Methods," NASA TM 101088, February, 1989.

16) Yates, L. A., "Interferograms, Schlieren, and Shadowgraphs Constructed from Real- and Ideal-Gas, Two- and Three-Dimensional Computed Flow Fields and Comparisons to Experiment," to be published at the 17th AIAA Ground Testing Conference, Nashville, TN, September, 1992.

17) Warnatz, J., "Rate Coefficients in the C/H/O System," *Combustion Chemistry*, Chapter 5, Gardiner, Jr., W. C. (Ed.), Springer-Verlag, New York, 1984.

Captions

Figure 1: Shadowgraph of a Spherical Nose Projectile Moving at Mach 6.46 in a Stoichiometric Hydrogen-Air Mixture (Courtesy of H.F. Lehr).

Figure 2: Shadowgraph of a Spherical Nose Projectile Moving at Mach 4.79 in a Stoichiometric Hydrogen-Air Mixture: a) side view b) off-axis view (Courtesy of H.F. Lehr).

Figure 3: Variation of the mass fraction of the hydroxyl (OH) radical in the induction zone for a quasi-one-dimensional calculation of shock-induced combustion.

Figure 4: Density contours from a numerical simulation of the Mach 6.46 experiment in Figure 1: a) flux-vector splitting b) upwind TVD.

Figure 5: 52 × 52 grid used for the calculations presented in Figure 4.

Figure 6: Density contours from a numerical simulation of the Mach 4.79 experiment in Figure 2: a) flux-vector splitting b) upwind TVD.

Figure 7: Computed shadowgraphs from a numerical simulation of the Mach 4.79 experiment in Figure 2: a) flux-vector splitting b) upwind TVD (shadowgraphs computed by L.A. Yates[16]).

Figure 8: Enlargement of the Mach 4.79 ballistic-range shadowgraph in Figure 2*a* (courtesy of H.F. Lehr).

Figure 9: Schematic of the periodic flowfield structures seen in shadowgraphs of ballistic-range experiments.

Figure 10: Pressure contours for the Mach 4.79 case at one point in an oscillation period.

Figure 11: Schematic of a one-dimensional bow shock – compression wave interation.

Figure 12: Schematic of a bow shock – compression wave interaction with shock-induced combustion: a) series of one-dimensional diagrams b) x-t diagram.

Figure 13: McVey and Toong[6] wave interaction model.

Figure 14: Computed x-t diagrams of density and pressure along the stagnation streamline for the Mach 4.79 case using flux-vector splitting: a) density contours b) pressure contours.

Figure 15: Computed x-t diagrams of density and pressure along the stagnation streamline for the Mach 5.04 case using flux-vector splitting: a) density contours b) pressure contours.

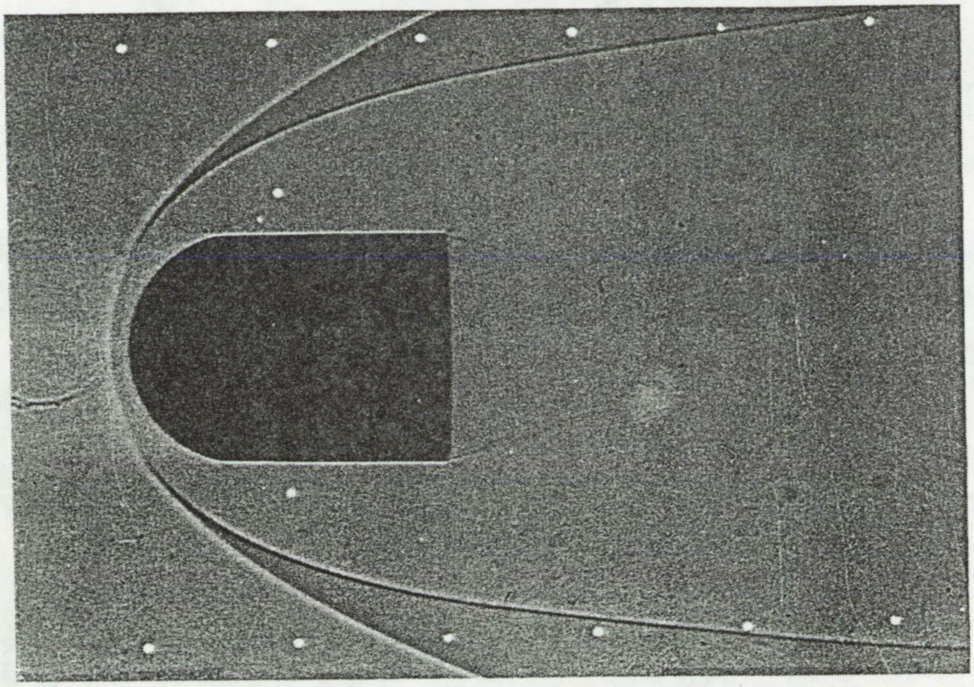

Figure 1

Wilson & Sussman

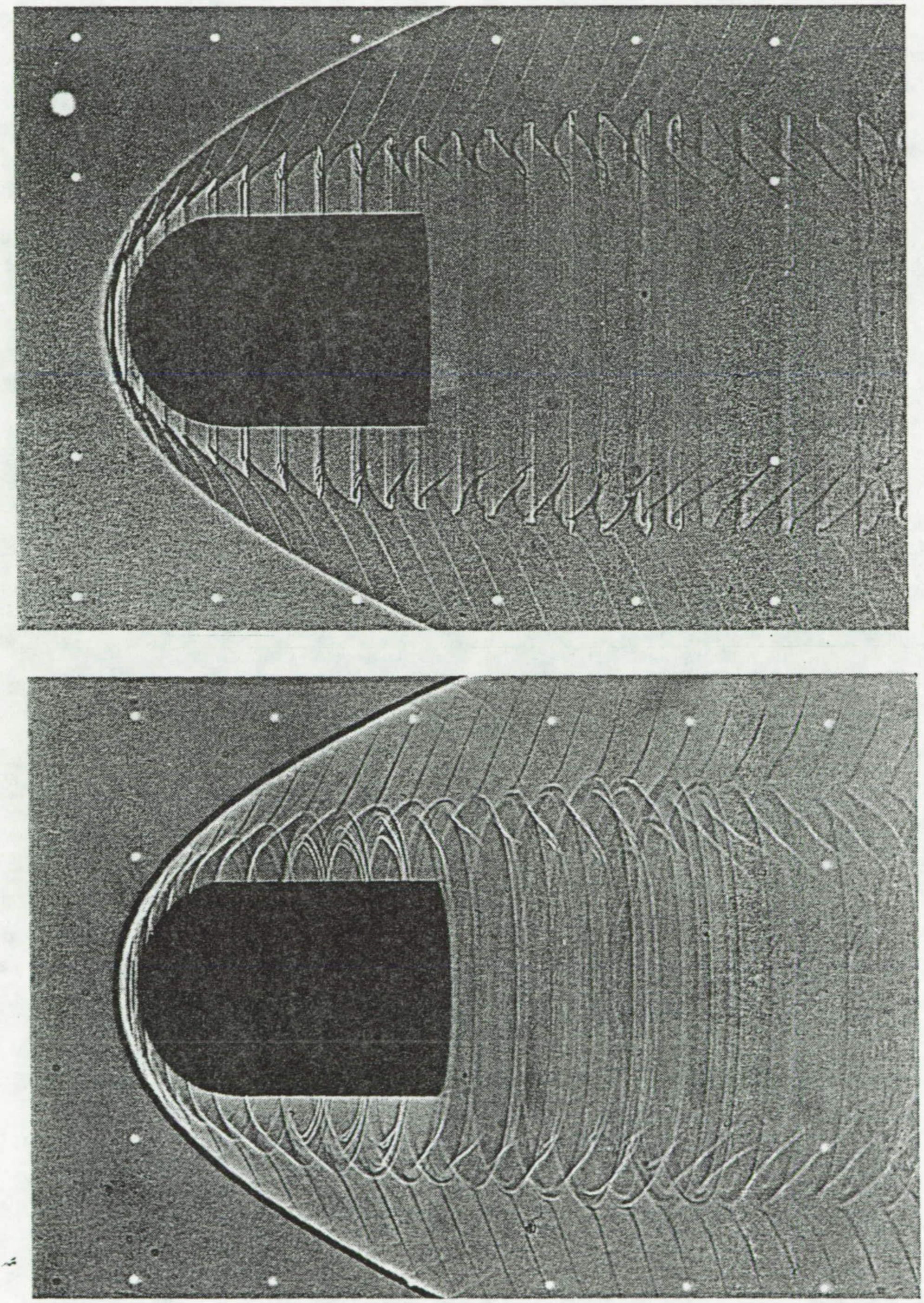

Figure 2a,b

Wilson & Sussman

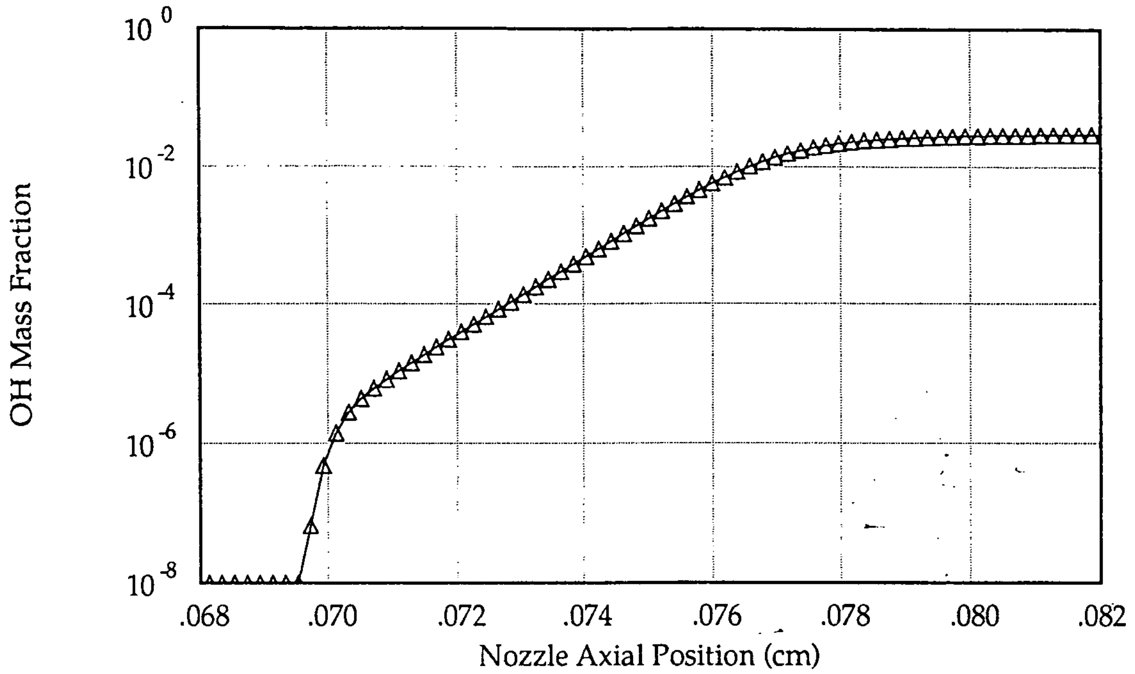

Figure 3

Wilson & Sussman

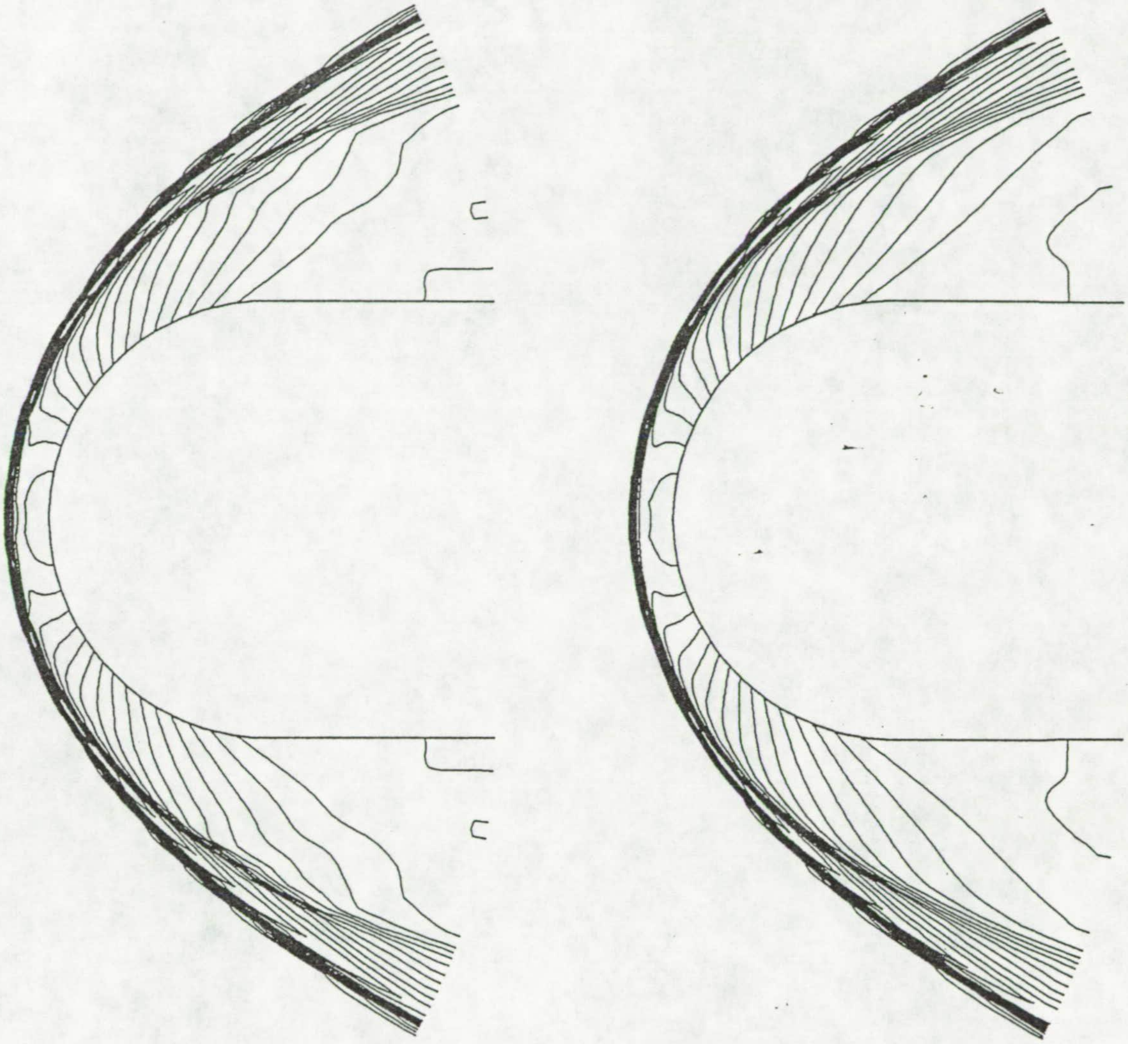

Figure 4 a,b

Wilson & Sussman

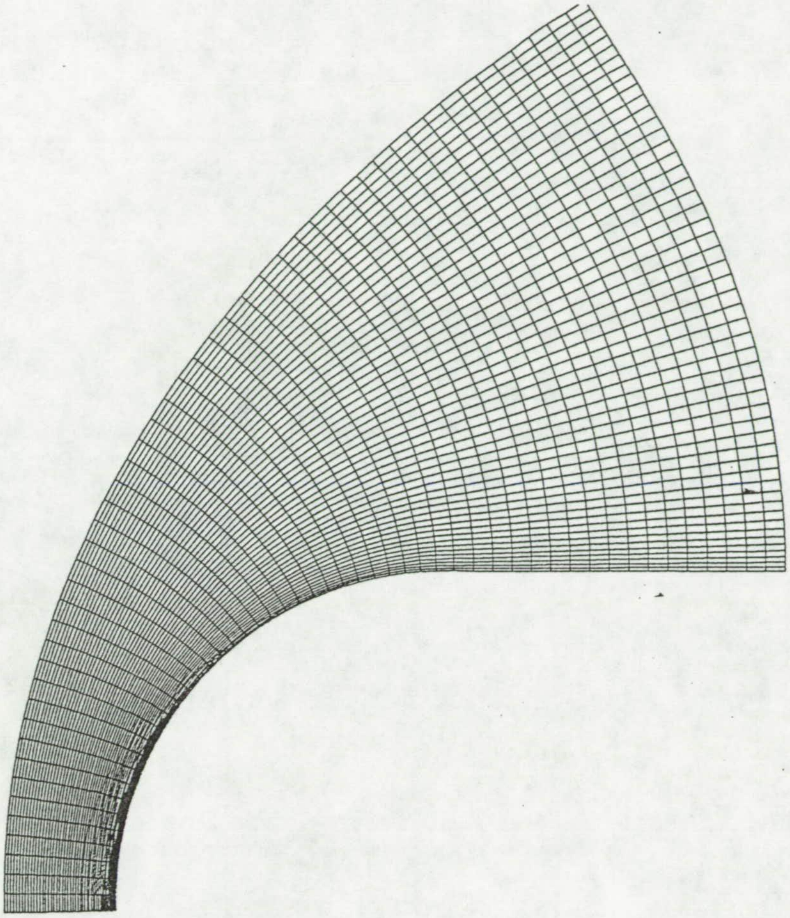

Figure 5

Wilson & Sussman

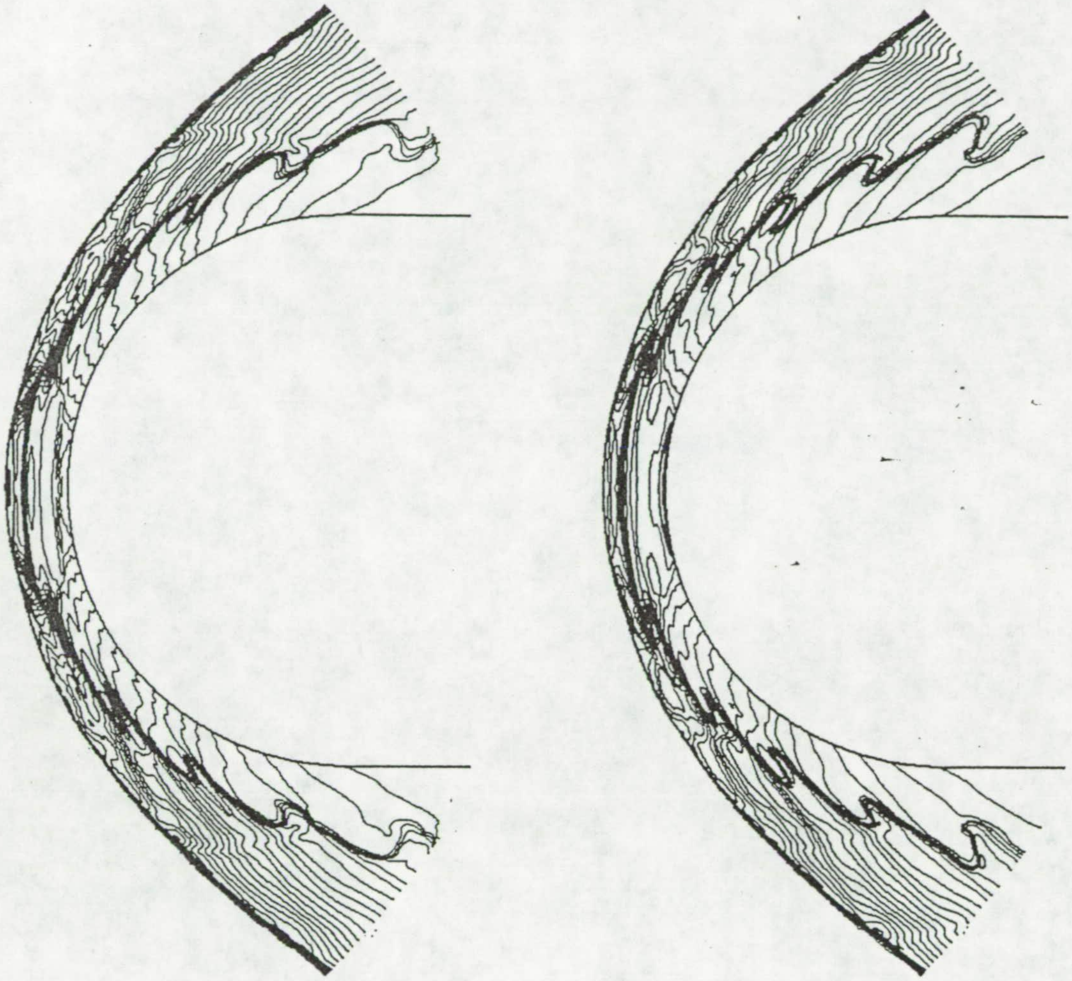

Figure 6 a, b

Wilson & Sussman

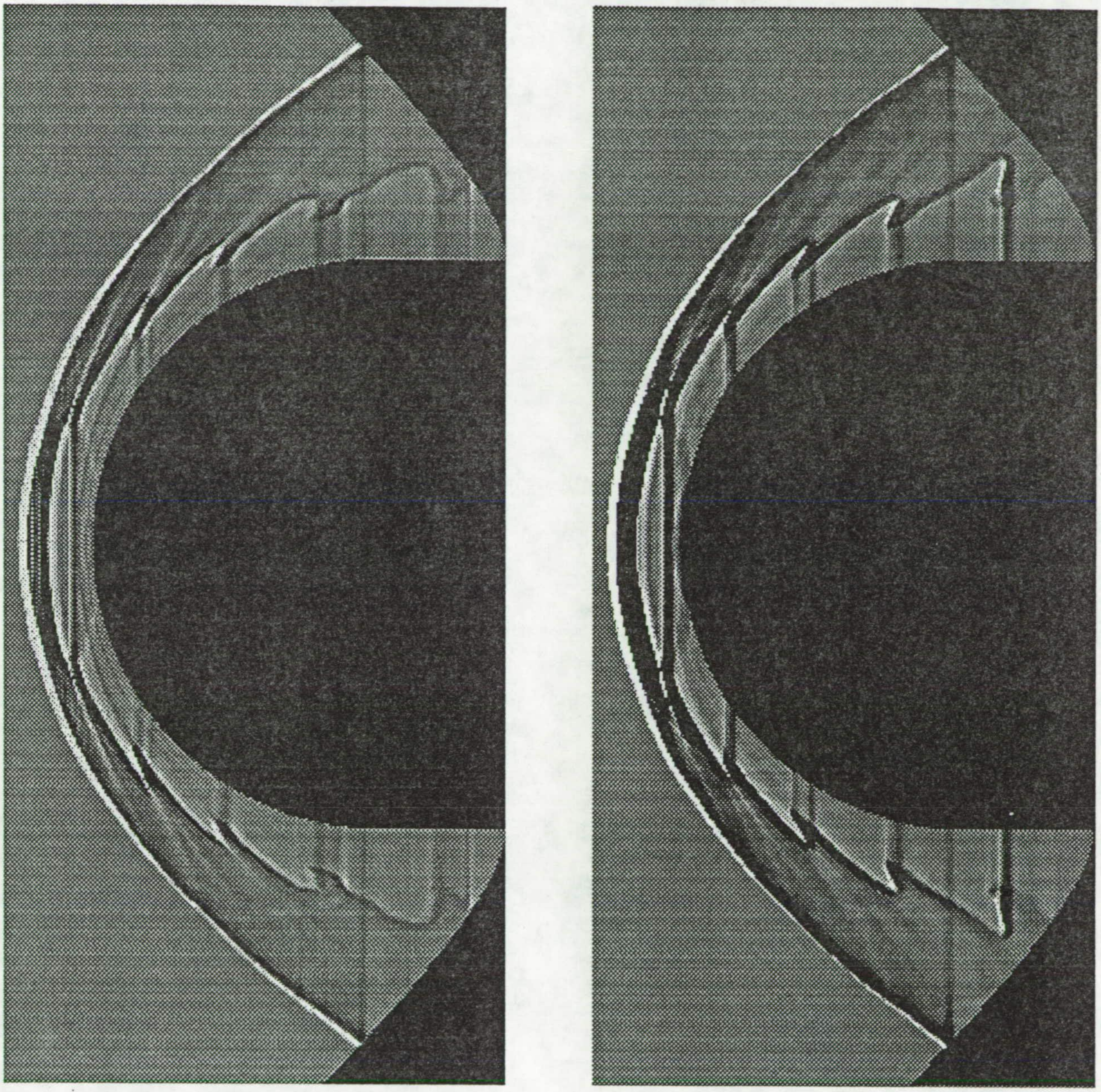

Figure 7a,b

Wilson & Sussman

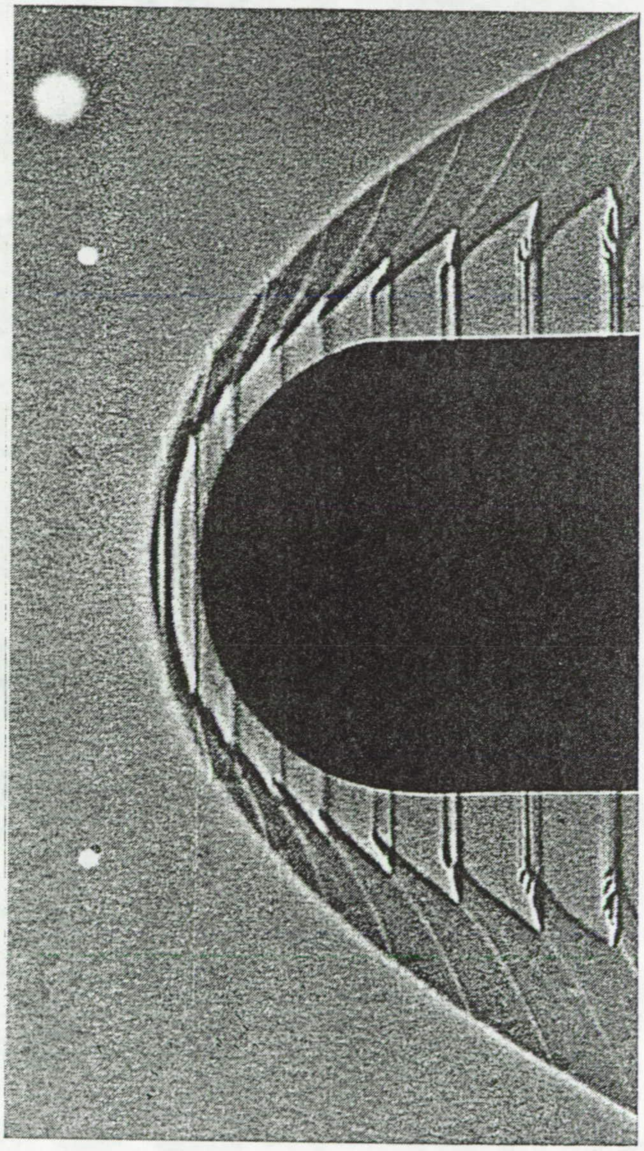

Figure 8

Wilson & Sussman

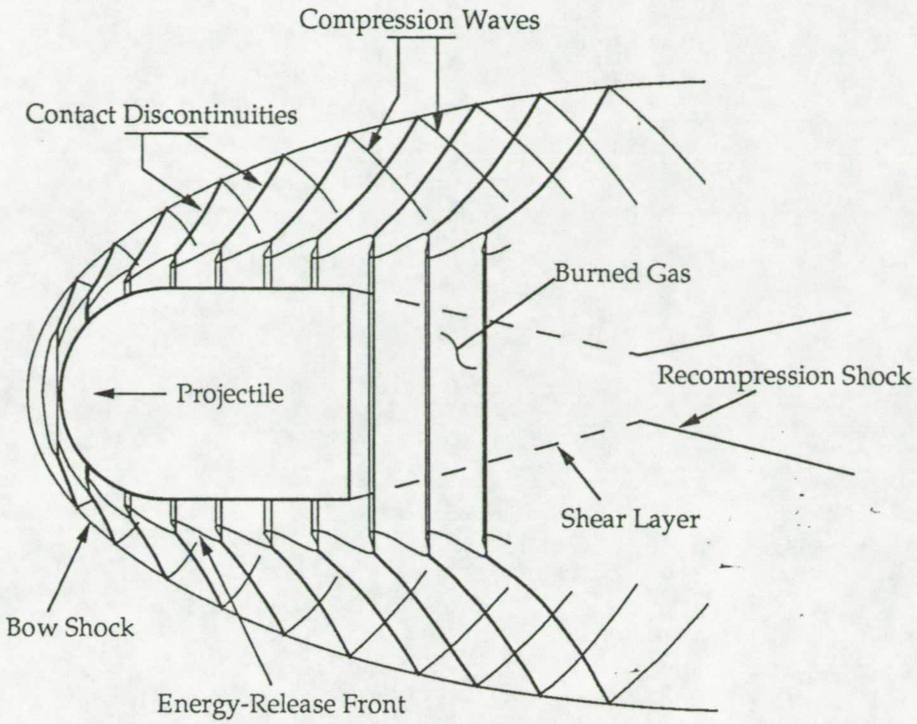

Figure 9

Wilson & Sussman

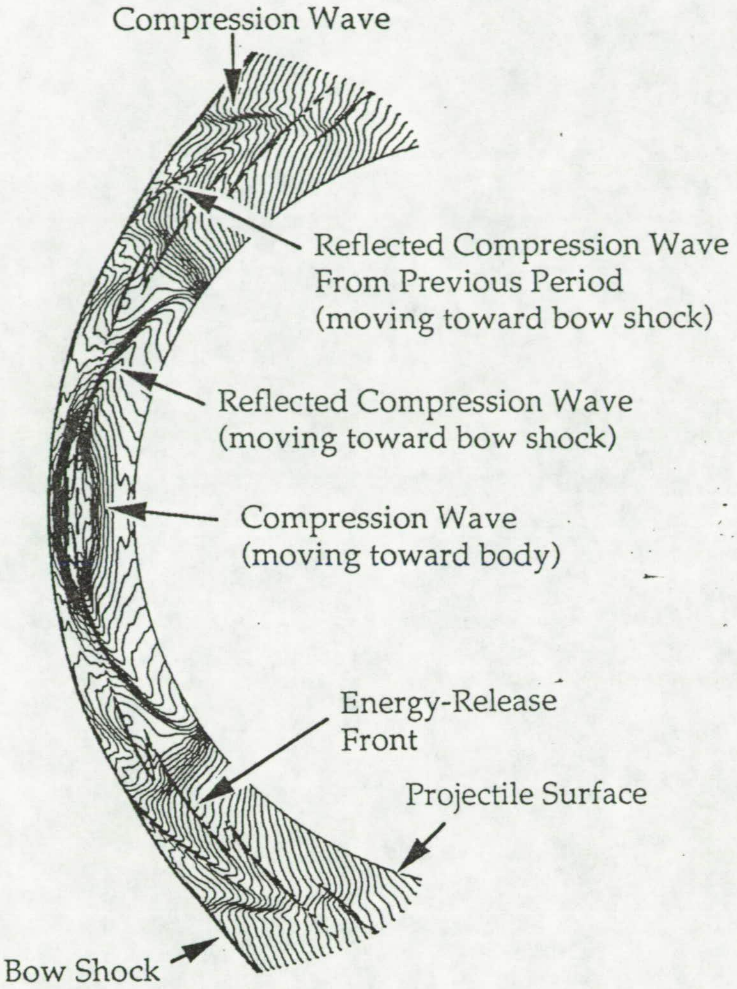

Figure 10

Wilson & Sussman

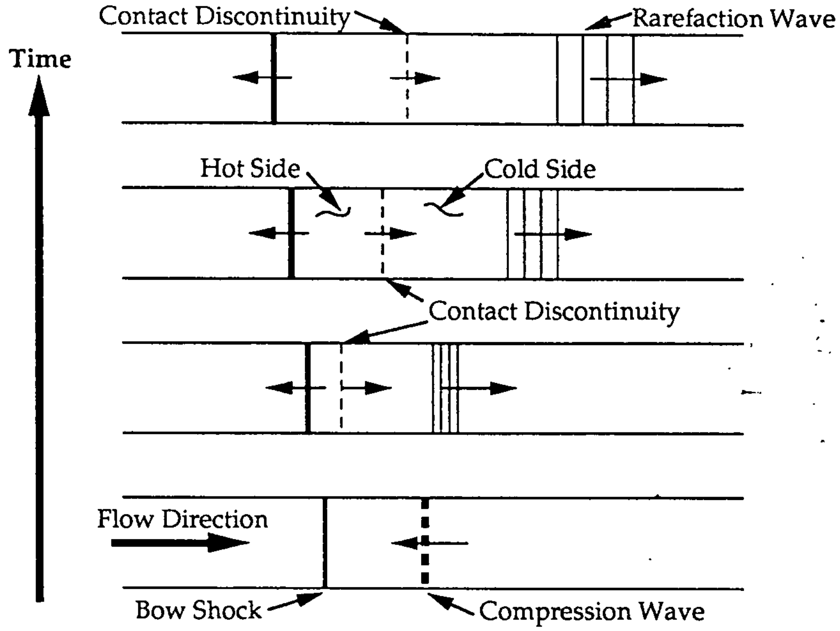

Figure 11

Wilson & Sussman

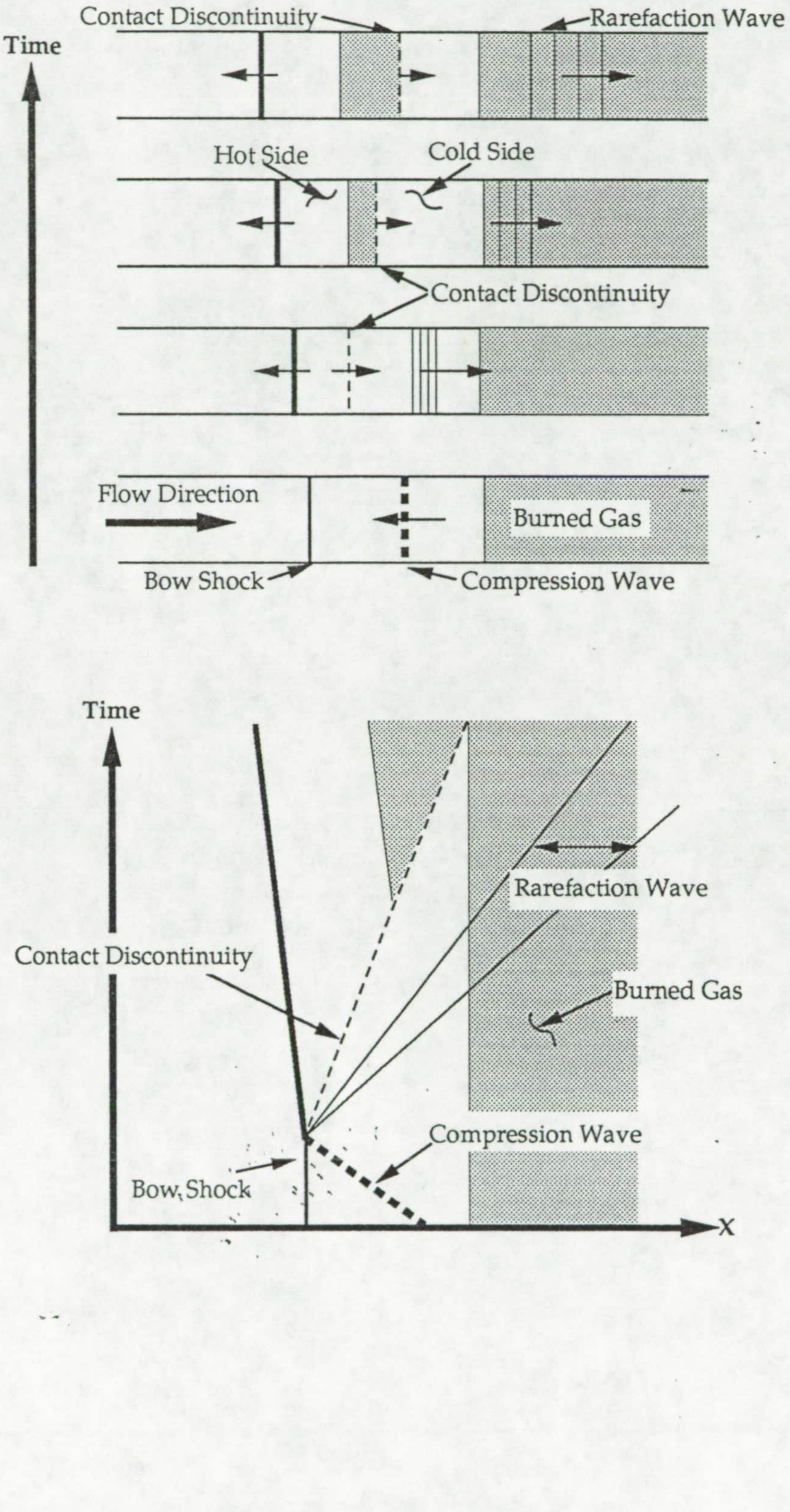

Figure 12 a,b

Wilson & Sussman

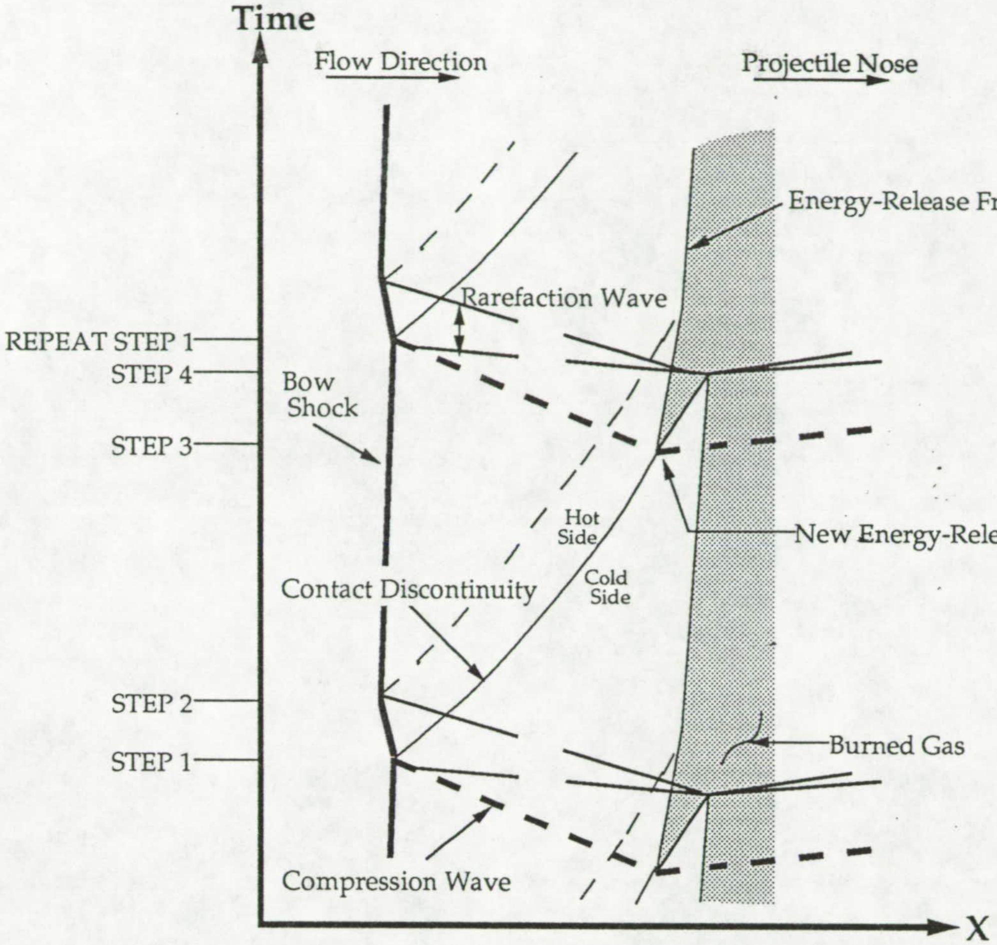

Figure 13

Wilson & Sussman

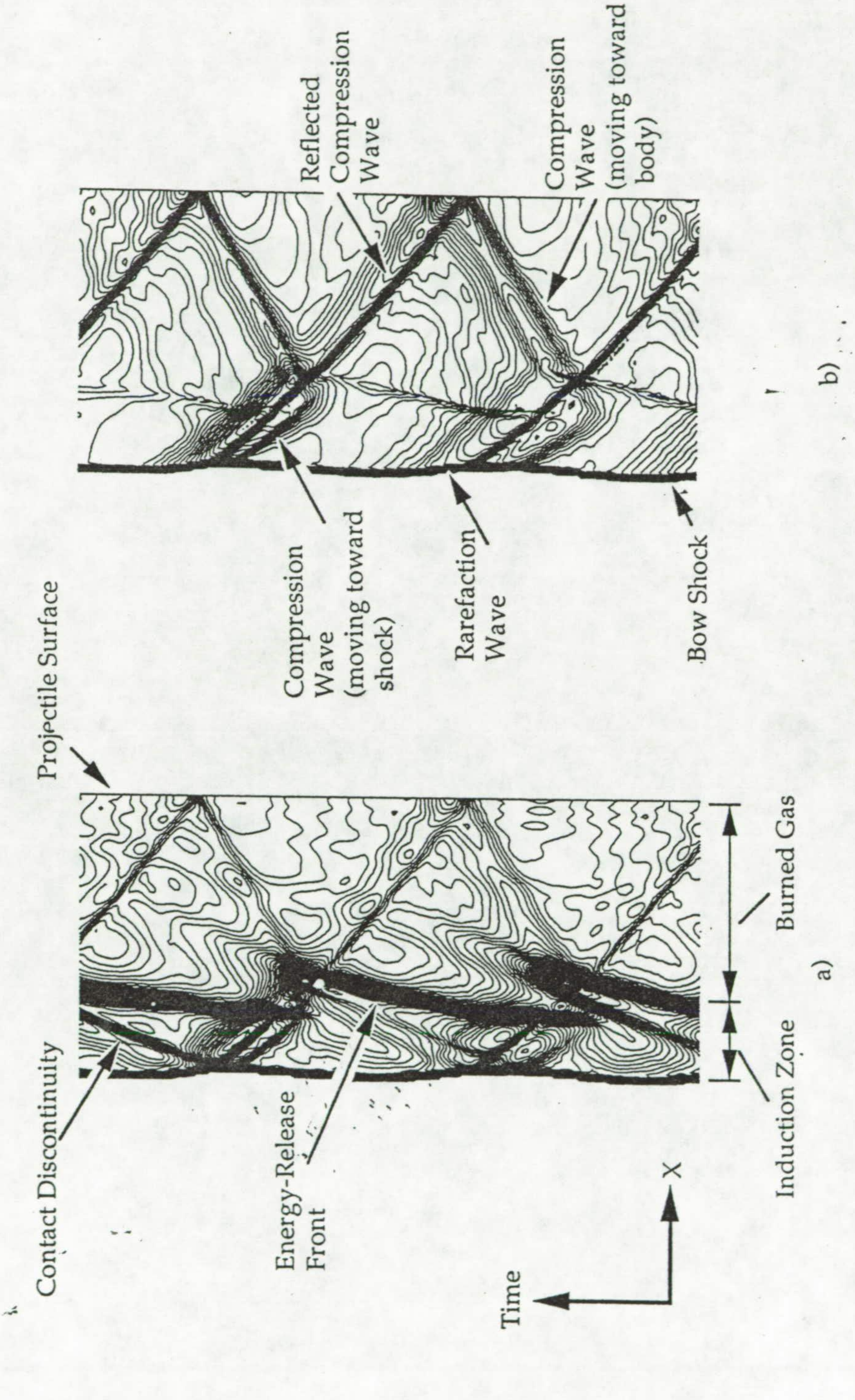

Figure 14 a,b

Wilson & Sussman

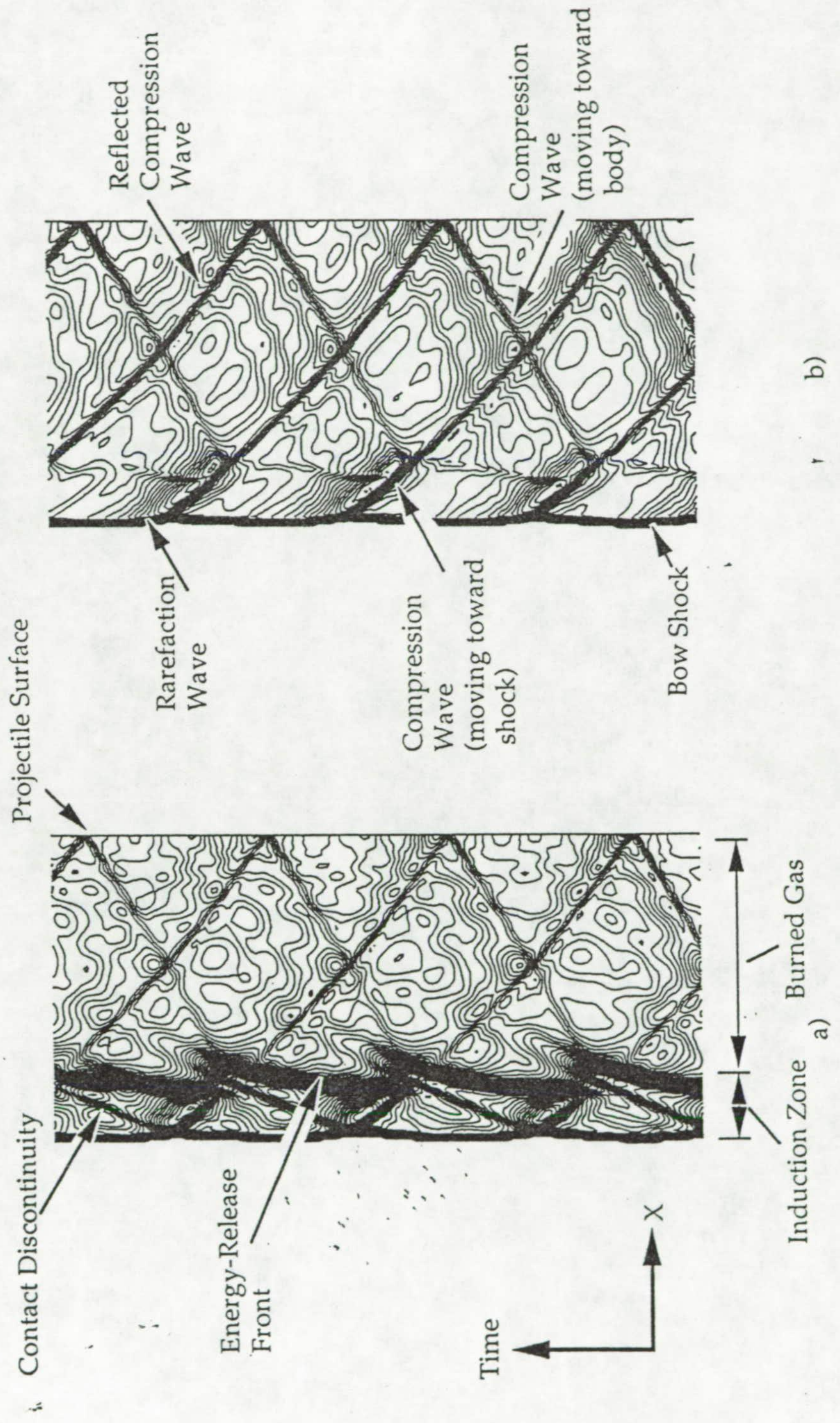

Figure 15 a,b

Wilson & Sussman